

Advanced Nanomaterials and Nanostructures for Tribological Applications

Guest Editors: Yongsheng Zhang, Tianchang Hu, Xianjin Ning,
and Qi Ding





Advanced Nanomaterials and Nanostructures for Tribological Applications

Journal of Nanomaterials

Advanced Nanomaterials and Nanostructures for Tribological Applications

Guest Editors: Yongsheng Zhang, Tianchang Hu, Xianjin Ning,
and Qi Ding



Copyright © 2014 Hindawi Publishing Corporation. All rights reserved.

This is a special issue published in "Journal of Nanomaterials." All articles are open access articles distributed under the Creative Commons Attribution License, which permits unrestricted use, distribution, and reproduction in any medium, provided the original work is properly cited.

Editorial Board

Katerina E. Aifantis, USA
Nageh K. Allam, USA
Margarida Amaral, Portugal
Xuedong Bai, China
Lavinia Balan, France
Enrico Bergamaschi, Italy
Theodorian Borca-Tasciuc, USA
C. Jeffrey Brinker, USA
Christian Brosseau, France
Xuebo Cao, China
Shafiq Chowdhury, USA
Kwang-Leong Choy, UK
Cui ChunXiang, China
Miguel A. Correa-Duarte, Spain
Shadi A. Dayeh, USA
Ali Eftekhari, USA
Claude Estournés, France
Alan Fuchs, USA
Lian Gao, China
Russell E. Gorga, USA
Hongchen Chen Gu, China
Mustafa O. Guler, Turkey
John Z. Guo, USA
Smrati Gupta, Germany
Michael Harris, USA
Zhongkui Hong, China
Michael Z. Hu, USA
David Hui, USA
Y.-K. Jeong, Republic of Korea
Sheng-Rui Jian, Taiwan
Wanqin Jin, China
Rakesh K. Joshi, UK
Zhenhui Kang, China
Fathallah Karimzadeh, Iran
Alireza Khataee, Iran

Do K. Kim, Korea
Alan K. T. Lau, Hong Kong
Burtrand Lee, USA
Jun Li, Singapore
Benxia Li, China
Xing-Jie Liang, China
Shijun Liao, China
Gong-Ru Lin, Taiwan
Tianxi Liu, China
Jun Liu, USA
Songwei Lu, USA
Daniel Lu, China
Jue Lu, USA
Ed Ma, USA
Gaurav Mago, USA
Santanu K. Maiti, India
Sanjay R. Mathur, Germany
Vikas Mittal, UAE
Weihai Ni, Germany
Sherine Obare, USA
Atsuto Okamoto, Japan
Abdelwahab Omri, Canada
Edward A. Payzant, USA
Kui-Qing Peng, China
Anukorn Phuruangrat, Thailand
Mahendra Rai, India
Suprakas Sinha Ray, South Africa
Ugur Serincan, Turkey
Huaiyu Shao, Japan
Donglu Shi, USA
Vladimir Sivakov, Germany
Marinella Striccoli, Italy
Bohua Sun, South Africa
Saikat Talapatra, USA
Nairong Tao, China

Titipun Thongtem, Thailand
Somchai Thongtem, Thailand
Alexander Tolmachev, Ukraine
Valeri P. Tolstoy, Russia
Tsung-Yen Tsai, Taiwan
Takuya Tsuzuki, Australia
Raquel Verdejo, Spain
Mat U. Wahit, Malaysia
Zhenbo Wang, China
Ruiping Wang, Canada
Shiren Wang, USA
Cheng Wang, China
Yong Wang, USA
Jinquan Wei, China
Ching-Ping Wong, Hong Kong
Xingcai Wu, China
Guodong Xia, Hong Kong
Ping Xiao, UK
Zhi Li Xiao, USA
Yangchuan Xing, USA
Shuangxi Xing, China
Nanping Xu, China
Doron Yadlovker, Israel
Yingkui Yang, China
Khaled Youssef, USA
Kui Yu, Canada
William W. Yu, USA
Haibo Zeng, China
Tianyou Zhai, China
Renyun Zhang, Sweden
Bin Zhang, China
Yanbao Zhao, China
Lianxi Zheng, Singapore
Chunyi Zhi, Hong Kong

Contents

Advanced Nanomaterials and Nanostructures for Tribological Applications, Yongsheng Zhang, Tianchang Hu, Xianjin Ning, and Qi Ding
Volume 2014, Article ID 402198, 2 pages

Elastic Properties of the Fabric Liner and Their Influence on the Wear Depth of the Spherical Plain Bearing, Xuejin Shen, Pandong Gao, Zhaolei Liu, and Xiaoyang Chen
Volume 2014, Article ID 836386, 7 pages

Regression Analysis of the Effect of Bias Voltage on Nano- and Macrotribological Properties of Diamond-Like Carbon Films Deposited by a Filtered Cathodic Vacuum Arc Ion-Plating Method, Shojiro Miyake, Takanori Shindo, and Masatoshi Miyake
Volume 2014, Article ID 657619, 13 pages

Preparation and Tribological Properties of Dual-Coated TiO₂ Nanoparticles as Water-Based Lubricant Additives, Yue Gu, Xiuchen Zhao, Ying Liu, and Yunxia Lv
Volume 2014, Article ID 785680, 8 pages

Hard and Soft Multilayered SiCN Nanocoatings with High Hardness and Toughness, S. K. Mishra, Devraj Verma, S. Bysakh, and L. C. Pathak
Volume 2013, Article ID 949416, 8 pages

The Effect of Nitrogen Ion Implantation on the Surface Properties of Ti6Al4V Alloy Coated by a Carbon Nanolayer, Petr Vlcek, Frantisek Cerny, Zdenek Weiss, Stanislav Danis, Josef Sepitka, Zdenek Tolde, and Vladimir Jech
Volume 2013, Article ID 475758, 8 pages

Editorial

Advanced Nanomaterials and Nanostructures for Tribological Applications

Yongsheng Zhang,¹ Tianchang Hu,¹ Xianjin Ning,² and Qi Ding¹

¹ State Key Laboratory of Solid Lubrication, Lanzhou Institute of Chemical Physics, Chinese Academy of Sciences, Lanzhou 730000, China

² School of Materials Science & Engineering, Beijing Institute of Technology, Beijing 100081, China

Correspondence should be addressed to Yongsheng Zhang; zhys@licp.cas.cn

Received 25 March 2014; Accepted 25 March 2014; Published 9 April 2014

Copyright © 2014 Yongsheng Zhang et al. This is an open access article distributed under the Creative Commons Attribution License, which permits unrestricted use, distribution, and reproduction in any medium, provided the original work is properly cited.

Lubricating problems are common in many engineering applications, such as aerospace, ground mechanical equipment, and large aircraft carriers. Moreover, the high-performance lubricating materials are the key to ensure high running precision and stability for mechanical systems. With the rapid development of modern technology, various lubricating materials have been developed for different machineries. These developments are geared toward improving the property of materials and allowing them to surmount severe challenges under extreme conditions (e.g., high/low temperature, special media, and unfavorable atmosphere) in the fields of aviation, space, nuclear energy, and microelectronics. The lubricating materials corresponding to the required conditions in these fields must be capable of working in corrosive environments and high/low temperatures for a long time. However, because the conventional lubricating materials cannot satisfy these application requirements, lubricating materials are currently facing a series of challenges [1, 2].

In recent years, much effort has been directed toward preparing high-performance materials and coatings for tribological applications, such as laminated-graded self-lubricating composites [3, 4], composite-lubricating coatings [5], and DLC films with surface texturing [6]. In addition, nanomaterials and nanostructures, because of their special dimensional effects, reveal totally different tribological and mechanical properties compared with traditional materials

[7, 8]. The combination of nanomaterials and lubricating composites is a promising way to achieve the optimization of lubricating materials [9]. Meanwhile, the emergences of new preparation technologies [10] and theoretical approaches [11] have hastened the development of an increasingly large number of new lubricating materials and thus speeded up the industrialization process of these materials.

In this special issue, five papers are devoted to the mechanical and tribological performances of nanomaterials and films. The carbon nanolayer, remained on the surface of Ti6Al4V alloy after ion implantation, was proved to have an influence on friction reduction due to the self-lubrication property of the carbon nanolayer. Dual-coated TiO₂ nanoparticles as water based lubricant additive and cutting fluids additive provided excellent tribological properties, which might be ascribed to the forming of a dynamic deposition film during rubbing process according to surface analysis. For DLC films, nanotribological properties such as H (Nanoindentation hardness) and nanowear resistance were highly correlated with I_D/I_G ratio and highly dependent on the films' nanostructures. Hard and soft multilayered SiCN nanocoatings with high hardness and toughness were prepared by magnetron sputtering. Increased deformation accommodation was achieved for such alternate hard and soft layers as the thin hard layers slide relative to each other due to shear deformation of low modulus layers. This special issue also contains a very interesting hypothesis about

developing an elastic property analysis model suitable for three commonly used fabric liners through a theoretical analysis of the elastic properties.

We hope that readers will find in this special issue not only accurate data and updated reviews on the tribological behavior of advanced materials, but also important guidance for the optimization of the advanced lubricating materials.

Yongsheng Zhang
Tianchang Hu
Xianjin Ning
Qi Ding

References

- [1] Y. S. Zhang, Y. Fang, H. Z. Fan, J. J. Song, T. C. Hu, and L. T. Hu, *High-Performance Ceramic Lubricating Materials*, vol. 17 of *Advances in Materials Science Research*, Nova Science, New York, NY, USA, 2014.
- [2] Y. E. Qi, Y. S. Zhang, and L. T. Hu, "High-temperature self-lubricated properties of $\text{Al}_2\text{O}_3/\text{Mo}$ laminated composites," *Wear*, vol. 280-281, pp. 1-4, 2012.
- [3] Y. Fang, Y. S. Zhang, J. J. Song, H. Z. Fan, and L. T. Hu, "Design and fabrication of laminated-graded zirconia self-lubricating composites," *Materials & Design*, vol. 49, pp. 421-425, 2013.
- [4] Y. E. Qi, Y. S. Zhang, Y. Fang, and L. T. Hu, "Design and preparation of high-performance alumina functional graded self-lubricated ceramic composites," *Composites Part B: Engineering*, vol. 47, pp. 145-149, 2013.
- [5] T. C. Hu, Y. S. Zhang, and L. T. Hu, "Tribological investigation of MoS_2 coatings deposited on the laser textured surface," *Wear*, vol. 278-279, pp. 77-82, 2012.
- [6] Q. Ding, L. P. Wang, Y. F. Wang, S. C. Wang, L. T. Hu, and Q. J. Xue, "Improved tribological behavior of DLC films under water lubrication by surface texturing," *Tribology Letters*, vol. 41, pp. 439-449, 2011.
- [7] Y. S. Zhang, J. M. Chen, and L. T. Hu, "Progress on tribological investigation of ceramic-based nanocomposites," *Tribology*, vol. 26, pp. 284-288, 2006.
- [8] T. C. Hu, Y. S. Zhang, and L. T. Hu, "Mechanical and wear characteristic of Y-TZP/ Al_2O_3 nanocomposites," *Industrial Lubrication and Tribology*, vol. 66, pp. 209-214, 2014.
- [9] Y. S. Zhang, L. T. Hu, J. M. Chen, and W. M. Liu, "Lubrication behavior of Y-TZP/ $\text{Al}_2\text{O}_3/\text{Mo}$ nanocomposites at high temperature," *Wear*, vol. 268, pp. 1091-1094, 2010.
- [10] X. J. Ning, J. H. Kim, H. J. Kim, and C. Lee, "Characteristics and heat treatment of cold-sprayed Al-Sn binary alloy coatings," *Applied Surface Science*, vol. 255, pp. 3933-3939, 2009.
- [11] Q. Wang and Y. W. Chung, *Encyclopedia of Tribology*, Springer, New York, NY, USA, 2013.

Research Article

Elastic Properties of the Fabric Liner and Their Influence on the Wear Depth of the Spherical Plain Bearing

Xuejin Shen, Pandong Gao, Zhaolei Liu, and Xiaoyang Chen

Department of Mechanical Automation Engineering, Shanghai University, Shanghai 200072, China

Correspondence should be addressed to Xuejin Shen; shenxuejin@gmail.com

Received 20 December 2013; Accepted 3 February 2014; Published 17 March 2014

Academic Editor: Yongsheng Zhang

Copyright © 2014 Xuejin Shen et al. This is an open access article distributed under the Creative Commons Attribution License, which permits unrestricted use, distribution, and reproduction in any medium, provided the original work is properly cited.

The major failure mechanism of typical spherical plain bearings with self-lubrication is the wear of the woven fabric liner, which is an orthotropic composite of different elastic properties in different directions. The elastic properties of the liner are required for studying the tribological properties of the spherical plain bearings. This paper aims to develop an elastic property analysis model suitable for three commonly used fabric liners through a theoretical analysis of the elastic properties in order to obtain the parameter expression of the compliance matrix. The influence of the elastic properties on the wear depth of the spherical plain bearings is further investigated. Suggestions are made for the optimal design of the spherical plain bearings based on wear reduction.

1. Introduction

Spherical plain bearing with self-lubricating is a kind of sliding bearings with low-speed multiaxial rotary oscillating motion pattern. Widely used in mining and metallurgy, aerospace, tank cannon gun system, and so forth [1, 2], the typical spherical plain bearing with self-lubricating consists of an inner ring with an outside spherical surface and an outer ring which has an inner sphere surface with a woven fabric liner bonded to it, and its main failure form is the wear of the woven fabric liner. The current studies on woven fabric liner of spherical plain bearing with self-lubricating largely concern the aspect of friction and wear experiments [3, 4], while the elastic properties are obtained mainly by tensile test experiments [5, 6] or numerical experiments [7–9]. Most of the experiments focus on the particular structure of the woven fabric liners [10–14]. Obtaining the elastic properties of the liner is essential in studying the mechanical properties of spherical plain bearings. The study on the influence of the elastic properties of woven fabric liners on the wear depth of the spherical plain bearings is almost blank. The purposes of this paper are to create an elastic properties analysis model which is suitable for the three commonly used woven fabric liners, to obtain the elastic properties of the plain and stain liners using the method of the tensile test experiment,

and then to validate the analysis model in an experimental way and to investigate the influence of the elastic properties on the wear depth of the spherical plain bearings. We wish to propose some suggestions for liner structural optimizing.

2. Theoretical Analysis of Elastic Properties of the Liner

2.1. Geometric Model of the Woven Fabric Liner. The woven fabric liner is mainly made up of matrix and reinforced fibers, and the fiber distribution of the typical woven fabric liners is shown in Figure 1. A global Cartesian coordinate system (X, Y, Z) is set, where axis X , whose included angle with warp direction is β , is along the horizontal direction, and axes Y, Z are along the directions of fill and thickness of the woven fabric liners, respectively. The angle between the warp and fill directions is γ , the fibers in the warp direction are the mixture of polytetrafluoroethylene (PTFE) and Nomex, and only Nomex fibres are in fill direction. The Nomex fiber is used to improve the strength of the liner materials and bonding properties, while the PTFE fiber is mainly used to improve friction and wear properties of materials. The matrix of the woven fabric liner is phenolic resin.

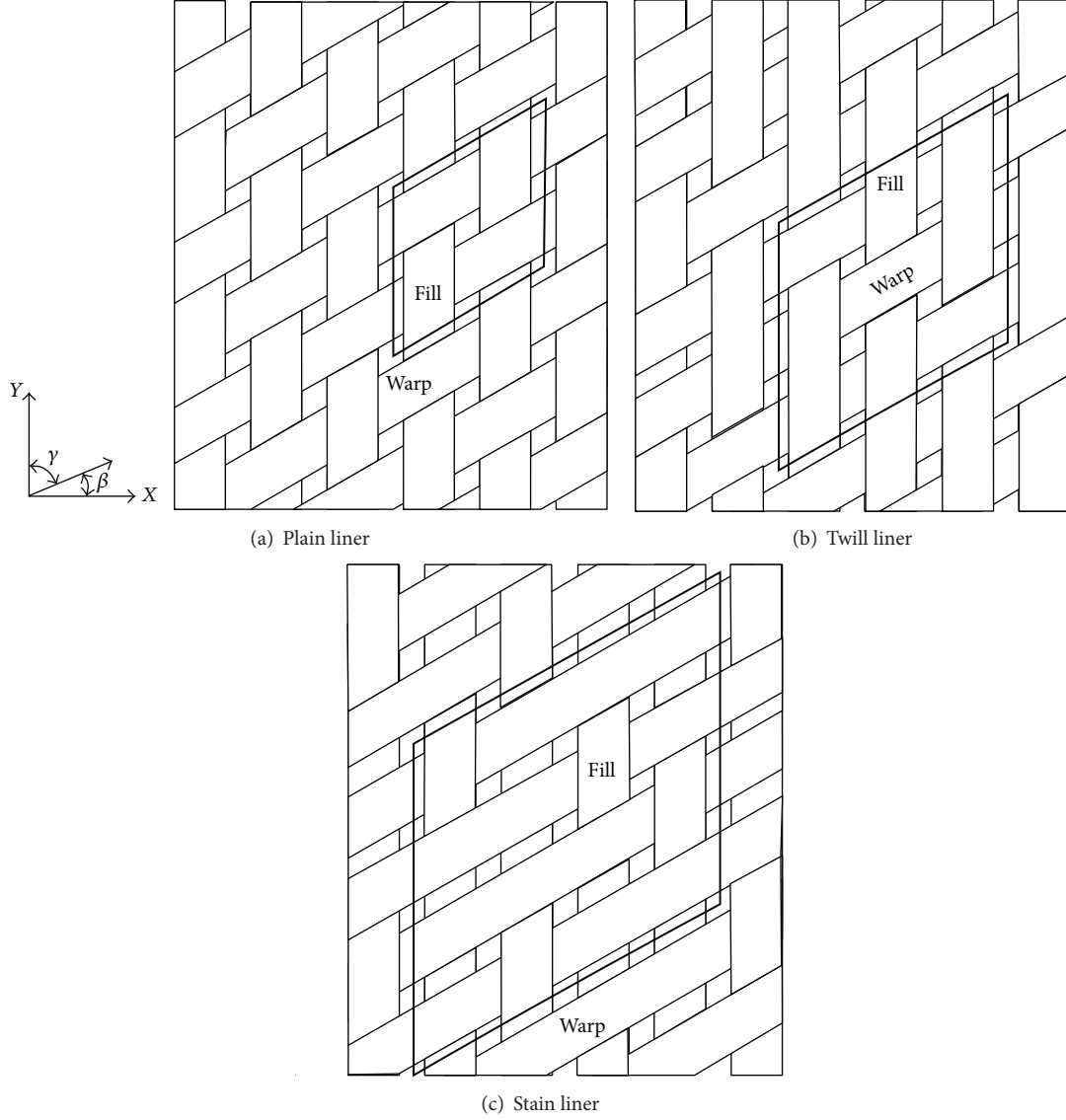


FIGURE 1: Fiber distribution of the woven fabric liner.

Take the black box parts (in Figure 1) of the liners for the analysis units and make the following assumptions of the microstructure of the fabric liners.

(1) The cross section of the yarn is lenticular shape [15]. Its shape and geometric dimensions are shown in Figure 2.

The width w_w and the thickness d_w of the warp yarn after cutting along Y direction can be obtained as

$$w_w = \frac{w}{\sin \gamma}, \quad d_w = d, \quad (1)$$

where w and d represent the width and the thickness of the yarn in the cross section, respectively. The subscript w indicates the warp yarn, and the subscript f will be used in the fill yarn (an exception if it is labeled especially). The warp yarns of the liner are taken as an example, to study here, and the fill yarns could be studied in the similar way.

The radius, R_w , the inner angle, φ_w , and the cross-sectional area, A_w , can be expressed as follows:

$$R_w = \frac{w_w^2}{4d_w} + \frac{d_w}{4}, \quad \varphi_w = 2 \arcsin \left(\frac{2w_w d_w}{d_w^2 + w_w^2} \right), \quad (2)$$

$$A_w = R_w^2 \varphi_w - w_w R_w + \frac{d_w w_w}{2}.$$

(2) Warp and fill yarns have the same fiber directions.

The global coordinate system of the liner is (X, Y, Z) , the coordinate system of the plane of the fiber yarn trace is local coordinate system (u, v, w) , and the coordinate system of the fiber yarn trace is local coordinate system $(1, 2, 3)$. The local coordinate system (u, v, w) is obtained by β angle rotation of the global coordinate system (X, Y, Z) around Z axis, and the coordinate axes of $(1, 2, 3)$ is parallel to the axes of (u, v, w)

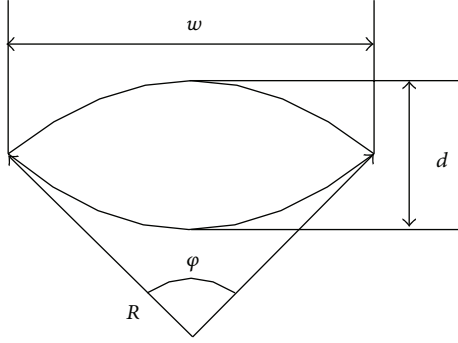


FIGURE 2: Cross section of the fiber yarn.

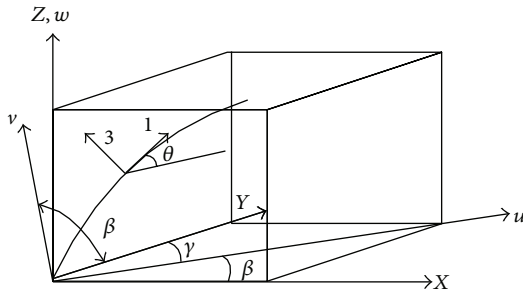


FIGURE 3: Coordinate systems of warp yarn.

after rotating θ angle around v axis. The position relationship of the coordinate systems is shown in Figure 3.

Fibers directions are divided into the straight parts and the curve parts shown in Figure 4. This model applies to plain, twill, and stain fabric liners.

The thickness of two layers of fiber yarns can be written as

$$t = d_w + d_f, \quad (3)$$

where d_f indicates the thickness of the fill yarn after cutting along warp direction.

The bend radius of the yarn can be obtained as

$$r_w = R_f + \frac{d_w}{2}. \quad (4)$$

Yarn-to-yarn distance is

$$Ls_w = 2\sqrt{r_w^2 - R_f^2}. \quad (5)$$

The length of the curve part of the yarn is

$$Lc_w = r_w\phi_f. \quad (6)$$

The length of the warp yarn can be calculated by

$$L_{s/w} = mLs_w + 2Lc_w, \quad m = 0, 1, 2, \quad (7)$$

where $m = 0, 1, 2$ represents plain, twill, and stain woven fabric liner, respectively. The subscript s refers to the fiber

yarn, the subscript w refers to the warp direction, and the meaning of the subscript s/w below is the same as here.

The volumes of the warp yarns in the basic study cell can be obtained as

$$V_{s/w} = \sum_{i=1}^n A_{wi} L_{(s/w)i}, \quad n = 2, 3, 4, \quad (8)$$

where $n = 2, 3$, and 4 correspond to the plain, twill, and stain woven fabric liners, respectively. The meaning of the n below is the same as here; $i = 1$ represents the first warp yarn.

The length of the basic study cell in the warp direction can be written as

$$L_w = nLs_w, \quad n = 2, 3, 4. \quad (9)$$

The volume of the basic study cell is

$$V = L_w L_f h, \quad (10)$$

where L_f indicates the length of the basic study cell in the fill direction, and h represents the thickness of the study cell. Since the thickness of the matrix is very thin, we assume $h = t$.

The volume fraction of the warp yarns in the basic study cell can be obtained as

$$v_{s/w} = \frac{V_{s/w}}{V}. \quad (11)$$

The fiber volume fraction of the warp yarns can be written as

$$\Psi_w = \frac{kA_{f/w}}{A_w}, \quad (12)$$

where k indicates the number of the single fiber in the yarn, $A_{f/w}$ represents the cross-sectional area of the single fiber, and subscripts f and w in f/w refer to the single fiber and warp direction, respectively. The meaning of the subscript f/w below is the same as here.

Accordingly, the fiber volume fraction of the warp direction in the basic study cell can be calculated by

$$\nu_{f/w} = \Psi_w \nu_{s/w} = \frac{kA_{f/w} \sum_{i=1}^n L_{(s/w)i}}{L_w L_f h}, \quad n = 2, 3, 4. \quad (13)$$

2.2. Elastic Properties of the Woven Fabric Liner. The chamis model [16] is used to calculate the elastic constants of the straight part of the yarn. The expressions are as follows:

$$E_{11} = V_f E_{11}^f + V_m E^m, \quad \nu_{12} = V_f \nu_{12}^f + V_m \nu^m,$$

$$E_{22} = \frac{E^m}{1 - \sqrt{V_f} (1 - E^m/E_{22}^f)},$$

$$G_{12} = \frac{G^m}{1 - \sqrt{V_f} (1 - G^m/G_{12}^f)}, \quad (14)$$

$$G_{23} = \frac{G^m}{1 - \sqrt{V_f} (1 - G^m/G_{23}^f)},$$

where 1 is radial direction along the direction of the fiber axis; 2, 3 are traverse directions lying in the plane perpendicular to the fiber; E_{11} and E_{22} are the elastic moduli of fiber yarn along the direction of 1 and 2, respectively; ν_{12} is Poisson's ratio of the fiber yarn of the 1-2 plane; G_{12} and G_{23} are the shear moduli of fiber yarn of the 1-2 and 2-3 planes, respectively; E^m , ν^m , and G^m are the elastic modulus, Poisson's ratio, and shear modulus of the matrix, respectively; E_{11}^f , E_{22}^f , ν_{12}^f , G_{12}^f , and G_{23}^f are the radial elastic modulus, traverse elastic modulus, in-plane Poisson's ratio, in-plane shear modulus,

and 2-3 plane shear modulus of the fiber, respectively; V_f indicates the fiber volume fraction of the yarn, namely, ψ_w in the expression (12).

The curve part of the yarn can be regarded as the assemblage of a number of infinitesimal straight yarn segments. The compliance matrix of the straight part of the warp yarn in the local coordinate system (1, 2, 3) and the transition matrix [16] between any two coordinate systems (x_1, x_2, x_3) and (x, y, z) can be written as

$$S_{ij}^s = \begin{bmatrix} S_{11} & S_{12} & S_{12} & 0 & 0 & 0 \\ S_{12} & S_{22} & S_{23} & 0 & 0 & 0 \\ S_{12} & S_{23} & S_{22} & 0 & 0 & 0 \\ 0 & 0 & 0 & S_{44} & 0 & 0 \\ 0 & 0 & 0 & 0 & S_{55} & 0 \\ 0 & 0 & 0 & 0 & 0 & S_{55} \end{bmatrix}, \quad T = \begin{bmatrix} l_1^2 & l_2^2 & l_3^2 & l_2 l_3 & l_3 l_1 & l_1 l_2 \\ m_1^2 & m_2^2 & m_3^2 & m_2 m_3 & m_3 m_1 & m_1 m_2 \\ n_1^2 & n_2^2 & n_3^2 & n_2 n_3 & n_3 n_1 & n_1 n_2 \\ 2m_1 n_1 & 2m_2 n_2 & 2m_3 n_3 & m_2 n_3 + m_3 n_2 & m_1 n_3 + m_3 n_1 & m_1 n_2 + m_2 n_1 \\ 2n_1 l_1 & 2n_2 l_2 & 2n_3 l_3 & l_2 n_3 + l_3 n_2 & l_1 n_3 + n_1 l_3 & l_1 n_2 + l_2 n_1 \\ 2l_1 m_1 & 2l_2 m_2 & 2l_3 m_3 & l_2 m_3 + l_3 m_2 & l_1 m_3 + l_3 m_1 & l_1 m_2 + l_2 m_1 \end{bmatrix}, \quad (15)$$

where subscripts i and j in S_{ij}^s refer to the row and column, respectively. For the transition matrix T ,

$$l_i = \cos(x_i, x), \quad m_i = \cos(x_i, y), \quad n_i = \cos(x_i, z) \\ i = 1, 2, 3. \quad (16)$$

The compliance matrix of the straight part of the warp yarn in the local coordinate system (1, 2, and 3) can be completely determined by the chamis model, based on the relationship between compliance matrix and elastic constants. The transition matrix T_{w1} between the local coordinate system (1, 2, and 3) and (u, v, w) and T_{w2} between the local coordinate system (u, v, w) and the global coordinate system (X, Y, Z) can be obtained according to transition matrix T . Then the compliance matrix of the warp yarn in the global coordinate system can be derived

$$S_{ij}^{sw} = T_{w2} S_{ij}^s T_{w2}^T, \quad S_{ij}^{cG} = T_{w2} T_{w1} S_{ij}^s T_{w1}^T T_{w2}^T, \\ S_{ij}^{cw} = \frac{1}{\theta} \int_0^\theta S_{ij}^{cG} d\theta, \quad (17)$$

where S_{ij}^{sw} , S_{ij}^{cG} , and S_{ij}^{cw} signify the compliance matrices of the straight part, curve part yarn segment, and curve part yarn in the global coordinate system (X, Y, Z) , respectively.

The compliance matrix of the warp yarn can be written as

$$S_{ij}^w = \lambda_{sw} S_{ij}^{sw} + \lambda_{cw} S_{ij}^{cw}, \quad (18)$$

where $\lambda_{cw} = 2L_{cw}/L_{s/w}$ and $\lambda_{sw} = 1 - \lambda_{cw}$ indicate the length fractions of the curve part and the straight part, respectively.

The compliance matrix of the fill yarn S_{ij}^f can be obtained in a similar way. Since the compliance matrices of the warp

and fill yarns have been obtained, their stiffness matrices can also be obtained by inverting their compliance matrices. Then according to the volume fraction of the fibers in the warp and fill directions, the stiffness matrices of the woven fabric liners of spherical plain bearing with self-lubricating can be calculated by

$$C_{ij}^c = \nu_{f/w} C_{ij}^w + \nu_{f/f} C_{ij}^f + (1 - \nu_{f/w} - \nu_{f/f}) C_{ij}^m, \quad (19)$$

where C_{ij}^w , C_{ij}^f , and C_{ij}^m indicate the stiffness matrices of the warp yarn, fill yarn, and matrix, respectively. $\nu_{f/w}$ and $\nu_{f/f}$ refer to fiber volume fraction of the warp and fill direction, respectively.

The compliance matrix S_{ij}^c of the woven fabric liner can be obtained by inverting stiffness matrix C_{ij}^c , and the nine elastic constants of the liner can be written as $E_{11} = 1/S_{11}^c$, $E_{22} = 1/S_{22}^c$, $E_{33} = 1/S_{33}^c$, $\nu_{12} = -S_{12}^c/S_{11}^c$, $\nu_{23} = -S_{23}^c/S_{22}^c$, $\nu_{13} = -S_{13}^c/S_{11}^c$, $G_{12} = 1/S_{66}^c$, $G_{13} = 1/S_{55}^c$, and $G_{23} = 1/S_{44}^c$.

3. Elastic Properties Test and Validation of the Analysis Model

Experiment specimens include two types of woven fabric liners: one is the plain woven fabric liner with PTFE fibers in both the warp and fill directions; the other is the stain woven fabric liner with PTFE and Nomex fibers in the warp direction and Nomex fiber in the fill direction. The experiment is implemented by Zwick/Roell (BZ2.5/TS1S) test machine. During the experiment, the displacement control mode is used, and the loading speed is 0.2 mm/min. A CCD camera is placed at the normal of the specimen surface to record images while loading. Precision for strain measurement is 50 $\mu\epsilon$. The sequential images are subjected to DIC (digital image correlation) analysis, and then we can acquire the elastic properties of the liners through the corresponding

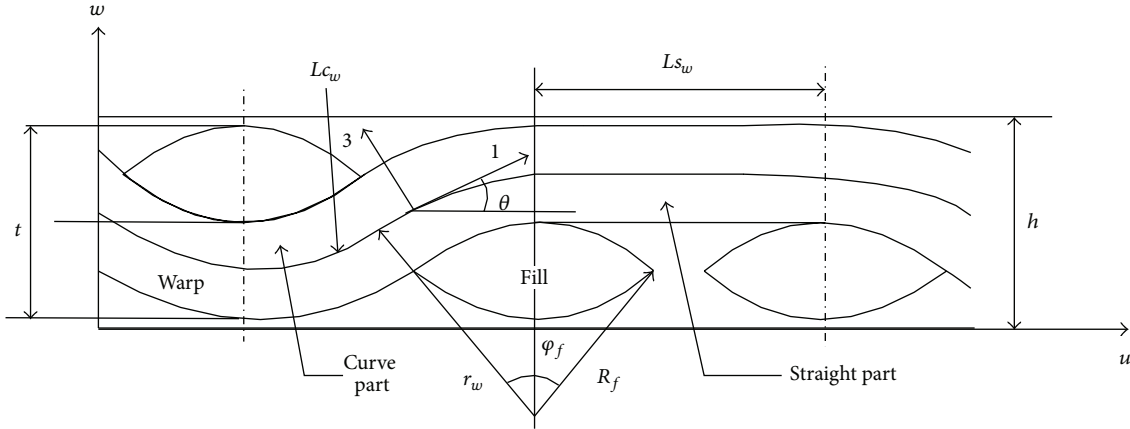


FIGURE 4: Geometric model of fibers directions.

TABLE 1: Geometric parameters of woven fabric composites.

Liner types	Thickness of yarn (mm) (d)		Width of yarn (mm) (w)		Lamina thickness (mm) (h)	Inner angle ($^\circ$) (φ_w)	Fiber volume fraction of the yarn (ψ_w)
	Warp	Fill	Warp	Fill			
Plain/stain liners	0.19		0.51		0.38	90	0.70

TABLE 2: Material elastic properties.

Material	E_{11} (GPa)	E_{22} (GPa)	G_{12} (GPa)	G_{13} (GPa)	ν_{12}
PTFE fiber	0.75	0.75	0.28	0.28	0.30
Nomex fiber	6.70	6.70	2.69	2.69	0.23
Phenolic resin matrix	2.88	2.88	1.01	1.01	0.42

stress-strain curves. The structural and material parameters are shown in Tables 1 and 2 [17]. The elastic properties of plain and stain liners can be calculated by applying the structural and material parameters to Sections 2.1 and 2.2, respectively. The comparison between the computational and experimental results is listed in Table 3. The coordinate system (X, Y, Z) is replaced by (1, 2, and 3) to align with the conventional means of expression.

Table 3 shows that the calculation results of plain woven fabric liner are in good agreement with the experimental data. Relative error of the warp elastic modulus of the stain woven fabric liner is a little bit bigger, but within the scope of the engineering allowable error.

4. Influence of Elastic Properties of the Liner on Wear Depth of Spherical Plain Bearing

Wear simulation was realized by commercial finite element software ABAQUS. Wear simulation program is designed using Python language and the elastic properties of the liner is changed to derive the variation trend of the maximum wear depth of spherical plain bearing after 25000 cycles of oscillating.

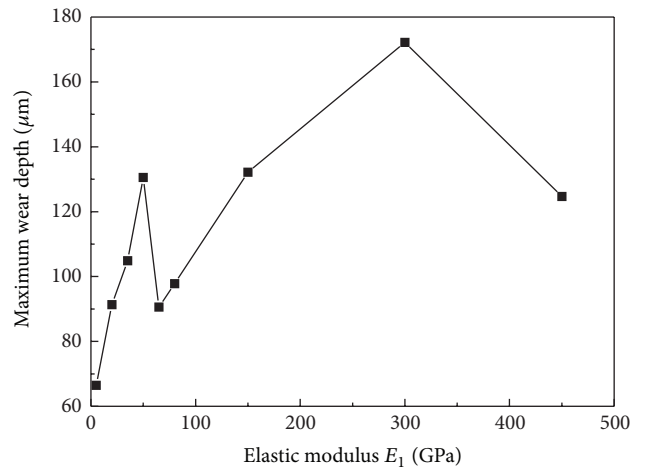


FIGURE 5: Influencing of elastic modulus E_1 on the maximum wear depth.

Figure 5 to Figure 8 are the curves of influencing of the elastic properties on the maximum wear depth of the spherical plain bearing after 25000 cycles of oscillating.

Figures 5 and 6 show that the elastic moduli of the liner have a tremendous impact on the maximum wear depth of the spherical plain bearing. The elastic moduli E_1 (E_2) and E_3 have an opposite influence on the maximal wear depth when they vary from 0 GPa to 65 GPa. With E_1 (E_2) increasing, the maximal wear depth is firstly increased by 96.34% and then decreased by 30.61%. With the increase of E_3 , the maximal wear depth is firstly decreased by 49.31% and then increased by 28.33%. When the elastic moduli are over 65 GPa, the maximal wear depth increases firstly and then decreases and increases with the increase of E_1 (E_2) and E_3 , respectively.

TABLE 3: Comparison between the computational and experimental results.

Liner types	Elastic properties	Computational results	Test results	Error
Plain liner	E_{11} (GPa)	1.95	1.98	1.35%
	E_{22} (GPa)	1.95	1.98	1.35%
	G_{12} (GPa)	0.66	0.63	4.39%
Stain liner	E_{11} (GPa)	3.29	2.96	11.15%
	E_{22} (GPa)	3.36	3.23	4.02%
	G_{12} (GPa)	1.19	1.09	9.17%

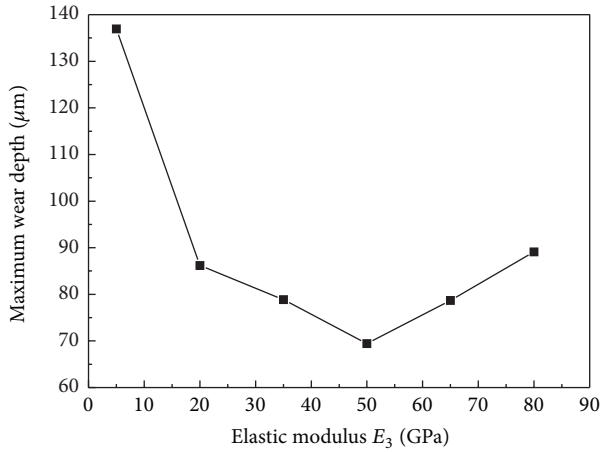
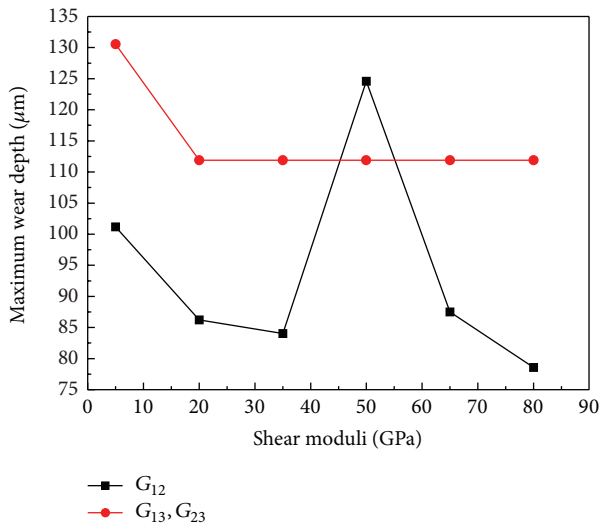
FIGURE 6: Influencing of elastic modulus E_3 on the maximum wear depth.

FIGURE 7: Influencing of shear moduli on the maximum wear depth.

The main movement pattern of the spherical plain bearing is multiaxial rotary oscillating motion in a lower speed, so there is an impact of the in-plane shear performance on wear depth of the spherical plain bearing, which cannot be ignored. As shown in Figure 7, with the shear modulus G_{12} increasing, the maximal wear depth firstly decreases, then increases, and then decreases again. And it varies greatly when the shear

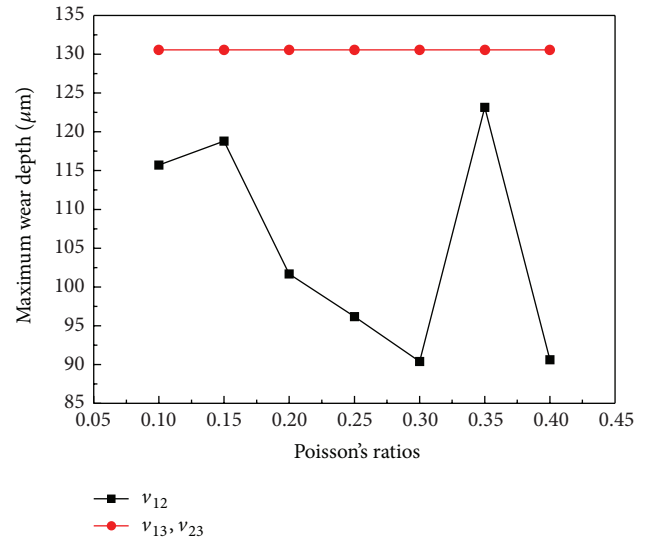


FIGURE 8: Influencing of Poisson's ratios on the maximum wear depth.

modulus G_{12} ranges from 35 GPa to 60 GPa. The maximal wear depth of the bearing almost keeps the same and is under the minimum state when G_{13} and G_{23} change from 20 GPa to 80 GPa.

Figure 8 suggests that the maximum wear depth will increase and decrease when the Poisson's ratio ν_{12} increases in the area of 0.1 to 0.15 or 0.3 to 0.35 and 0.15 to 0.3 or 0.35 to 0.4, respectively. The maximal wear depth will be minimal when Poisson's ratio ν_{12} is 0.3. Poisson's ratios ν_{13} and ν_{23} have no effect on the maximal wear depth.

The wear depth of the spherical plain bearing at predetermined conditions cannot be greater than allowed limit 0.114 mm based on the standard MIL-B-81820. Thus the elastic moduli E_1 and E_2 should change from 0 GPa to 40 GPa or 56 GPa to 113 GPa, E_3 should be greater than 12 GPa, the shear modulus G_{12} should change from 0 GPa to 46 GPa or 54 GPa to 80 GPa, and Poisson's ratios ν_{12} should change from 0.16 to 0.34 or 0.36 to 0.45. Because the elastic constants G_{13} , G_{23} , ν_{13} , and ν_{23} , have a little or no influence on the maximal wear depth, they can be ignored.

5. Conclusions

An elastic property analysis model, which is suitable for three commonly used woven fabric liners, is described in

this paper. The influence of the elastic properties on the wear depth of the spherical plain bearings is further investigated. The following is a summary.

- (1) A general elastic properties analysis model adjusting to the plain, twill, and stain liners was built.
- (2) For the plain woven fabric liner, the computational results of elastic properties are in good agreement with the experimental data, and the relative errors of in-plane elastic and shear moduli are 1.35% and 4.39%, respectively. For the stain woven fabric liner, the relative error of the warp elastic modulus is 11.15%, which is a little larger but within the scope of the engineering allowable error, and the relative errors of fill elastic and in-plane shear modulus are 4.02% and 9.17%, respectively.
- (3) The influence of the liner elastic properties on the wear of the spherical plain bearing was analyzed based on the finite element method. The results show that the liner elastic properties, which are the elastic moduli E_1 (E_2) and E_3 , the shear modulus G_{12} , and Poisson's ratio ν_{12} , have the greater impacts on the maximal wear depth of the woven fabric liner of the spherical plain bearing. The results also show that the shear moduli G_{13} (G_{23}) have a small effect and Poisson's ratios ν_{13} (ν_{23}) have no effect on the liner's wear.
- (4) For the woven fabric liner of the spherical plain bearing based on the standard MIL-B-81820, the elastic moduli E_1 , E_2 should change from 0 GPa to 40 GPa or 56 GPa to 113 GPa, E_3 should be greater than 12 GPa, the shear modulus G_{12} should change from 0 GPa to 46 GPa or 54 GPa to 80 GPa, and Poisson's ratios ν_{12} should change from 0.16 to 0.34 or 0.36 to 0.45, so as to meet the wear requirement of the bearing. The elastic constants G_{13} , G_{23} , ν_{13} , and ν_{23} have a little or no influence on the maximal wear depth; therefore they can be ignored. Above suggestions could be used for the optimal design of the spherical plain bearings based on wear reduction, so as to select the suitable geometric and material parameters of the woven fabric composite.

Conflict of Interests

The authors declare that there is no conflict of interests regarding the publication of this paper.

Acknowledgments

This work is supported by the COSTIND of China (D.50-0109-11-002) and High and New Engineering Program of Shanghai (D.51-0109-09-001). The authors wish to thank Professor Q. Jane Wang at Northwestern University of USA for valuable discussions.

References

- [1] B. C. Kim, D. C. Park, H. S. Kim, and D. G. Lee, "Development of composite spherical bearing," *Composite Structures*, vol. 75, no. 1-4, pp. 231-240, 2006.
- [2] M. F. Fleszar, "Thermal behaviour of teflon/phenolic liners in self-lubricating bearings," *Journal of Thermal Analysis*, vol. 49, no. 1, pp. 219-226, 1997.
- [3] D. Xiang, Z. Yao, and J. Wen, "Experimental investigation on dry frictional behavior of the two self-lubricating composites under heavy loading conditions," *Materials Letters*, vol. 59, no. 18, pp. 2352-2356, 2005.
- [4] Q. Guo, Y.-F. Song, H.-B. Qiao, and W.-L. Luo, "The friction and wear properties of the spherical plain bearings with self-lubricating composite linear in oscillatory movement," *Journal of Wuhan University of Technology*, vol. 19, pp. 86-91, 2004.
- [5] B. j. Pang, S. Y. Du, J. C. Han, X. D. He, and Y. Yan, "Experimental investigation of three-dimensional four-directional braided carbon/epoxy composites," *Acta Materiae Compositae Sinica*, vol. 16, no. 4, pp. 136-141, 1999.
- [6] C.-K. Yang, "Research of mechanical properties of 3D braided composite materials," *Journal of Materials Engineering*, no. 7, pp. 33-36, 2002.
- [7] Z. Xia, C. Zhou, Q. Yong, and X. Wang, "On selection of repeated unit cell model and application of unified periodic boundary conditions in micro-mechanical analysis of composites," *International Journal of Solids and Structures*, vol. 43, no. 2, pp. 266-278, 2006.
- [8] K. Xu and X. Xu, "Prediction of elastic constants and simulation of stress field of 3D braided composites based on the finite element method," *Acta Materiae Compositae Sinica*, vol. 24, no. 3, pp. 178-185, 2007.
- [9] W.-Y. Zhang, Z.-H. Yao, X.-F. Yao, and Y.-P. Cao, "Numerical model of woven fabric composites," *Engineering Mechanics*, vol. 21, no. 3, pp. 55-60, 2004.
- [10] P. Vandeurzen, J. Ivens, and I. Verpoest, "A three-dimensional micromechanical analysis of woven-fabric composites: I. Geometric analysis," *Composites Science and Technology*, vol. 56, no. 11, pp. 1303-1315, 1996.
- [11] J. L. Kuhn and P. G. Charalambides, "Modeling of plain weave fabric composite geometry," *Journal of Composite Materials*, vol. 33, no. 3, pp. 188-220, 1999.
- [12] T. C. Lim, "Elastic stiffness of three-phase composites by the generalized mechanics-of-materials (GMM) approach," *Journal of Thermoplastic Composite Materials*, vol. 15, no. 2, pp. 155-168, 2002.
- [13] R. Wang, J.-K. Wang, and L. Wu, "Prediction for elastic properties of plain weave fabric composites," *Acta Materiae Compositae Sinica*, vol. 19, no. 1, pp. 90-94, 2002.
- [14] L. Wang and Y. Yan, "Micro analysis and experimental study of the elastic properties of braided composites structure," *Acta Materiae Compositae Sinica*, vol. 21, no. 4, pp. 152-156, 2004.
- [15] S.-K. Lee, J.-H. Byun, and S. H. Hong, "Effect of fiber geometry on the elastic constants of the plain woven fabric reinforced aluminum matrix composites," *Materials Science and Engineering A*, vol. 347, no. 1-2, pp. 346-358, 2003.
- [16] Z. M. Huang, *An Introduction to Micromechanics of Composites*, The Press of Science, 2004.
- [17] L. Deters, F. Mueller, and M. Berger, "Self-lubricating dry rubbing bearings-fundamentals and methods of calculation," *Tribology Series*, vol. 41, pp. 183-194, 2003.

Research Article

Regression Analysis of the Effect of Bias Voltage on Nano- and Macrotribological Properties of Diamond-Like Carbon Films Deposited by a Filtered Cathodic Vacuum Arc Ion-Plating Method

Shojiro Miyake,¹ Takanori Shindo,¹ and Masatoshi Miyake²

¹ Nippon Institute of Technology, 4-1 Gakuendai, Miyasiro-machi, Saitama 345-8501, Japan

² School of Management, Tokyo University of Science, Kuki-shi, Saitama 346-8512, Japan

Correspondence should be addressed to Shojiro Miyake; gosaburo@gmail.com

Received 21 September 2013; Accepted 12 December 2013; Published 28 January 2014

Academic Editor: Tianchang Hu

Copyright © 2014 Shojiro Miyake et al. This is an open access article distributed under the Creative Commons Attribution License, which permits unrestricted use, distribution, and reproduction in any medium, provided the original work is properly cited.

Diamond-like carbon (DLC) films are deposited by bend filtered cathodic vacuum arc (FCVA) technique with DC and pulsed bias voltage. The effects of varying bias voltage on nanoindentation and nanowear properties were evaluated by atomic force microscopy. DLC films deposited with DC bias voltage of -50 V exhibited the greatest hardness at approximately 50 GPa, a low modulus of dissipation, low elastic modulus to nanoindentation hardness ratio, and high nanowear resistance. Nanoindentation hardness was positively correlated with the Raman peak ratio I_d/I_g , whereas wear depth was negatively correlated with this ratio. These nanotribological properties highly depend on the films' nanostructures. The tribological properties of the FCVA-DLC films were also investigated using a ball-on-disk test. The average friction coefficient of DLC films deposited with DC bias voltage was lower than that of DLC films deposited with pulse bias voltage. The friction coefficient calculated from the ball-on-disk test was correlated with the nanoindentation hardness in dry conditions. However, under boundary lubrication conditions, the friction coefficient and specific wear rate had little correlation with nanoindentation hardness, and wear behavior seemed to be influenced by other factors such as adhesion strength between the film and substrate.

1. Introduction

Diamond-like carbon (DLC) films have attracted much attention as a surface coating due to their superior tribological properties [1]. DLC films exhibit outstanding tribological properties such as low friction, high hardness, and wear resistance [2]. Furthermore, improvement of the boundary lubrication properties of such films is also expected. For instance, in an attempt to maximize fuel efficiency of automobile engines by decreasing friction, DLC films on the shim of a follower series have been investigated. On comparing the lubrication properties of these films with those of other films, it was observed that hydrogen-free DLC films were readily obtained [3, 4]. In the case of magnetic storage disks, wear and minute friction fluctuation diminishes equipment performance. An extremely thin wear and corrosion resistant

film coated on these surfaces should be considered [5–7]. To achieve high recording density, a durable protective film should be less than 2 nm thick, and to achieve such thicknesses the filtered cathodic vacuum arc (FCVA) technique has been studied extensively [8–10].

Many methods have been applied to depositing DLC films. Films produced by the plasma chemical vapor deposition (CVD) method contain hydrogen; therefore to avoid this physical vapor deposition (PVD) methods such as arc ion plating (AIP) have been applied. When solid carbon is used as the vapor source, little hydrogen is found in the films. AIP is applied when there is a desire to improve the hardness and adhesion of the films using high energy plasma. With AIP, it is possible to deposit a tetrahedral amorphous carbon (ta-C) thin film, which is employed in the fabrication of automobile sliding parts and films that protect magnetic

heads at a high speed. However, a disadvantage of AIP is that the surface roughness will be increased due to the deposition of macroparticles. In order to overcome this problem, a filter has been used in film deposition. Since FCVA was first reported as an efficient method for depositing high-quality hard coatings free of macroparticles, DLC films deposited by the FCVA method have generated considerable interest as coating materials [11, 12]. Ion energy controlled by substrate bias is an important parameter in determining the properties of films deposited via the FCVA technique. The hardness and Young's modulus values for a ta-C film deposited at an ion energy of 75 eV were 59 and 507 GPa, respectively [12].

In this study, DLC thin films were deposited via FCVA ion plating under both DC and pulse bias voltages. Then, the relationships between the structures and nano- and macrotribological properties of FCVA-DLC films deposited at various bias voltages were evaluated by regression analysis.

2. Materials and Methods

2.1. Deposition of DLC Films. DLC films were deposited by FCVA plating with a bended filter, a graphite target, and argon gas. The substrate was subjected to DC and pulse bias voltages during film deposition. To deposit smooth DLC films, the bended filter was applied to arc plasma from a graphite target. The high density arc plasma was applied while the target was irradiated. During this time, macroparticles were removed by the magnetic field through the pipe bended filter. For depositing films, a bias voltage, DC bias voltage from -50 to -200 V, or pulse bias voltage from -0.5 to -2.0 kV was applied on the substrate. The DLC films were also deposited under floating voltage and ground without bias voltage and were then compared with biased DLC films. To avoid the influence of surface roughness, the silicon (100) substrate was polished to give a mirror finish. The above-mentioned conditions resulted in a film thickness of approximately 200 nm and are listed in Table 1.

To clarify the structure of the FCVA-DLC film [12], Raman spectral measurements ($200\text{--}2000\text{ cm}^{-1}$) were carried out [13] with a LabRAM Horiba Jobin Yvon spectrometer equipped with a CCD detector and a He-Ne laser (532 nm) at 5 mW. All samples were analyzed at an exposure time of 100 s and with an aperture hole of $100\text{ }\mu\text{m}$.

2.2. Evaluation of Nanoindentation Properties. Nanoindentation tests were carried out to evaluate the mechanical properties of FCVA-DLC films by atomic force microscopy (AFM: digital instrument with hysitron digital instrument). The Berkovich diamond indenter, which is a three-sided pyramid, was used with a load of $300\text{ }\mu\text{N}$ and a tip radius of approximately 200 nm. During the experiment, both the loading and unloading times were 5 s. Maximum plastic deformation depth was evaluated from the nanoindentation curve, and the contact area (A_r) encircled by load curve, unload curve, and X -axis was calculated. Then, hardness H was calculated as follows:

$$H = \frac{P}{A_r}, \quad (1)$$

TABLE 1: Deposition condition.

Bias	Direct current	-50 to -200 V
	Pulse bias	-0.5 to -2.0 kV
	Ground, floating	
		Film thickness: ~ 200 nm

where P is the applied load in the measurement. Young's modulus E was obtained on the basis of inclination of the unloading curve in the nanoindentation test and the plasticity index [14] was defined as follows.

To clarify the deformation mechanism of FCVA-DLC films, an energy analysis of nanoindentation was performed [15]. Total deformation energy was calculated using the integral of the loading curve. Storage energy was calculated using the integral of the unloading curve and dissipated energy was calculated as the remainder of total energy minus the storage energy. The modulus of dissipation was calculated by dividing the dissipation energy by the total energy.

2.3. Nanowear Test. A nanowear test was performed to evaluate wear resistance at the nanometer scale using AFM [2, 11, 16] as shown in Figure 1(a). The tip was supported by a parallel-leaf spring unit with a small spring constant. The diamond tip was slid against the specimen surface by lead zirconate titanate (PZT) scanner, which moved the sample for contact, loading, and scanning. Samples coated with DLC films were scanned by this scanner and the test conditions were as follows: the radius of the Berkovich diamond indenter tip was nearly 200 nm, the load was $30\text{ }\mu\text{N}$, the scan range was $500 \times 500\text{ nm}^2$, and the friction speed was $4.0\text{ }\mu\text{m/s}$. After the wear test, the nanowear volumes were measured by AFM from the change in surface profile measured at a load less than $1\text{ }\mu\text{N}$. Then, the wear average depth was evaluated.

2.4. Tribological Test. A ball-on-disk type friction test was carried out to evaluate the tribological properties of FCVA-DLC films as shown in Figure 1(b). By rotating the sample with the application of a specific load on a 6 mm diameter SUS440C ball indenter, we measured the friction force using a strain gauge type friction sensor. The tribological properties of these DLC films under dry and boundary lubrication conditions were investigated. The dependence of frictional properties on rotation cycles was evaluated under conditions of a load of 5.0 N, a rotation speed of 100 rpm, a rotation radius of 4 mm, and a total number of rotating cycles of 6000. The velocity was approximately 31.4 mm/s . The testing temperature was maintained near 293 K. After the friction test, the wear traces of the samples were observed using an optical microscope and three-dimensional profile meter. Moreover, to investigate the boundary lubrication properties of DLC films, Z-20 lubricant with molybdenum dithiocarbamates (MoDTC) and water were used.

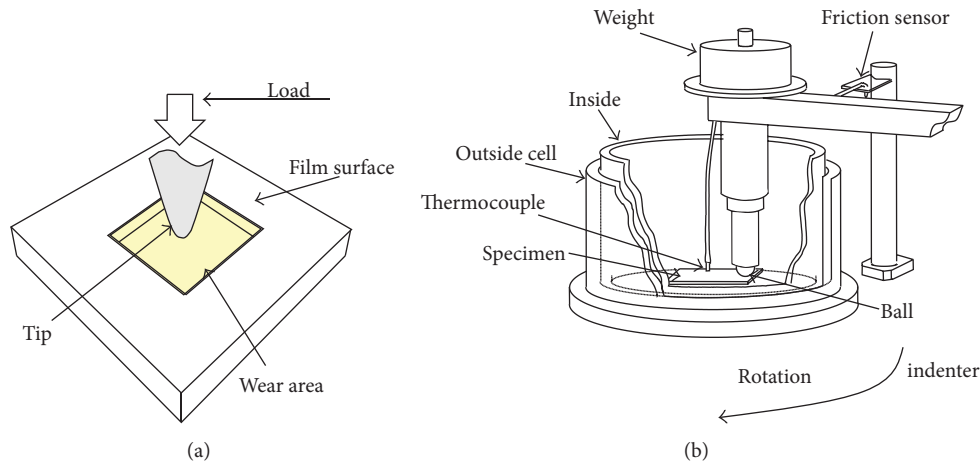


FIGURE 1: Schematic diagrams for (a) nanowear and (b) ball-on-disk tribotests.

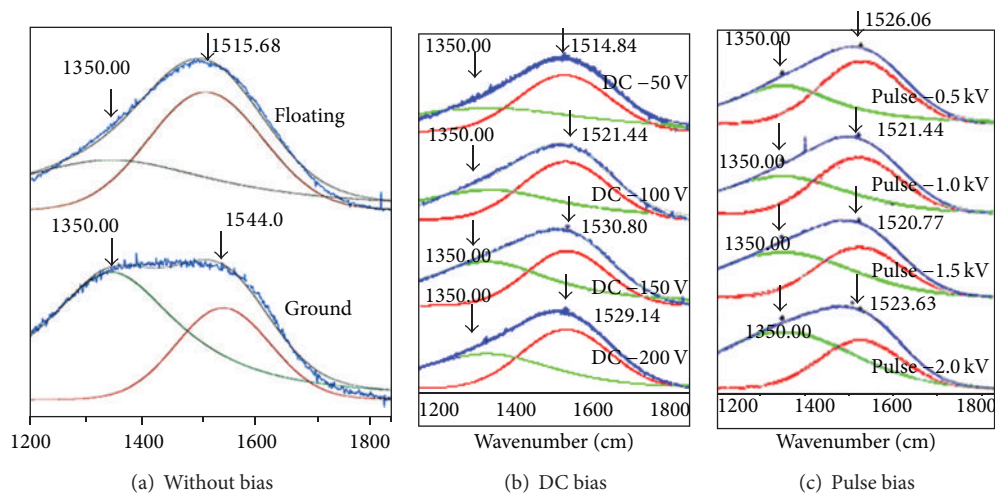


FIGURE 2: Raman spectra of DLC films deposited at various bias voltages.

3. Results and Discussion

3.1. DLC Film Roughness and Structure

3.1.1. Surface Roughness. To examine the surface roughness created by the macroparticles produced during DLC film deposition, surface profiles of coated samples were observed with AFM. Maximum roughness, S_y , and center-line average roughness, S_a , were evaluated. The roughness values of the DLC film deposited with ground were the highest at 5.3 nm S_y and 0.4 nm S_a , whereas those of the DLC film deposited with floating voltage were low at 1.5 nm S_y and 0.18 nm S_a . Under the floating condition, self biased voltages were induced. When the direct current bias voltage was applied during deposition, the surface roughness values were 1.5 nm S_y and 0.15 nm S_a . For DLC films deposited under pulse bias voltage, the roughness values were 1.8 nm S_y and 0.18 nm S_a . These results show that the macroparticles produced during deposition were removed by filtering and the roughness of DLC films deposited under both direct and pulse bias voltages were less than 2.0 nm S_y and 0.2 nm S_a .

3.1.2. Raman Spectra. Figure 2 shows the Raman spectra of DLC films prepared by the FCVA method with different target bias voltages. For all FCVA-DLC films deposited with pulse, floating, and DC bias voltages, the intensity of the peak at approximately 1580 cm^{-1} (Graphite- (G-) band) was higher than that of FCVA-DLC films deposited with ground. For these FCVA-DLC films, except the DLC film deposited with ground, the G-band peak intensity was very low, and no significant Disorder- (D-) band peak at approximately 1350 cm^{-1} was observed. However, for films deposited with ground, the intensity of the G-band peak was higher than those of other FCVA-DLC films. The G-band peak was due to the motion of the sp^2 carbon in the graphite plane, and the D-band peak was due to the disorder of the structure. In addition, the G-band peak appeared to shift to the left with increasing bias voltage due to the distortion of atom bonds. Figure 3 illustrates the dependence of I_d/I_g and G position on bias voltage. The I_d/I_g of a DLC film deposited with ground was as high as 2.5. I_d/I_g decreased to nearly 1.0 with the addition of bias voltage. Moreover, I_d/I_g slightly increased with an increase in the DC bias voltage. DLC films

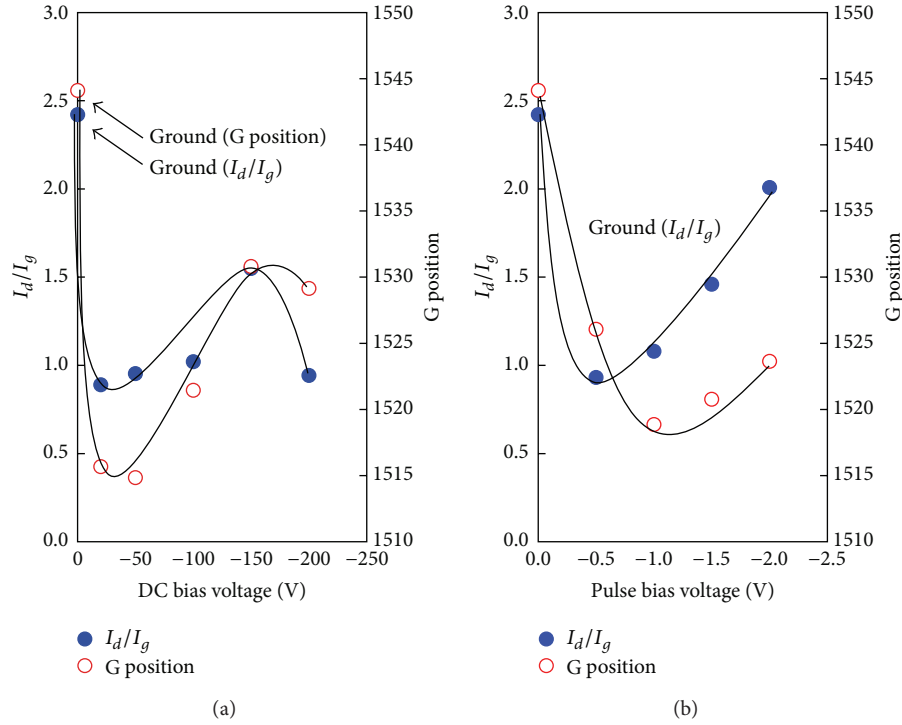


FIGURE 3: Effects of (a) DC bias voltage and (b) pulse bias voltage on I_d/I_g and G position.

deposited at floating voltage showed low values of I_d/I_g due to their self-biased voltage. For pulse bias voltage, I_d/I_g was as low as 1.0 at -0.5 kV and then increased with the pulse peak voltage. On the other hand, the G position was the lowest at 1515 cm^{-1} with floating and -50 V DC bias voltage. For pulse bias voltage, the G position showed a similar trend as I_d/I_g and was low at -1 kV. The background noise caused by the polymeric structure in these films was also low, because the FCVA-DLC films were deposited via a hydrogen-free process. These results show that the FCVA-DLC films deposited with bias voltage contain significant sp^3 bonding structures [12, 13].

3.2. Nanoindentation Properties. Nanoindentation hardness, H , is defined as the resistance to plastic deformation per unit area. Elastic modulus (E)/ H was evaluated because E/H is the material parameter indicating the index of plasticity; thus, E/H corresponds to the ease of plastic deformation. The average H and E/H values in this study are summarized in Figure 4. The H values of DLC films with floating voltage and with ground were 45 and 29 GPa, respectively. DLC films deposited with DC bias voltage had higher H than those of DLC films with ground. The DLC films exhibited a maximum H of approximately 50 GPa when the DC bias voltage was -50 V, and the hardness of these films decreased with increasing DC bias voltage. For the pulse bias voltage, DLC films had a maximum hardness when the peak voltage was -0.5 kV, and then, hardness decreased with increasing peak voltage. The proper bias voltages for high hardness were obtained under both DC and pulse bias voltages. The same

test was carried out on the DLC films deposited by electron beam ion plating and by sputtering, and H values of both were approximately 20 GPa. The H value of the silicon substrate was 13 GPa.

The scatter diagram of the modulus of dissipation and E/H dependence on H is shown in Figure 5. A high positive correlation was observed between the modulus of dissipation, E/H , and H , because their correlation coefficient R and coefficient of determination R^2 were as high as 0.82 and 0.65, respectively. The relationships between the moduli of dissipation in these nanoindentation tests are expressed, as shown in Figure 5.

All tested DLC films deposited with ground, floating, and DC and pulse bias voltages can be expressed in one mastering curve. The hardest -50 V DC biased DLC film showed a low modulus of dissipation and E/H . Therefore, these FCVA-DLC films show excellent resistance to plastic deformation. Moreover, when the DC bias voltage was reduced from -50 V to -150 V, the modulus of dissipation and E/H increased. The modulus of dissipation and E/H of DLC films deposited with ground were larger than those of the other films. The modulus of dissipation of DLC films deposited with ground and with -2.0 kV pulse peak voltage was approximately 25% and 28%, respectively. Under the same test conditions, the modulus of dissipation of the DLC films deposited by electron beam ion plating was approximately 25%, which is similar to that of DLC films deposited with ground.

For very hard materials, it is difficult to induce plastic deformation. The value of E/H ranges from 14 to 20 for conventional materials such as metals. In the case of the DLC films deposited with bias voltage by an FCVA method,

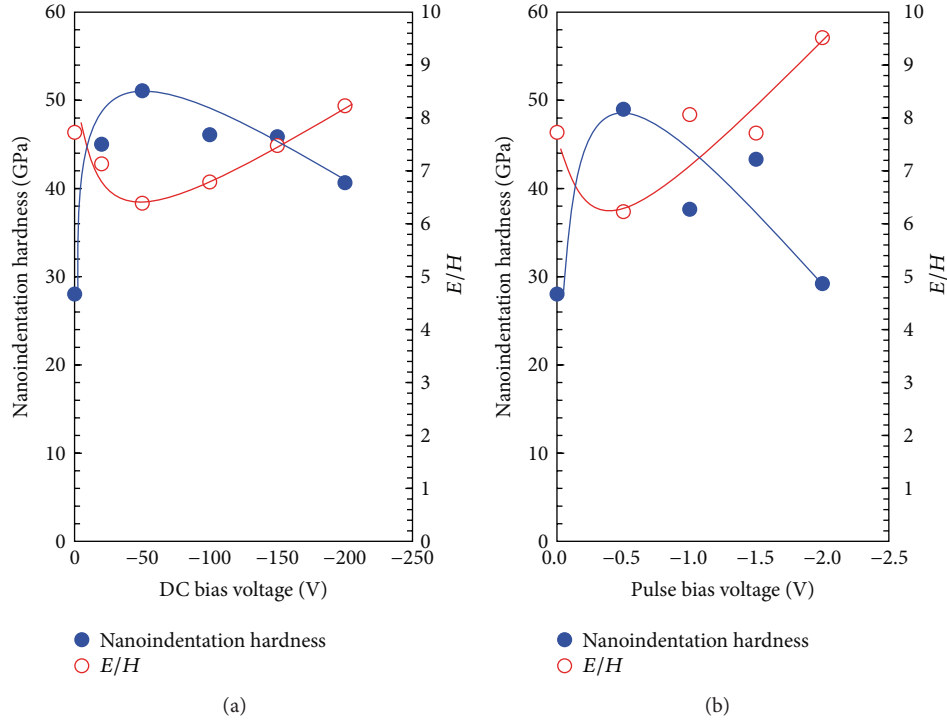


FIGURE 4: Effects of (a) DC bias voltage and (b) pulse bias voltage on nanoindentation hardness (H).

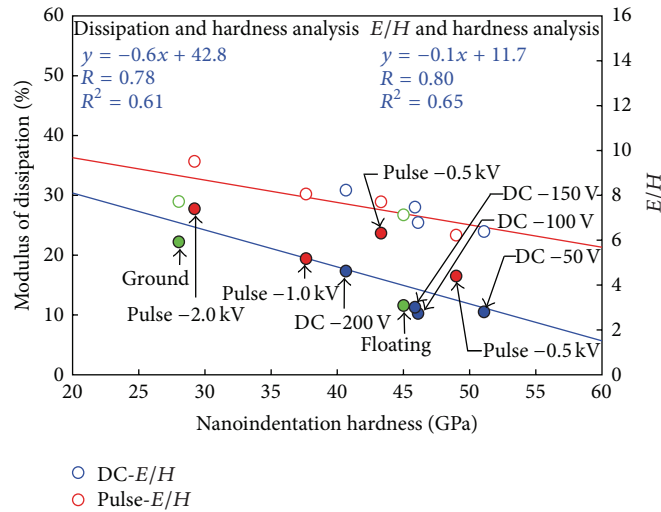


FIGURE 5: Scatter diagram of modulus of dissipation, E/H , and H for DLC films deposited with 10 different bias voltages.

the value of E/H was very small, about 10.0. From the results of the nanoindentation test, we conclude that the DLC films deposited by the FCVA method exhibit superior resistance to plastic deformation.

3.3. Nanowear Properties. A nanowear test was carried out by AFM to evaluate the dependence of nanowear resistance properties of the FCVA-DLC films on bias voltage. Figure 6(a) shows the nanowear profiles of DLC films deposited with -50 V DC (A) and -1.5 kV pulse (B) bias

voltage compared with ground (C). A quantificational analysis was carried out to evaluate the wear depth of an atomic order. The histograms of the profiles near the wear areas were calculated. For each DLC film, two peaks corresponding to the top surface and the surface of the wear groove were obtained as shown in Figure 6(b). The wear depth was estimated from the distance between central values of these two peaks. The atomic radius of carbon is approximately 0.07 nm, and according to this method the atomic scale of wear depth can be evaluated. For DLC films deposited with ground, the peak of the top surface was broad due to the

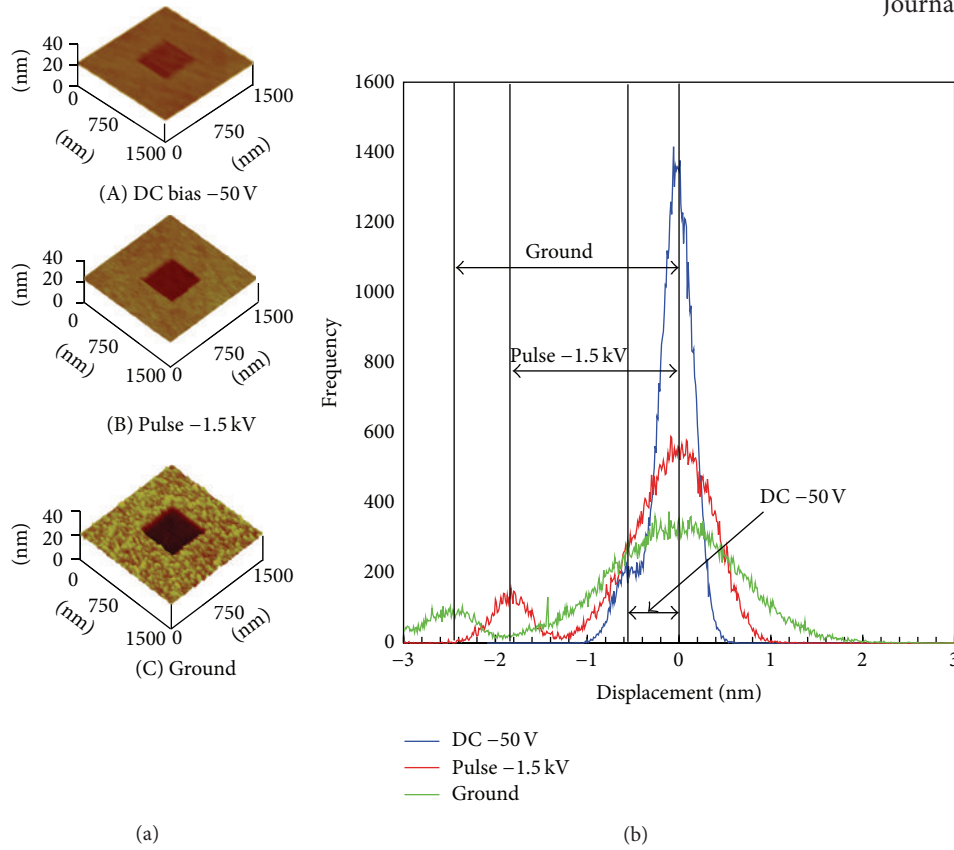


FIGURE 6: Nanowear profile and histogram of wear surfaces.

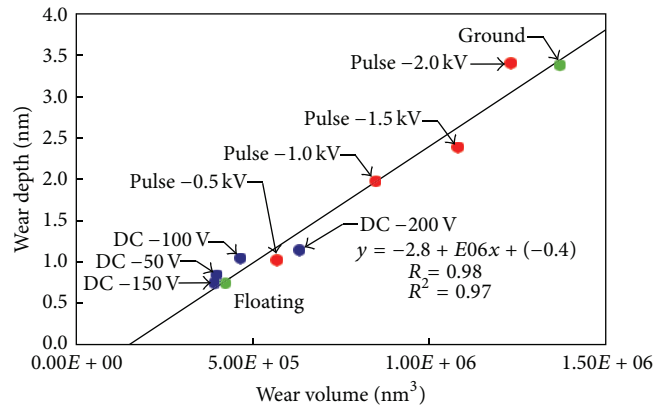


FIGURE 7: Scatter diagram of wear depth and wear volume for DLC films deposited with 10 different bias voltages.

large surface roughness, and the peak of bottom surface was separated from the top surface due to the deep wear depth. By contrast, on DLC films prepared with DC -50 V, the wear groove is flat and the surface roughness is low. Nearly 0.6 nm differences between the two peaks of these DLC films were observed. For the DLC film deposited with -1.5 kV pulse bias voltage, the wear depth was 1.8 nm, whereas for those deposited with ground the wear depth was 2.5 nm.

Figure 7 shows the scatter diagram of wear depth and wear volume for films deposited with the 10 different bias voltages. A high positive correlation was found between wear depth and wear volume, and the correlation coefficient was

$R = 0.91$. The wear depths of films deposited with pulse bias voltage were slightly greater than those of films deposited with DC bias voltage. The wear depths of DLC films deposited with both -2.0 kV pulse bias voltage and ground exhibited similar large values. Figure 8 shows the scatter diagram of wear depth and H for films deposited with the 10 different bias voltages. A strong negative correlation was found between wear depth and H , and the correlation coefficient was $R = 0.87$. The extremely thin wear depths, which were less than 4 nm, reveal that the clear differences in the nanotribological properties of films deposited under different conditions can be evaluated.

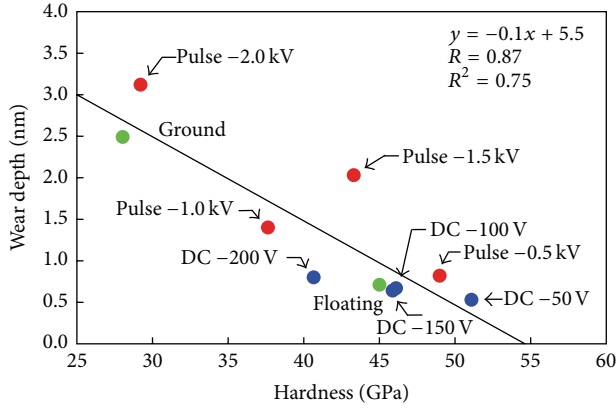


FIGURE 8: Scatter diagram of wear depth and nanoindentation hardness for DLC films deposited with 10 different bias voltages.

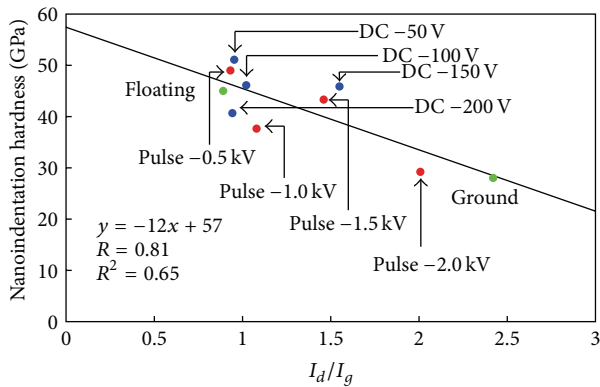


FIGURE 9: Scatter diagram of nanoindentation hardness and I_d/I_g for DLC films deposited with 10 different bias voltages.

The scatter diagram of I_d/I_g and H for films deposited with the 10 different bias voltages is shown in Figure 9. H decreased with increasing I_d/I_g , and a strong negative correlation was identified between H and I_d/I_g , with a correlation coefficient as high as $R = 0.81$. By contrast, H and G position were less correlated, with a correlation coefficient of $R = 0.56$.

The scatter diagram of nanowear depth and I_d/I_g for films deposited with the 10 different bias voltages is shown in Figure 10. A strong positive correlation was observed between nanowear depth and I_d/I_g , with a correlation coefficient as high as $R = 0.82$. These results show that the nanotribological properties such as H and nanowear resistance are highly correlated with I_d/I_g and highly dependent on the nanostructures of the films.

3.4. Tribological Properties Evaluated by Ball-on-Disk Tribotest. Using a ball-on-disk type tribotester, the frictional properties of the DLC films were evaluated under dry and boundary lubrication conditions.

3.4.1. Frictional Properties under Dry Conditions. Figure 11 shows the relationship between the friction coefficient and the number of sliding cycles under dry conditions. For

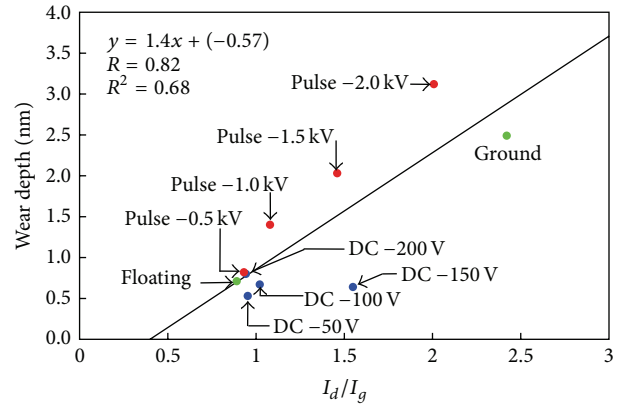


FIGURE 10: Scatter diagram of wear depth and I_d/I_g for DLC films deposited with 10 different bias voltages.

the DLC films deposited with ground, the friction coefficient increased with the number of sliding cycles, with a friction coefficient as high as 0.3~0.5. The friction coefficient of the DLC films deposited with floating voltage showed a minimum value at 0.2. The friction coefficients of the DLC films deposited with both DC and pulse bias voltages were approximately 0.2~0.3. These friction coefficients decreased and then became saturated with additional sliding cycles.

Figure 12 shows the dependence of the average friction coefficient of DLC films on bias voltage. DLC films deposited with floating voltage exhibited the lowest friction coefficient among all the samples. For DLC films deposited with -1.0 kV pulse bias voltage, the friction coefficient was also low and was similar to that for DLC films deposited with floating voltage.

3.4.2. Frictional Properties under Boundary Lubrication Conditions with Z-20 and Modifier (MoDTC) Lubricant. Evaluation of boundary lubrication properties was carried out using Z-20 with added modifier (MoDTC) lubricant. The average friction coefficients of DLC films are shown in Figure 13. DLC films deposited with all DC bias voltages and the ground exhibited low friction coefficients, which were near 0.1. The lowest friction coefficient of DLC films deposited at -150 V was nearly 0.09. For DLC films deposited with pulse bias voltage, friction coefficients were slightly higher at approximately 0.1~0.12. DLC films deposited with -1.0 kV pulse bias voltage showed the highest friction coefficient value at approximately 0.12.

3.4.3. Friction Properties under Boundary Lubrication with Refined Water. Under boundary lubrication with refined water, the friction reduction effect was less than that obtained using the Z-20 with MoDTC lubricant as shown in Figure 14. The change in friction properties compared to those obtained under dry conditions was different with refined water. For example, the friction coefficient of DLC films deposited with floating voltage was high at approximately 0.35. By contrast, under dry conditions the friction coefficient was the lowest. For films deposited with floating voltage, the

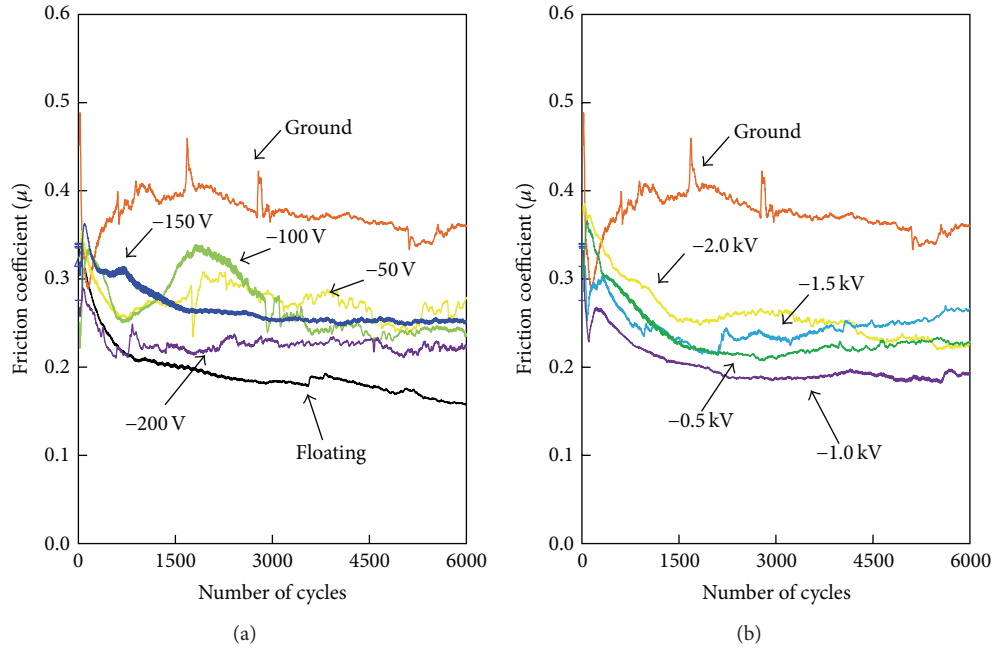


FIGURE 11: Friction properties of various biased DLC films deposited with (a) DC bias and (b) pulse bias voltage (load: 5.0 N, dry conditions).

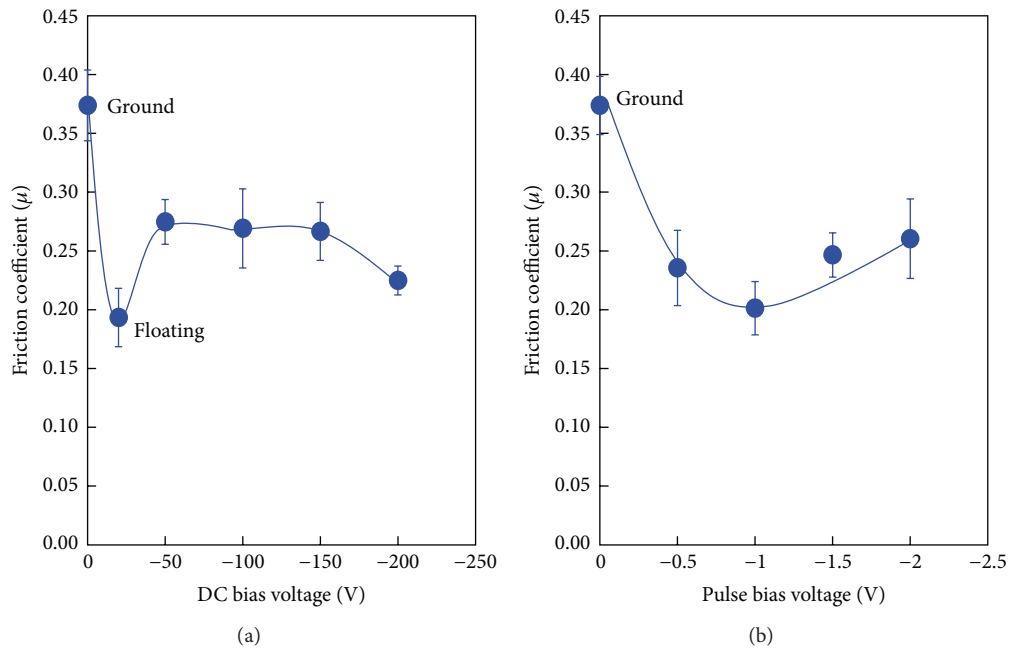


FIGURE 12: Average friction coefficient of DLC films under dry conditions.

friction exhibited inconsistent fluctuation at the beginning of the experiment. The friction coefficient of DLC films deposited with DC bias voltage was stable at approximately 0.15. The lowest friction coefficient of 0.1 was observed for DLC films deposited with ground. In addition, the average friction coefficients of DLC films deposited with pulse bias voltage were greater than those for DLC films deposited with DC bias voltage. Overall, the friction coefficients fluctuated inconsistently from 0.2 to 0.4, similarly as

under dry conditions. The friction coefficient of DLC films deposited with -1.0 kV pulse peak voltage reached as high as 0.4 and then decreased with an increase in peak voltage.

3.4.4. Damage to DLC Films after Friction Testing. Under dry conditions, no visible damage to most of the FCVA-DLC film-coated samples was observed. Figure 15 shows an example of wear tracks formed with the use of Z-20 with MoDTC lubricant. The damage to DLC films deposited

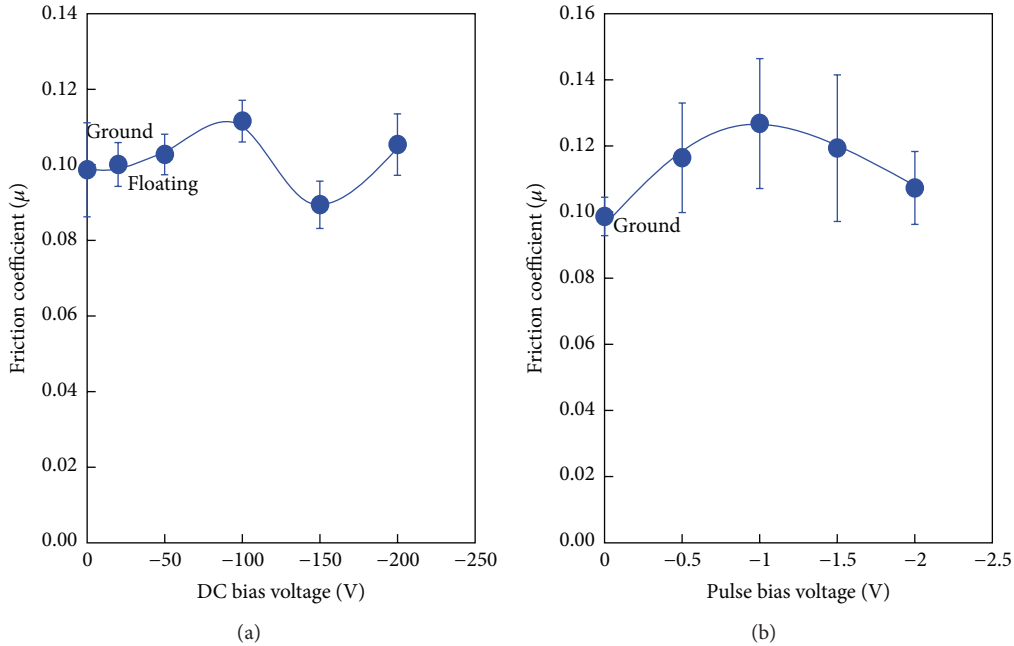


FIGURE 13: Average friction coefficient of DLC films deposited with (a) DC bias and (b) pulse bias voltage under lubrication using Z-20 with MoDTC.

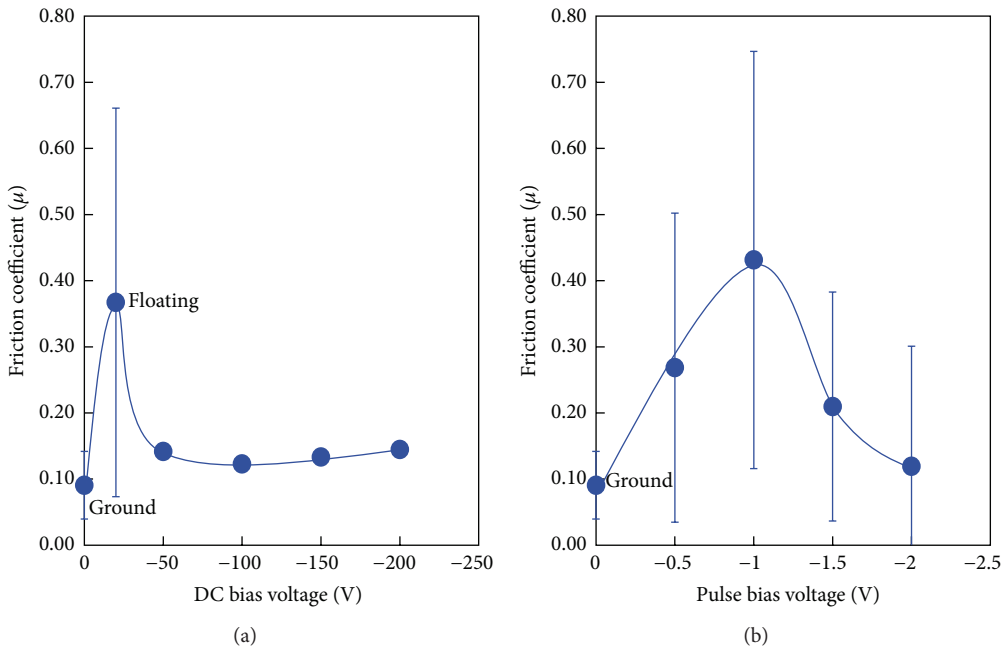


FIGURE 14: Average friction coefficient of DLC films deposited with (a) DC bias and (b) pulse bias voltage under lubrication using refined water.

with DC bias voltage and floating voltage was difficult to observe under an optical microscope. By contrast, clear damage to DLC films deposited with pulse bias voltage and ground was observed. Under water boundary lubrication, less damage was observed on DLC films deposited with DC bias voltage than on the others as shown in Figure 16. On the other hand, DLC films deposited with pulse bias voltage,

ground, and floating voltage showed considerable damage, especially those deposited with ground, which showed the most damage. Under lubrication with motor oil or water, severe wear damage was formed by friction. This deduced that peeled hard and brittle films act as abrasives.

The damaged states of the tested DLC films are summarized in Table 3. The extent of damage caused was divided

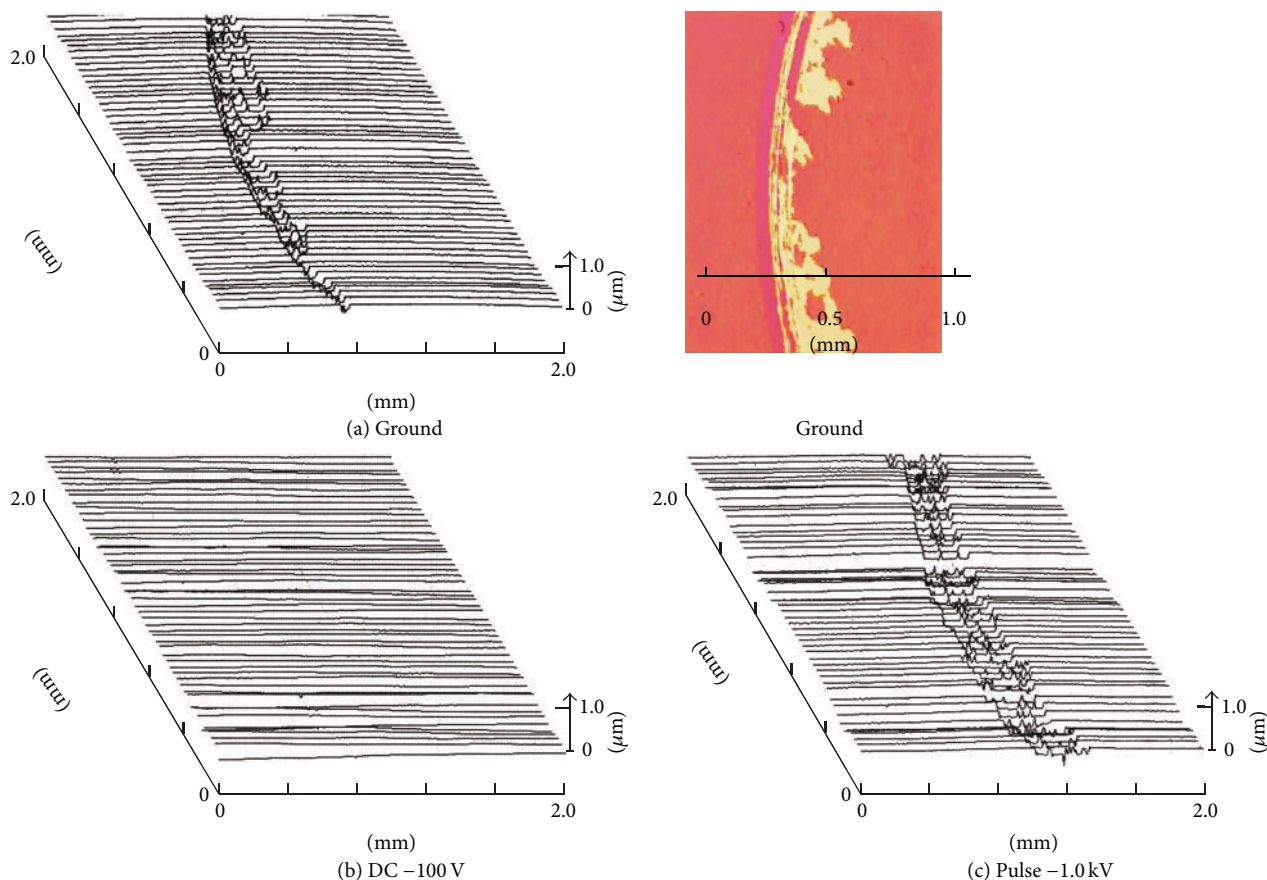


FIGURE 15: Wear profiles of DLC films deposited with (a) ground, (b) DC at -100 V, and (c) pulse bias at -1.0 kV under lubrication using Z-20 with MoDTC.

into three levels. At the first level, the damage could be observed clearly by optical microscopy, and the profile measurement was expressed as severe damage, \times . At the second level, the damage was difficult to observe by optical microscopy, and the profile measurement was expressed as slight damage, Δ . At the third level, the damage could not be observed by optical microscopy, and the profile measurement was expressed as no damage, \circ . In particular, DLC films deposited with DC bias voltages showed superior wear resistance under dry, water, and oil boundary lubrication conditions.

3.4.5. Correlation of Nano- and Macrotribological Properties.

Generally, the friction coefficient depends on hardness and Young's modulus. The scatter diagram of friction coefficients shows dependence on hardness and Young's modulus for the 10 types of DLC films deposited with bias voltage under dry conditions, and a negative correlation between the friction coefficient and hardness is shown in Figure 17. The correlation coefficients, R , of the friction coefficient with hardness and with E was as large as 0.47 and 0.69, respectively, as shown in Figure 10. This decrease in friction coefficient is attributed to the decrease in the contact area with increasing hardness and Young's modulus. Under Z-20 with MoDTC and water boundary lubrication, the regression between the friction

TABLE 2: Friction and lubrication properties test conditions.

Load	5.0 N
Sliding speed	31.4 mm/s
Ball indenter	ANSI 440 C (radius = 3.0 mm)
Environment	Dry condition
	Water lubrication (refined water)
	Motor oil lubrication (Z-20; MO-DTC containing)

coefficient and H is very weak. Under boundary lubrication, the friction coefficients were influenced by surface damage (Table 2).

There is little correlation between the specific wear rate and H of the prepared FCVA-DLC films. The damage to DLC films deposited without bias voltage was considerable, and the damage to DLC films deposited with pulse bias voltage was greater than that observed on films deposited with DC bias voltage. Therefore, the specific wear rates determined in the friction test seemed to be affected by other factors such as the adhesion strength between the DLC films and the substrate.

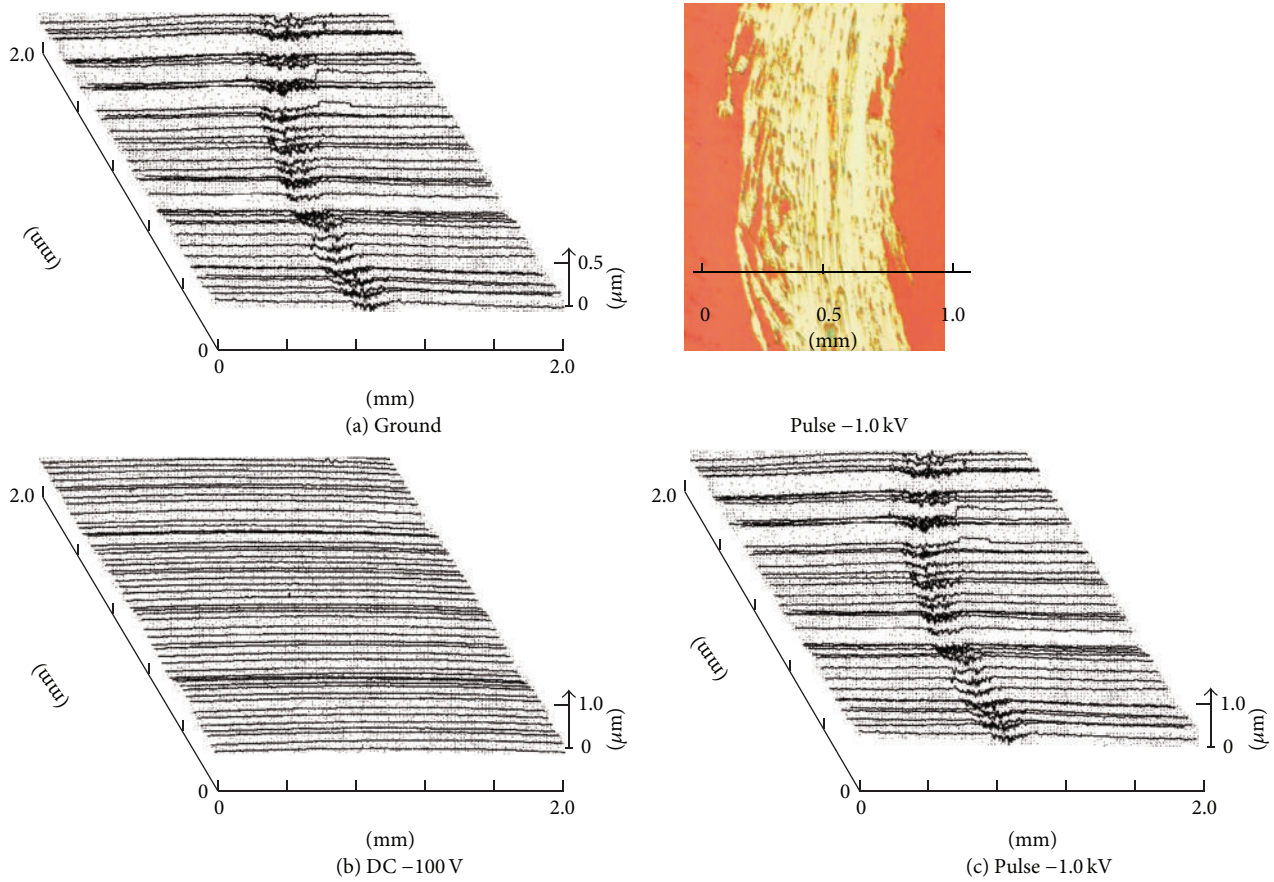


FIGURE 16: Wear profiles under lubrication using water for DLC films deposited with (a) ground, (b) DC at -100 V, and (c) pulse bias at -1.0 kV.

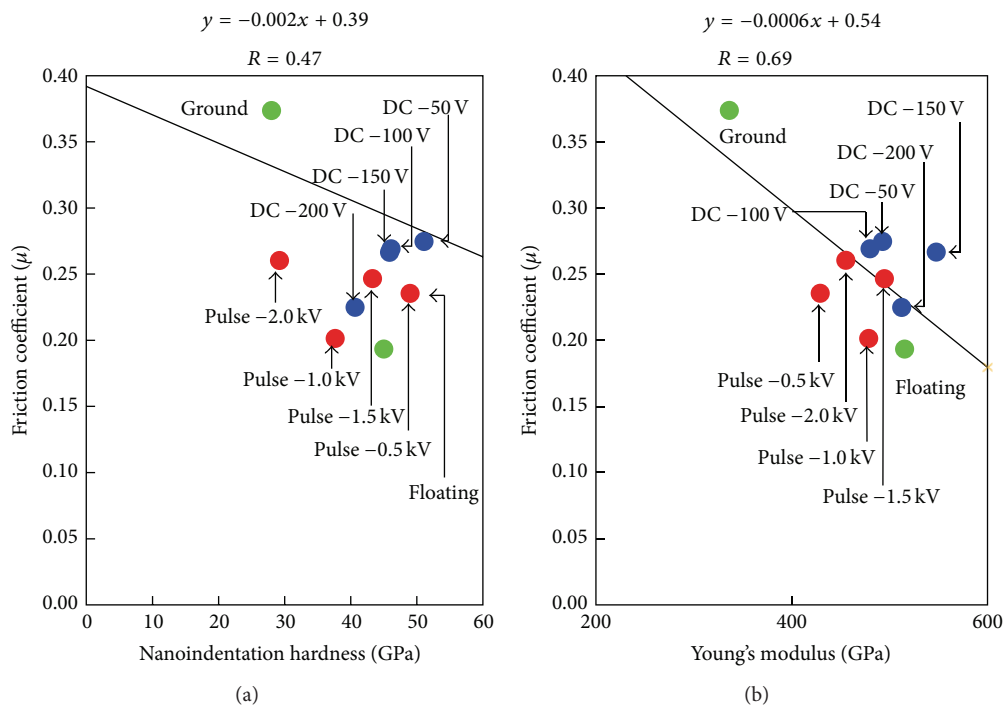


FIGURE 17: Scatter diagram of friction coefficient, nanoindentation hardness, and Young's modulus.

TABLE 3: Sliding damage and specific wear rate (nm^2/N).

	DC					Pulse			Ground	Floating
	-50 V	-100 V	-150 V	-200 V	-0.5 kV	-1.0 kV	-1.5 kV	-2.0 kV	0 V	0 V
Dry	○	○	○	○	○	○	○	△ 0.21	△ 0.20	○
Oil	○	○	○	△ 0.61	× 6.54	× 9.26	× 8.88	× 8.20	× 6.76	△ 0.24
Water	× 1.35	△ 0.62	△ 0.86	△ 0.38	× 5.0	× 1.80	× 2.42	× 1.46	× 6.92	× 5.28

○: damage free; △: less damage; ×: severe damage.

4. Conclusions

The nano- and macrotribological properties of DLC films deposited by the FCVA method were evaluated, and the results are summarized as follows.

- (1) To determine resistance to plastic deformation, H , the modulus of dissipation, and E/H were measured using a nanoindentation test. Strong correlations between hardness, modulus of dissipation, and E/H were observed. The FCVA-DLC films deposited with DC bias voltage showed high resistance to plastic deformation. The DLC films deposited with a DC bias voltage of -50 V exhibited the greatest hardness (approximately 50 GPa), a low modulus of dissipation, and low E/H .
- (2) Nanowear properties of FCVA-DLC films at less than 4 nm depth were evaluated by the AFM. The wear depths of DLC films deposited with floating and DC bias voltage were shallow at less than 1.0 nm. A strong negative correlation was found between H and wear depth.
- (3) A positive correlation was observed between H and the Raman peak ratio I_d/I_g , whereas a negative correlation was observed between wear depth and I_d/I_g . These results show that nanotribological properties such as H and nanowear resistance are highly correlated with I_d/I_g and highly dependent on the films' nanostructures.
- (4) Under dry conditions, DLC films deposited with floating and pulse bias voltages of -1.0 kV exhibited low friction coefficients ($\mu = 0.2$). Under boundary lubrication with MoDTC-containing Z-20, FCVA-DLC films deposited with DC bias voltage also showed low friction coefficients ($\mu = 0.1$). Under water boundary lubrication, the average friction coefficients of DLC films deposited with DC bias voltage also were low at about 0.1.
- (5) Under dry conditions, no visible damage could be observed on any of the FCVA-DLC films after friction testing. The damage to DLC films deposited with DC bias voltage was also very little under boundary lubrication with either MoDTC-containing Z-20 lubricant or water. By contrast, the FCVA-DLC films deposited

with pulse bias voltage and ground clearly exhibited visible damage.

- (6) The friction coefficient determined by a ball-on-disk test was correlated with H under dry conditions. However, with boundary lubrication, the friction coefficient and the specific wear rate showed little correlation with H . These results suggest that the friction and wear behaviors of these films are influenced by other factors such as the adhesion strength between the film and substrate.

Conflict of Interests

The authors declare that there is no conflict of interests regarding the publication of this paper.

Acknowledgment

This research was partly supported by the Storage Research Consortium (SRC).

References

- [1] S. Miyake and R. Kaneko, "Microtribological properties and potential applications of hard, lubricating coatings," *Thin Solid Films*, vol. 212, no. 1-2, pp. 256–261, 1992.
- [2] S. Miyake, R. Kaneko, Y. Kikuya, and I. Sugimoto, "Microtribological studies on fluorinated carbon films," *Journal of Tribology*, vol. 113, no. 2, pp. 384–389, 1991.
- [3] S. Miyake, Y. Yasuda, M. Kano, and Y. Mabuchi, "Slidably movable member and method of producing same," Japanese patent 3555844, U.S. patent 6844068, DE patent 10017459C2, 2002.
- [4] Y. Okamoto, Y. Yasuda, and S. Miyake, "Hard carbon film slidably movable member," Japanese patent application nos. 355775 (2005), 260671 (2005), 088270 (2005), 317513 (2004), 317498 (2004), 276825 (2002).
- [5] M. Kano, Y. Yasuda, Y. Okamoto et al., "Ultralow friction of DLC in presence of glycerol mono-oleate (GMO)," *Tribology Letters*, vol. 18, no. 2, pp. 245–251, 2005.
- [6] S. Miyake and M. Wang, "Nanotribology of magnetic disks," in *Encyclopedia of Nanoscience and Nanotechnology*, H. S. Nalwa, Ed., vol. 19, pp. 399–451, American Scientific Publishers, 2011.
- [7] J. Robertson, "Ultrathin carbon coatings for magnetic storage technology," *Thin Solid Films*, vol. 383, no. 1-2, pp. 81–88, 2001.
- [8] T. Yamamoto, H. Hyodo, S. Tsuchitani, and R. Kaneko, "Ultrathin amorphous carbon overcoats by filtered cathodic arc

- deposition," *IEEE Transactions on Magnetics*, vol. 39, no. 5, pp. 2201–2204, 2003.
- [9] H. Hyodo, T. Yamamoto, and T. Toyoguchi, "Properties of tetrahedral amorphous carbon film by filtered cathodic arc deposition for disk overcoat," *IEEE Transactions on Magnetics*, vol. 37, no. 4, pp. 1789–1791, 2001.
- [10] S. Miyake and S. Yamazaki, "Nanoscratch properties of extremely thin diamond-like carbon films," *Wear*, vol. 305, pp. 69–77, 2013.
- [11] S. Miyake, W. Kurosaka, and K. Oshimoto, "Nanometre scale mechanical properties of extremely thin diamond-like carbon films," *Tribology—Materials, Surfaces & Interfaces*, vol. 3, no. 4, pp. 158–164, 2009.
- [12] X. Shi, B. K. Tay, H. S. Tan et al., "Properties of carbon ion deposited tetrahedral amorphous carbon films as a function of ion energy," *Journal of Applied Physics*, vol. 79, no. 9, pp. 7234–7240, 1996.
- [13] A. C. Ferrari, "Determination of bonding in diamond-like carbon by Raman spectroscopy," *Diamond and Related Materials*, vol. 11, no. 3–6, pp. 1053–1061, 2002.
- [14] N. Taniguchi, Ed., *Nanotechnology*, Oxford University Press, Oxford, UK, 1996.
- [15] Z. N. Farhat, Y. Ding, D. O. Northwood, and A. T. Alpas, "Nanoindentation and friction studies on Ti-based nanolaminated films," *Surface and Coatings Technology*, vol. 89, no. 1-2, pp. 24–30, 1997.
- [16] S. Miyake, S. Watanabe, H. Miyazawa, M. Murakawa, R. Kaneko, and T. Miyamoto, "Improved microscratch hardness of ion-plated carbon film by nitrogen inclusion evaluated by atomic force microscope," *Applied Physics Letters*, vol. 65, no. 25, pp. 3206–3208, 1994.

Research Article

Preparation and Tribological Properties of Dual-Coated TiO₂ Nanoparticles as Water-Based Lubricant Additives

Yue Gu, Xiuchen Zhao, Ying Liu, and Yunxia Lv

School of Materials Science and Engineering, Beijing Institute of Technology, Beijing 100081, China

Correspondence should be addressed to Xiuchen Zhao; zhaoxiuchen@bit.edu.cn

Received 19 October 2013; Accepted 12 December 2013; Published 16 January 2014

Academic Editor: Qi Ding

Copyright © 2014 Yue Gu et al. This is an open access article distributed under the Creative Commons Attribution License, which permits unrestricted use, distribution, and reproduction in any medium, provided the original work is properly cited.

Titanium dioxide nanoparticles (TiO₂) were synthesized and then dual-coated with silane coupling agent (KH-570) and OP-10 in sequence in order to be dispersed stably in water as lubricant additives. The tribological properties and the application performance in Q235 steel machining of the nanoparticles as water-based lubricant additives were investigated on an MSR-10D four-ball tribotester and on a bench drilling machine, respectively. Scanning electron microscope (SEM) and atomic force microscope (AFM) were used to analyze the worn surface. The results show that the surface-modified TiO₂ nanoparticles can remarkably improve the load-carrying capacity, the friction reducing, and anti wear abilities of pure water. The wear scar diameter and the coefficient of friction of the water-based lubricating fluids with TiO₂ nanoparticles decreased, and the thick deep furrows on the surface of wear scar also decreased obviously with the increase of TiO₂ concentration. The power consumption in drilling process was lower and the cutting surface was smoother using the water-based lubricating fluids added TiO₂ nanoparticles compared to the fluid without addition. The reason for nanoparticles improving tribological properties of water based lubricating fluid might be the formation of a dynamic deposition film during rubbing process according to analysis of the worn surface.

1. Introduction

Environment protection and energy conservation are becoming very important issues in modern industrial production. The main cause of energy loss in a mechanical system is friction [1]. The conventional choice is use of a mineral oil-based lubricant to reduce wear and friction in mechanical systems [2]. However, due to the inherent toxicity and the nonbiodegradable nature of oil-based lubricants, developing environment-friendly water-based lubricating fluids is meaningful for resource conservation society [3, 4]. Nevertheless, the poor tribological properties of water-based lubricating fluids [5] make it unacceptable for most of tribological applications. In order to adjust the performance and to improve the properties of water based lubricants, high-quality additives are used [6]. Liu et al. synthesized poly(N-isopropylacrylamide) brush as water-soluble additive and found that the additive helped decrease the friction coefficient of the lubricant to 0.03 due to its physical adsorption of the polymer chains [7]. Zhang et al. investigated the friction and wear behaviours of a (Ca, Mg)-sialon/SAE 52100 steel

pair under the lubrication of various polyols in water and found that the friction coefficient was much lower than that of pure water [8]. Duan Biao in his research on colloidal PST as a new additive for water-based lubrication found that it can improve the base fluid's antiwear and extreme pressure performance [9]. Among all of the studies on water-based lubricant additives, nanoparticles arouse our interest because there have been a lot of researches on nanoparticles as additive in traditional oil-based lubricant and the nanoparticles exhibit good antiwear and friction reducing properties [10–18]. Some researchers have found that Fe₂O₃, CeO₂, and diamond nanoparticles as water-based lubricating additives can significantly reduce the friction coefficients and improve anti-wear properties [19–21]. But the studies on nanoparticles as additive in water and, especially, on the application of nanoparticles in water-based machining liquid are still scarce and should be further investigated due to their difficulty of dispersion and stability in water [22, 23].

Among all nanoparticles as lubricant additives, TiO₂ nanoparticle is a promising additive to water-based lubricating fluids because of its excellent comprehensive properties,

such as nontoxicity, white color, low density, and good tribological properties [24–26].

In this paper, titanium dioxide (TiO₂) nanoparticles were synthesized using the homogeneous precipitation method. The surface of TiO₂ nanoparticles was modified by dual coatings with silane coupling agent (KH-570) and OP-10 in sequence in order to improve its dispersion and stability in water. Zeta potential of TiO₂ nanoparticles in water was measured to analyse its dispersion stability. Tribological properties of TiO₂ nanoparticles as lubricant additive in water were investigated using a four-ball tester. And Q235 steel-drilling test on a bench drilling machine was carried out using water-based cutting fluids with TiO₂ nanoparticles in order to explore TiO₂ nanoparticles action on machining application. The antiwear and friction reducing mechanism of the dual-coated TiO₂ nanoparticles as water-based lubricant additive was discussed according to SEM and AFM analysis of the worn surfaces.

2. Experimental Method

2.1. TiO₂ Nanoparticle Synthesis. TiO₂ nanoparticles were synthesized by homogeneous precipitation (urea as precipitant) method in this paper. All chemical reagents were reagent grade without further purification. The typical preparation procedure is as follows: the solutions of titanous sulfate and sodium dodecyl benzene sulfonate (LAS) were prepared and mixed under stirring, and then an aqueous solution of urea (PH = 1.5) was added into the above mixture at 343 K, and the molar composition of urea to TiOSO₄ was 10:1. After completing precipitation, white precipitated powders were cleaned by deionized water, dried in a vacuum drying oven for 3 hours, calcined in a furnace at 650°C for 5 h, and then ground into powders in absolute ethyl alcohol-added KH-570 using a ball-grinding mill. And the KH-570 surface-modified TiO₂ powders were coated again by OP-10 in water at 343 K under ultrasonic vibration and mechanical stirring. The obtained powder was analyzed by transmission electron microscopy (TEM) and X-ray diffraction (XRD). The zeta potential of the dual-coated TiO₂ nanoparticles in the water was examined by a Zetasizer Nano ZS ZEN 3600 particle-size analyzer to determine its surface charge.

2.2. Tribological Test and Surface Analysis. In this study, deionized water was used as pure water. Water-based lubricants with different concentration of 0.1 vt.%, 0.2 vt.%, 0.4 vt.%, 0.8 vt.%, and 1.6 vt.% TiO₂ nanoparticles were prepared.

Experiments of measuring friction reduction and antiwear properties of the cutting fluids with nanoparticles were carried out with an MSR-10D four-ball tribotest at a rotating speed of 1440 rpm under the applied loads of 147 N for 10 min. The steel ball (Φ 12.7 mm, HRC 62–64) was made of GGr15 bearing steel (AISI 52100 steel). Same tests were performed for three times so as to minimize data scattering. At the end of each test, wear scar diameters on the three stationary balls were measured, and an average wear scar diameter of the three tests was calculated. Scanning electron

microscope (SEM), atomic force microscope (AFM), and energy dispersive spectrometry (EDS) were used to examine the morphology and chemical composition of the wear scars and to study possible tribochemical changes involved in the friction process.

2.3. The Application of the Water-Based Cutting Fluids Added TiO₂ Nanoparticle. The application performance of water-based cutting fluids added TiO₂ nanoparticles was explored by drilling test. A bench drilling machine (Z516-A) was used to measure the power consumption of drilling at 1800 rpm and room temperature for evaluating lubricating properties. The power consumption was calculated by the following formula:

$$\frac{\Delta P}{P} = \frac{(P - P_0)}{P_0} * 100\%, \quad (1)$$

where P_0 is the input power when the drilling machine is idle, yet the P is the actual input power during the drilling process.

The applied steel plates in all tests were made of Q235 steel, and the diameter of drill bit was 10 mm. The addition concentration of dual-coated TiO₂ nanoparticles in pure water was 2 vt.%, 4 vt.%, 6 vt.%, and 10 vt.%, respectively considering actual situation of drill processing. The water-based cutting fluids without nanoparticles used in the experiment were pure water mixed with an amount of KH-570 and OP-10 in order to exclude the effect of surfactant on TiO₂ nanoparticles action.

The machining surfaces of inside wall of the holes were analyzed after the experiments.

3. Results and Discussion

3.1. TiO₂ Nanoparticle Characterization. Figure 1 presents the XRD pattern and TEM images of TiO₂ nanoparticles. It can be seen that the prepared particles are pure TiO₂ particles with single anatase phase (Figure 1(a)). The dual-coated TiO₂ nanoparticles have spherical shape, take on homogeneous dispersion, and have no obvious aggregation, and the average size of the prepared particles is about 20 nm in diameter as shown in Figure 1(b). The surface modification agents are adsorbed on the surface of nanocrystalline, which can reduce the surface energy of nanocrystalline and prevent nanoparticles from aggregating. The zeta potential value of pure TiO₂ nanoparticles in water is measured to be −5.44 mV, and the zeta potential value of dual-coated nano-TiO₂ increases to −24.6 mV. The modified nanoparticles in water show relatively higher dispersion stability because the zeta potential value of dual-coated nano-TiO₂ is more than three times higher than that of pure TiO₂ nanoparticles.

3.2. Experimental Results of Four-Ball Test. Maximum non-seizure load (P_B values) of the lubricants containing the dual-coated TiO₂ nanoparticles is shown in Figure 2. In general, the P_B value of the lubricant increases with the increase of nanoparticles addition concentration, but the concentration of nanoparticles is 0.4 vt.%, and the P_B value reaches the

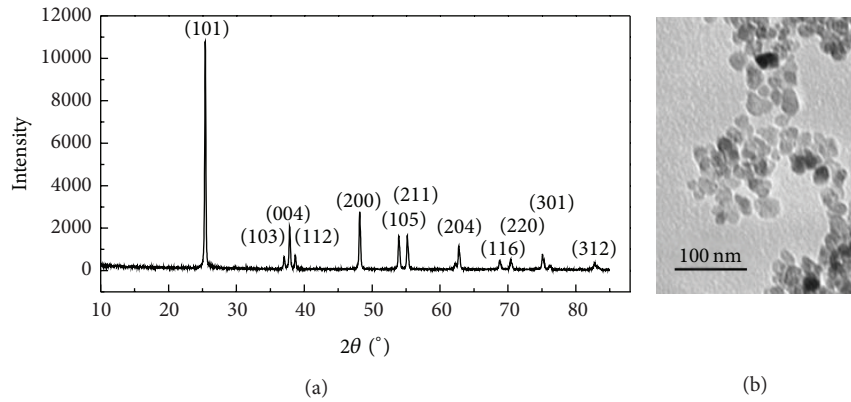


FIGURE 1: (a) X-ray diffraction spectra of the TiO₂ nanoparticles; (b) TEM image of the TiO₂ nanoparticles.

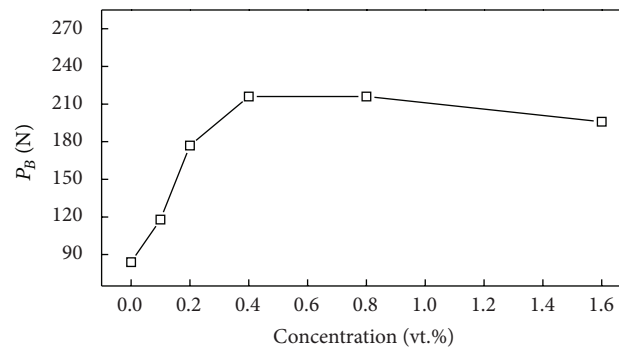


FIGURE 2: The maximum nonseizure load (P_B values) of lubricants with different additive concentration.

maximal value. At that concentration, the P_B value of the lubricants with TiO₂ nanoparticles is improved maximally by 157%. So it can be thought that the dual-coated TiO₂ nanoparticle has good load-carrying capacity and excellent extreme pressure property.

The wear scar diameter and friction coefficient are functions of the additive nanoparticle concentration in water, as presented in Figure 3. Figure 3(a) shows wear scar diameter (WSD) of steel balls lubricated by base water containing different amounts of TiO₂ nanoparticles. Results show that TiO₂ nanoparticles can improve the antiwear properties (reduce WSD) of the base water obviously, even at a low concentration of 0.1 vt.%. When the concentration of nanoparticles in water increases, the value of WSD decreased. The WSD of the lubricants with TiO₂ nanoparticles is reduced by 34.8% maximally.

The coefficient of friction is a demonstration of energy loss caused by friction. Figure 3(b) shows the friction reducing property of the TiO₂ nanoparticles at different additive concentration in base water. It can be seen from Figure 3(b) that the friction coefficient of the water-added TiO₂ nanoparticles is decreased dramatically compared to the lubricant without nanoparticles with the friction coefficient of 0.17; the minimum value of friction coefficient of the water containing

nanoparticles reaches 0.04 as the addition concentration of nanoparticles in water is 1.6 vt.%, which indicates that dual-coated TiO₂ nanoparticles as water-based lubricant additive have excellent friction reducing property.

Figure 4 gives SEM images of the rubbed surface lubricated with pure water and water-added TiO₂ nanoparticles of 0.1 vt.%, 0.8 vt.%, and 1.6 vt.%, respectively. The worn surface lubricated with pure water presented in Figure 4(a) is rough with many thick and deep furrows due to strong adhesion and ploughing between contacted asperities on the rubbed surface of tribopairs. The worn surface lubricated with water-added TiO₂ nanoparticles is smoother than that lubricated with pure water. And with the increase of addition concentration of TiO₂ nanoparticles in pure water, the thick and deep furrows on wear scar surfaces become less and shallower.

3.3. Experimental Results of Drilling Test. Figure 5 plots the variation of power consumption of drilling with addition concentration of TiO₂ nanoparticles in cutting fluids. In this figure, it can be seen that with the increase of TiO₂ nanoparticles in cutting fluids, the power consumption of drilling firstly decreases to the minimum value and then increases. The optimal addition concentration is 6 vt.%, and

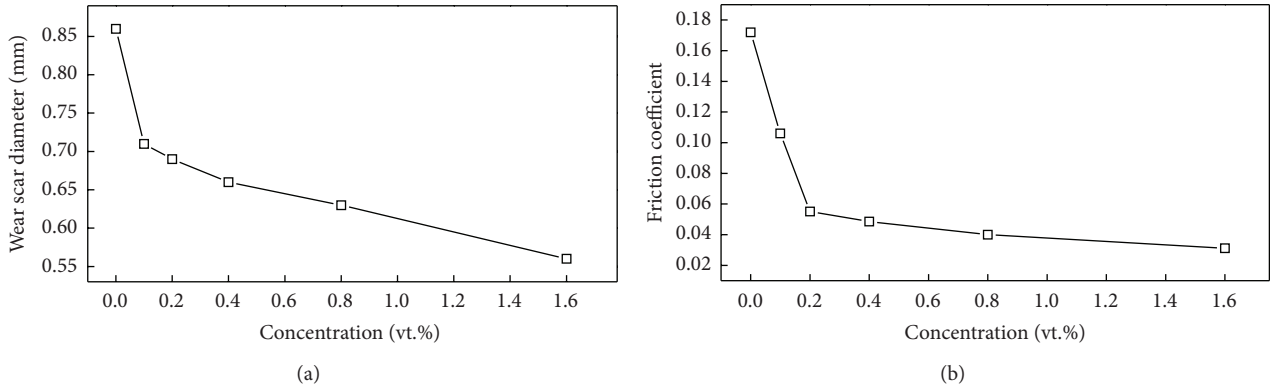


FIGURE 3: Wear scar diameter (a) and friction coefficient (b) as a function of additive concentration.

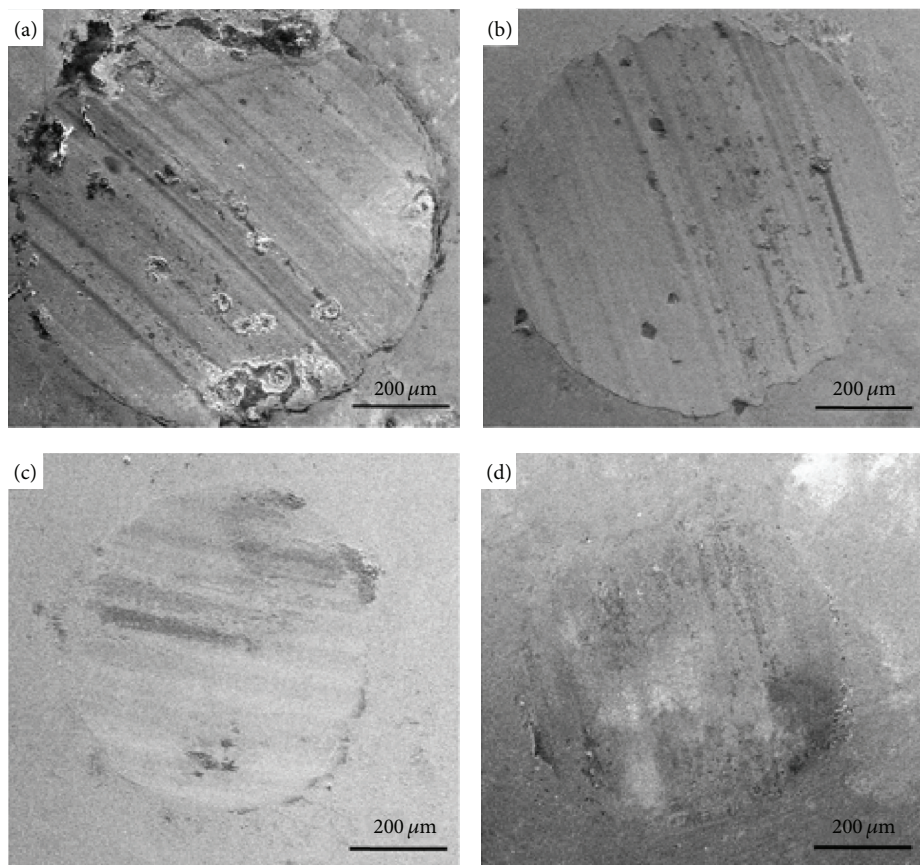


FIGURE 4: SEM micrographs of wear scar surfaces lubricated with different concentration of nanoparticles: (a) no addition, (b) 0.1 wt.%, (c) 0.8 wt.%, and (d) 1.6 wt.%.

under this concentration, the power consumption of drilling is 35.4% less than that without TiO_2 addition.

Figure 6 presents SEM images of the machined inside surface of drilling hole lubricated without lubricant liquid, using cutting fluids without nanoparticles and using cutting fluids with 2 wt.% and 6 wt.% nanoparticles.

The machined inside surface lubricated without lubricant liquid presented in Figure 6(a) is evidently rough with many built-up edges and some thick deep furrows

because of severe adhesion and ploughing. In Figure 6(b) the machined inside surface lubricated with cutting fluids without nanoparticles is also rough with many thick and deep furrows but without built-up edge. In Figures 6(c), and 6(d), the machined inside surfaces lubricated with cutting fluids with 2 wt.% and 6 wt.% nanoparticles, respectively, are smoother than that lubricated with the cutting fluids without nanoparticles, and the furrows of surface are less and shallower.

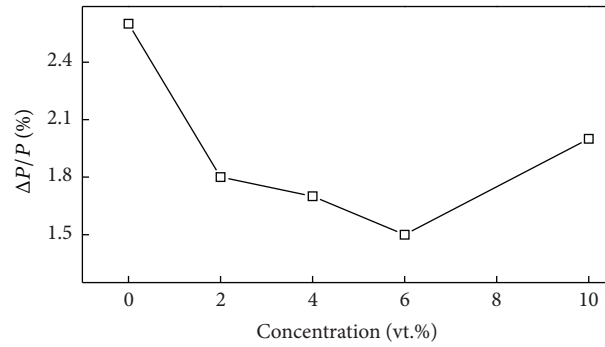


FIGURE 5: The power consumption of drilling as a function of additive concentration.

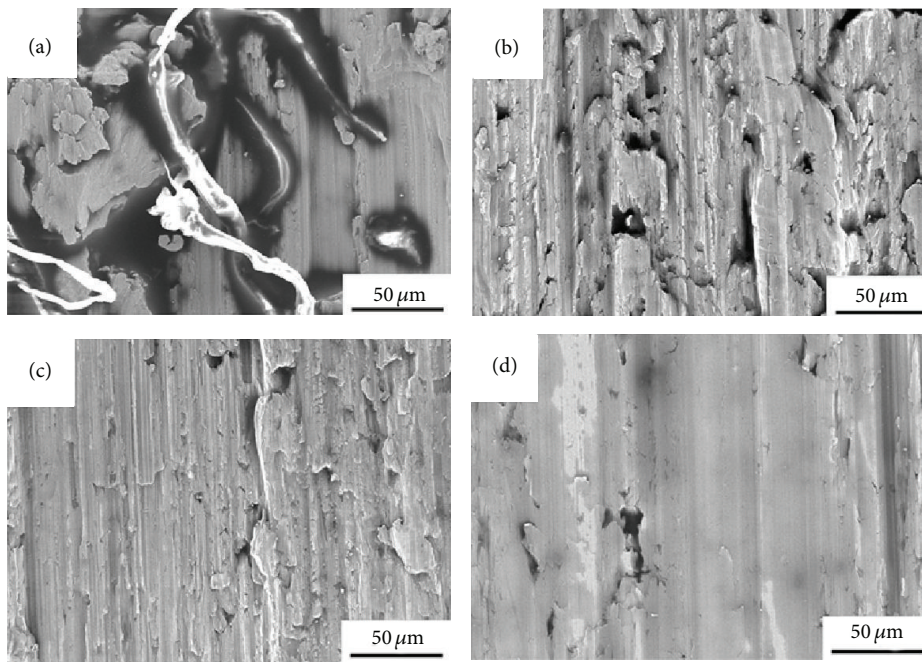


FIGURE 6: SEM image of the machined inside surface of drilling hole lubricated (a) without lubricant liquid; (b) using cutting fluids without nanoparticles; (c) using cutting fluids with 2 vt.% nanoparticles; (d) using cutting fluids with 6 vt.% nanoparticles.

3.4. Tribological Mechanism Analysis of Nanoparticles as Water-Based Additive. Figure 7 presents the tribological model of nanoparticles as water-based lubricant additive according to the above experimental results.

The antiwear and friction reducing mechanism of nanoparticles as water-based additive might be understood better due to the separation effect of nanoparticles as deposition film to the asperities on the contacting surface of the tribo-pairs. When lubricated with the water without nanoparticles addition as shown in Figure 7(a), many asperities on the rubbing surface of tribo-pairs might directly be in contact due to poor separation of pure water to the asperities, which leads to strong adhesion and ploughing between contacted asperities on the rubbed surface of tribo-pairs [27], and many thick and deep furrows on the worn surface are found as shown in Figures 4(a) and 6(b). When a trace amount of nanoparticles were added into the water as lubricant additive

as shown in Figure 7(b), the nanoparticles might be deposited on the rubbing surface, which separates apart asperities on the contacting surface and reduces the thick deep furrows on the worn surface as shown in Figures 4(b) and 6(c), due to reduction of the area of contacted asperities on the rubbing surfaces. When lubricated with the water added with an appropriate amount of nanoparticles as shown in Figure 7(c), the nanoparticles separate all asperities on the contacting surface and the thick deep furrows on the worn surface cannot be found as shown in Figures 4(c), 4(d), and 6(d). At the same time, the worn surface became smoother compared to that lubricated without nanoparticles.

In order to further explore the nanoparticles action as water-based lubricant additive in rubbing process, atom force microscope (AFM) is used to analyze the worn surface of steel ball lubricated with the water-added 1.6 vt.% nanoparticles after ultrasonic washing for 5 minutes as shown in Figure 8.

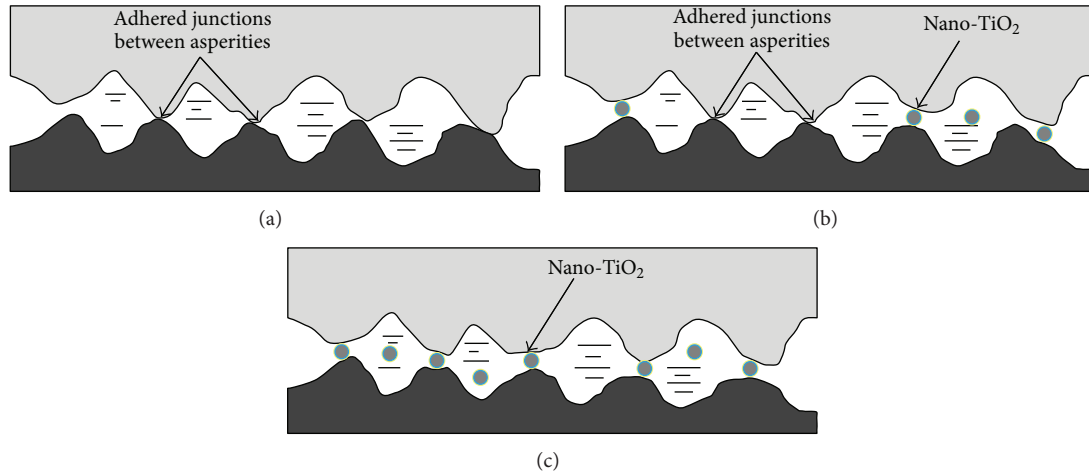


FIGURE 7: Schematic diagram showing separation effect of nanoparticles during rubbing lubricated (a) pure water without nanoparticle; (b) the water with a trace amount of nanoparticles; (c) the water with an appropriate amount of nanoparticles.

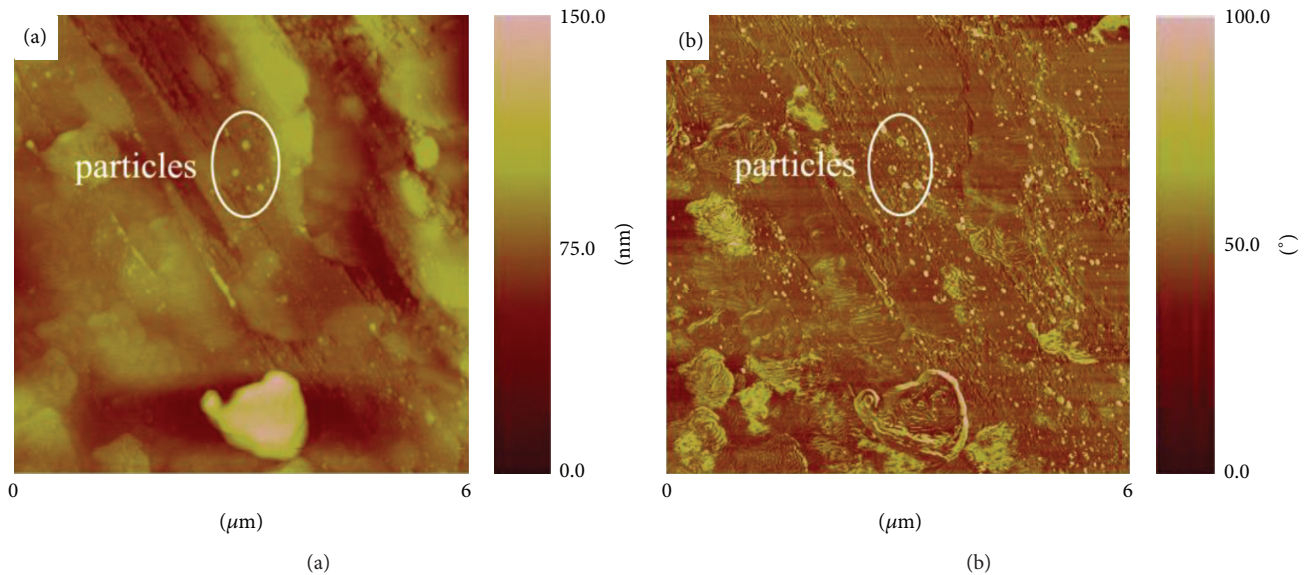


FIGURE 8: AFM analysis of the worn surface of steel ball after four-ball test lubricated by the water with 1.6 vt.% TiO_2 nanoparticles with ultrasonic washing for 5 minutes (a) height image; (b) phase image.

The nanoparticles are found on the surface of asperities. However, the amount of nanoparticles found on the surface of asperities is little and cannot separate the contacted asperities completely, so cannot perform excellent tribological properties.

Figure 9 presents the EDS analysis of worn surface after four-ball test lubricated by the water-added 1.6 vt.% TiO_2 nanoparticles without ultrasonic washing and with ultrasonic washing for 2 minutes and 5 minutes, respectively. It can be seen that with the increase of washing time, weight percent of Ti element on the worn surface decreases gradually, and Ti element is not found on the worn surface after ultrasonic washing for 5 minutes.

The reasonable explanation might be a dynamic deposition film formed by nanoparticles during rubbing process

which might separate effectively the direct contact of asperities, alleviate the strong adhesion and ploughing between asperities, and result in the decrease of the wear scar diameter and the friction coefficient obviously during four-ball test as shown in Figure 3 and the significant reduction of the power consumption during drilling test as shown in Figure 5.

4. Conclusion

- (1) Dual-coated TiO_2 nanoparticles with KH-570 and OP-10 in sequence exhibit good dispersity and stability in pure water.
- (2) Dual-coated TiO_2 nanoparticles as water-based lubricant additive provide more excellent tribological

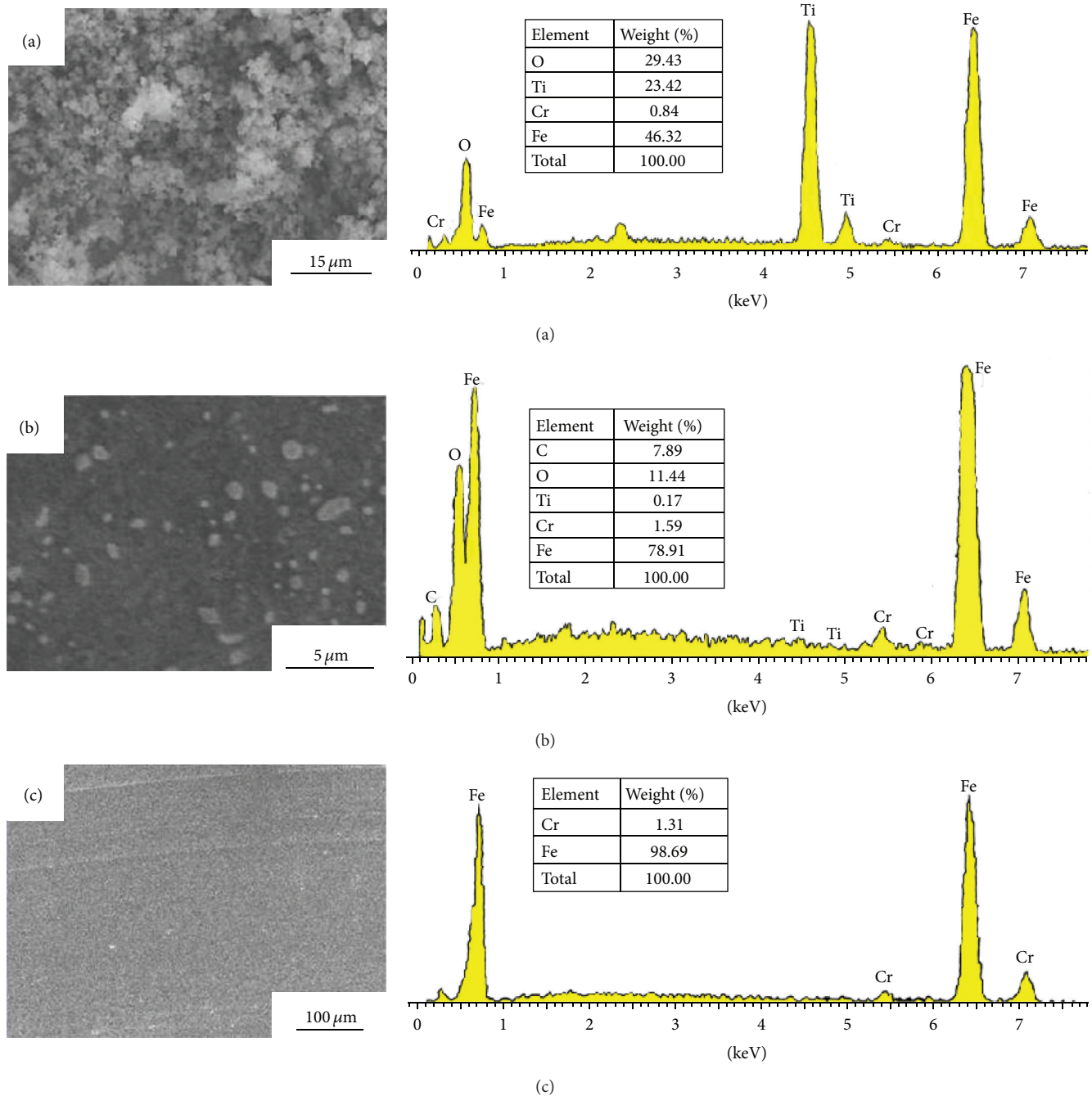


FIGURE 9: SEM and EDS analysis of worn surface of steel ball after four-ball test lubricated by the water-added 1.6 wt.% TiO_2 nanoparticles. (a) Without ultrasonic washing; (b) with ultrasonic washing for 2 minutes; (c) with ultrasonic washing for 5 minutes.

properties than pure water in terms of load-carrying capacity, antiwear, and friction reducing.

- (3) Dual-coated TiO_2 nanoparticles as cutting fluids additives also exhibit better friction reducing property. The power consumption in drilling process lubricated with TiO_2 nanoparticles is lower than that of the fluid without nanoparticle addition. The optimal concentration is about 6 wt.%.
- (4) The antiwear and friction reducing mechanism is that TiO_2 nanoparticles can form a dynamic deposition

film on the worn surface and separates the direct contact between the asperities of the rubbing surfaces according to the analysis of SEM, AFM, and EDS of worn surfaces.

Conflict of Interests

The authors declare that there is no conflict of interests regarding the publication of this paper.

Acknowledgment

The authors appreciate the financial support of the National Key Technology R&D Program (no.2006BAF02A11).

References

- [1] H. Yoshizawa, Y.-L. Chen, and J. Israelachvili, "Fundamental mechanisms of interfacial friction. 1: relation between adhesion and friction," *Journal of Physical Chemistry*, vol. 97, no. 16, pp. 4128–4140, 1993.
- [2] A. Willing, "Lubricants based on renewable resources: an environmentally compatible alternative to mineral oil products," *Chemosphere*, vol. 43, no. 1, pp. 89–98, 2001.
- [3] P. Mercurio, K. A. Burns, and A. Negri, "Testing the ecotoxicology of vegetable versus mineral based lubricating oils. 1: degradation rates using tropical marine microbes," *Environmental Pollution*, vol. 129, no. 2, pp. 165–173, 2004.
- [4] W. J. Bartz, "Lubricants and the environment," *Tribology International*, vol. 31, no. 1–3, pp. 35–47, 1998.
- [5] H. Lei, W. Guan, and J. Luo, "Tribological behavior of fullerene-styrene sulfonic acid copolymer as water-based lubricant additive," *Wear*, vol. 252, no. 3–4, pp. 345–350, 2002.
- [6] A. Tomala, A. Karpinska, W. S. M. Werner, A. Olver, and H. Störi, "Tribological properties of additives for water-based lubricants," *Wear*, vol. 269, no. 11–12, pp. 804–810, 2010.
- [7] Y. H. Liu, X. YuQi, and L. JianBin, "Preparation of poly (N-isopropylacrylamide) brush bonded on silicon substrate and its water-based lubricating property," *Science China Technological Sciences*, vol. 55, no. 12, pp. 3352–3358, 2012.
- [8] W. Zhang, W. Liu, and L. Yu, "Friction and wear behaviors of a (Ca, Mg)-sialon/SAE 52100 steel pair under the lubrication of various polyols as water-based lubricating additives," *Tribology International*, vol. 33, no. 11, pp. 769–775, 2000.
- [9] B. Duan, "A study on colloidal PST: a new type of water-based lubrication additive," *Wear*, vol. 236, no. 1–2, pp. 235–239, 1999.
- [10] L. Rapoport, N. Fleischer, and R. Tenne, "Applications of WS₂ (MoS₂) inorganic nanotubes and fullerene-like nanoparticles for solid lubrication and for structural nanocomposites," *Journal of Materials Chemistry*, vol. 15, no. 18, pp. 1782–1788, 2005.
- [11] Y. Y. Wu, W. C. Tsui, and T. C. Liu, "Experimental analysis of tribological properties of lubricating oils with nanoparticle additives," *Wear*, vol. 262, no. 7–8, pp. 819–825, 2007.
- [12] A. Hernández Battez, R. González, J. L. Viesca et al., "CuO, ZrO₂ and ZnO nanoparticles as antiwear additive in oil lubricants," *Wear*, vol. 265, no. 3–4, pp. 422–428, 2008.
- [13] J. Song, J. Zhang, and C. Lin, "Influence of graphene oxide on the tribological and electrical properties of PMMA composites," *Journal of Nanomaterials*, vol. 2013, Article ID 846102, 2013.
- [14] V. Eswaraiah, V. Sankaranarayanan, and S. Ramaprabhu, "Graphene-based engine oil nanofluids for tribological applications," *ACS Applied Materials and Interfaces*, vol. 3, no. 11, pp. 4221–4227, 2011.
- [15] V. N. Bakunin, A. Y. Suslov, G. N. Kuzmina, and O. P. Parenago, "Synthesis and application of inorganic nanoparticles as lubricant components—a review," *Journal of Nanoparticle Research*, vol. 6, no. 2–3, pp. 273–284, 2004.
- [16] J. Zhou, Z. Wu, Z. Zhang, W. Liu, and Q. Xue, "Tribological behavior and lubricating mechanism of Cu nanoparticles in oil," *Tribology Letters*, vol. 8, no. 4, pp. 213–218, 2000.
- [17] X. Li, Z. Cao, Z. Zhang, and H. Dang, "Surface-modification in situ of nano-SiO₂ and its structure and tribological properties," *Applied Surface Science*, vol. 252, no. 22, pp. 7856–7861, 2006.
- [18] C. Gu, Q. Li, Z. Gu, and G. Zhu, "Study on application of CeO₂ and CaCO₃ nanoparticles in lubricating oils," *Journal of Rare Earths*, vol. 26, no. 2, pp. 163–167, 2008.
- [19] C. Zhao, Y. K. Chena, and G. Ren, "A study of tribological properties of water-based ceria nanofluids," *Tribology Transactions*, vol. 56, no. 2, pp. 275–283, 2013.
- [20] T. X. Phuoc and M. Massoudi, "Experimental observations of the effects of shear rates and particle concentration on the viscosity of Fe₂O₃-deionized water nanofluids," *International Journal of Thermal Sciences*, vol. 48, no. 7, pp. 1294–1301, 2009.
- [21] Y. Liu, X. Wang, G. Pan, and J. Luo, "A comparative study between graphene oxide and diamond nanoparticles as water-based lubricating additives," *Science China Technological Sciences*, vol. 56, no. 1, pp. 152–157, 2013.
- [22] P. Fernández-Ibáñez, J. Blanco, S. Malato, and F. J. De Las Nieves, "Application of the colloidal stability of TiO₂ particles for recovery and reuse in solar photocatalysis," *Water Research*, vol. 37, no. 13, pp. 3180–3188, 2003.
- [23] M. Kosmulski, "pH-dependent surface charging and points of zero charge. III. Update," *Journal of Colloid and Interface Science*, vol. 298, no. 2, pp. 730–741, 2006.
- [24] Q. Xue, W. Liu, and Z. Zhang, "Friction and wear properties of a surface-modified TiO₂ nanoparticle as an additive in liquid paraffin," *Wear*, vol. 213, no. 1–2, pp. 29–32, 1997.
- [25] W. Ye, T. Cheng, Q. Ye, X. Guo, Z. Zhang, and H. Dang, "Preparation and tribological properties of tetrafluorobenzoic acid-modified TiO₂ nanoparticles as lubricant additives," *Materials Science and Engineering A*, vol. 359, no. 1–2, pp. 82–85, 2003.
- [26] J. Qian, X. Yin, N. Wang, L. Liu, and J. Xing, "Preparation and tribological properties of stearic acid-modified hierarchical anatase TiO₂ microcrystals," *Applied Surface Science*, vol. 258, no. 7, pp. 2778–2782, 2012.
- [27] Y. Mo, K. T. Turner, and I. Szlufarska, "Friction laws at the nanoscale," *Nature*, vol. 457, no. 7233, pp. 1116–1119, 2009.

Research Article

Hard and Soft Multilayered SiCN Nanocoatings with High Hardness and Toughness

S. K. Mishra,¹ Devraj Verma,¹ S. Bysakh,² and L. C. Pathak¹

¹ CSIR-National Metallurgical Laboratory, Jamshedpur 831007, India

² CSIR-Central Glass and Ceramic Research Institute, Kolkata 700032, India

Correspondence should be addressed to S. K. Mishra; skm_smp@yahoo.co.in

Received 16 September 2013; Revised 6 December 2013; Accepted 9 December 2013

Academic Editor: Qi Ding

Copyright © 2013 S. K. Mishra et al. This is an open access article distributed under the Creative Commons Attribution License, which permits unrestricted use, distribution, and reproduction in any medium, provided the original work is properly cited.

Alternate hard and soft layers increase deformation accommodation as thin hard layers slide relative to each other due to shear deformation of low modulus layers. However, the processing of such multilayers is challenging. In the present paper the alternating soft and hard multilayered SiCN coating deposited by magnetron sputtering has been studied and presented. A hardness and modulus of 37 GPa and 317 GPa with elastic recovery of 62% are achieved by alternate hard and soft layer of Si-C-N by magnetron sputtering. The trilayer films sustained even 2000 gf under indentation without failure though substrate plastically deformed. The fracture toughness value K_{IC} was measured to be 9.5–10 MPa m^{1/2}, significantly higher than many reported hard coatings.

1. Introduction

For engineering applications, hardness must be complimented with high toughness, which is a property of equal importance as hardness. Toughness is an important mechanical property related to materials resistance against the formation of cracks resulting from stress accumulation in the vicinity of the structural imperfections. In an energetic context, toughness is the ability of the material to absorb energy during deformation until fracture. Therefore, a high toughness coating has high resistance to the formation of cracks under stress and high energy absorbance to hinder crack propagation, whereby preventing chipping, flaking, or catastrophic failure. When the applied stress exceeds the critical value for a particular crack size, there is a growth in the microcracks present which results in brittle failure of the materials as per Griffith's theory [1]. Hard coatings are very important for different industrial application for protection against wear. However hardness must be complimented with good toughness for prolonged performances of these coatings. The nanocrystalline-amorphous composite coatings result in improvement in strength, due to restriction in the dislocation movement for crystallites of very small dimensions which gets pinned when it is surrounded by amorphous matrix.

The amorphous matrix present in the surrounding also helps in reducing problems associated with lattice misfit as the dislocation which might be in the crystalline cannot propagate in to the amorphous phase and vice versa. Secondly, if both the nanocrystalline phase and the amorphous phase are strong, then they have higher cohesive energies [2–4]. The usual mechanism of deformation and mechanical failure is absent or hindered as no dislocation multiplication source can operate and the energy of dislocation in such small crystallites being too high is repelled towards the grain boundaries and annihilates there during growth. However, the crack growth is hindered in nanocrystalline composites and the sizes of the cracks are limited to 2–4 nm. Therefore, nanocomposites coatings also provide high toughness and low friction apart from hardness at the same time [5].

Si-C-N nanocomposites due to their exceptional combination of properties are very promising material for applications as wear and oxidation resistance, optoelectronic material in hostile environment. Si-C-N coatings are desired for many industrial applications such as turbine engines, blades, and wear resistant coatings for automotive industry to enhance the life as well as the performances of the components. They also find application in MEMS device fabrication in the form of field emission displays.

TABLE I: Deposition parameters for the single-layer and multilayer Si-C-N films deposited by DC magnetron sputtering.

Type of coating	Nature of coating	Nitrogen pressure (mbar)	Argon pressure (mbar)	Deposition pressure (mbar)
Single-layer SiCN coating (A)	Hard	0.001	0.009	0.01-0.02
Single-layer SiCN coating (B)	Soft	0.099	0.001	0.09-0.1
Double-layer SiCN coating (C) (AB)	Hard	0.001	0.009	0.01
	Soft	0.099	0.001	0.09-0.1
Double-layer SiCN coating (D) (BA)	Soft	0.099	0.001	0.09-0.1
	Hard	0.001	0.009	0.01-0.02
Trilayer SiCN (E) (ABA)	Hard	0.001	0.009	0.01
	Soft	0.099	0.001	0.09-0.1
	Hard	0.001	0.009	0.01

Thin film depositions of Si-C-N have been carried out by plasma and ion-assisted deposition, chemical vapour deposition, magnetron sputtering, microwave, and electron cyclotron resonance plasma enhanced chemical vapour (ECRPECVD), ion implantation, pulsed laser deposition, and rapid thermal chemical vapour deposition (RTCVD). At substrate temperatures below 1000°C, amorphous Si-C-N films are reported to be deposited, while higher temperatures produced crystalline composite films of α - and β -Si₃N₄ and α - and β -SiC. Many reports are available on single-layer hard coatings of SiCN nanocomposite coatings and hardness and modulus has been tailored by varying the plasma or process parameter during deposition and films with less hardness to high harness more than 40 GPa has been achieved.

The limitations associated with monolithic coatings such as lack of multifunctional character and high residual stresses and problems associated with adhesion to substrate have led to increasing use of multilayer coatings. Multilayer coatings not only offer the combination of attractive properties from different materials, but also have observably increased tribological performance over monolithic coatings. The multilayers have advantage that use of one interlayer or several interlayers enhances the adhesion of coatings by reducing the mismatch in mechanical, chemical, or thermal properties between coatings and substrate. Alternating layers can improve the fracture toughness either by introducing layer interfaces to stop cracks or providing a tough medium through which propagation of cracks is prohibited.

A review paper by Stueber et al. [6] presents recent developments in hard, wear resistant thin films based on multilayer coating concept. There are many factors that contribute to enhanced hardness in multilayers.

Multilayers with alternating soft and hard layers increase deformation accommodation as thin hard layers slide relative to each other by virtue of the shear deformation of low modulus layers. However the processing aspect of multilayers is much more demanding with respect to the process control and material selection, number of layers required ensuring sufficient interface quality, stability, and avoiding interfacial reactions between layers that can decrease interfacial strength.

Lot of research is being done on the multilayer coatings alternated with two materials forming the bilayer period [7-9]. The two dissimilar material layers however face the problem of interface stresses, thermal mismatch, and lattice

mismatch of the two different materials. There is very little evidence in the literature on the deposition of multilayer coatings formed by depositing the hard and soft coating of the same material. Research has been done on the effect of pressure and nitrogen on the hardness of the Si-C-N coatings [10-17]. The research on different aspect of single-layer hard SiCN coatings has also been reported by one of the authors Mishra et al. in the literature, where it showed very fine nanocrystalline dispersion of size 2-10 nm in SiCN amorphous matrix [18, 19]. The films were very hard ranging between 10 and 35 GPa dependent on the deposition parameters.

Deposition pressure and nitrogen to argon ratio can play a dominant role in making a hard film (hardness greater than 20 GPa) or a soft film (hardness lesser than 20 GPa). The deposition of alternate hard and soft layers of the same Si-C-N material will circumvent the problems of interface stresses, thermal mismatch, and lattice mismatch of the two different materials soft and hard layers.

In the present paper our research on the microstructural study on the interface of the alternate hard and soft layers of Si-C-N and mechanical and fracture behaviour of hard and tough SiCN multilayered structure deposited by magnetron sputtering is discussed.

2. Experimental

Single-layer and multilayer Si-C-N hard and soft coatings were deposited by reactive DC magnetron sputtering on silicon (Si-100) and stainless steel (SS-304) substrates, using single compact target of SiC in argon-nitrogen atmosphere of plasma. The deposition pressure and nitrogen to argon ratio are varied to generate the comparatively soft (hardness less than 20 GPa) and hard (hardness more than 30 GPa) coatings of the same material, that is, Si-C-N and then use them to generate multilayer coating alternated hard and soft coatings. All coatings were deposited at 365°C substrate temperatures and at 150 watt power. Each layer was deposited for 2-hour duration. The deposition parameters are given in Table I.

Microstructural studies were carried out using AFM (SEIKO 400 Japan) and TEM (FEI Tecnai G230ST, The Netherlands). Nanoindentation (XP, MTS/Agilent, USA) experiments were done at varying depths of the film with strain rate of 0.05 s⁻¹. Poisson's ratio was taken as 0.25 for calculations of all parameters. A harmonic displacement of 2 nm at a frequency of 45 Hz was initialized for the experiments.

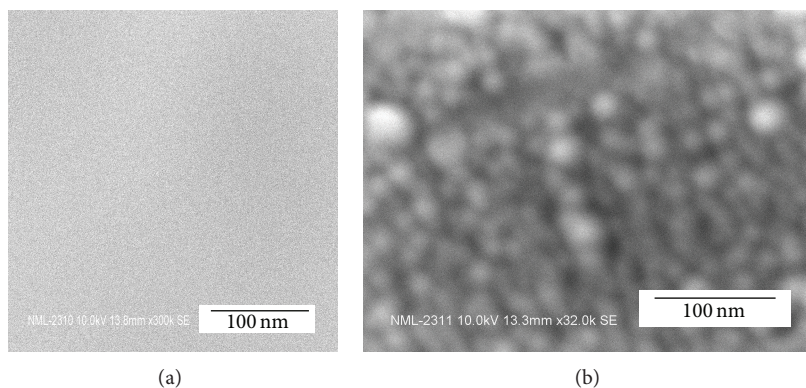


FIGURE 1: SEM image of SiCN film on SS: (a) single-layer A, hard film and (b) single-layer soft film, B.

The depth for each indentation was fixed as 500 nm and the experiment was carried out in continuous stiffness mode. The average hardness and modulus for each indent were averaged between the depth of 50 nm to 500 nm and the values reported are the average of 8 indents. The TEM samples for interface study were prepared by cutting very thin sample from cross section, then lapped, and finally ion beam thinned for TEM transparency. The percentage elastic recovery of the films was calculated from load-depth curve obtained by nanoindentation and by measuring total area under maximum loading and the retained plastic area with formula given below

$$\text{Percentage Elastic Recovery} = \left\{ \frac{(\text{Total area under the curve} - \text{Plastic area})}{\text{Total area}} \right\} * 100. \quad (1)$$

The microhardness was measured by Leica Germany at 25 gf load. The effect of higher loads was studied by indenting at higher loads of 100 gf, 200 gf, 300 gf, 500 gf, 1000 gf, and 2000 gf on the film. For each film the value presented is average of 6 indents.

3. Results and Discussion

The thicknesses of the single-layer hard (A) coating deposited for 2 hrs was about 2.5 micrometer, whereas soft film (B) when deposited for 2 hrs was 1.7 micrometer. Later all the layered films soft or hard were deposited in the desired sequence for 2 hrs each. The sequences were AB, BA, and ABA.

SEM images of the Si–C–N films deposited at different pressures (films A and B) are given in Figure 1. It was observed that the films deposited at the pressure of 10 Pa had larger particle sizes (100–200 nm) but in the film deposited at 1 Pa no particles could be resolved by SEM so they were very fine. The microstructure for the film deposited at 1 Pa showed densely packed which may be responsible for its high hardness value (around 32 GPa) whereas the microstructure for films deposited at 10 Pa showed the presence of globular structures with variable dimensions which may be the reason for their

comparatively low hardness values (around 9.6 GPa). The introduction of nitrogen in larger ratio (nitrogen argon ratio around 99:1) and increase in deposition pressure (around 10 Pa) for film B is responsible for the significant particle growth, due to lower deposition rates giving enough time to the atoms in terms of mobility and diffusion. The double-layer Film C (AB) the top layer is soft film B had larger size particles (1 μm) as seen in SEM image for bilayer.

SFM studies of different single and multilayer sequence were also carried out. The hard film was having very fine particle size in the film in the range of less than 50 nm, whereas the soft film B showed 100–120 nm particle size Figure 2(b). The film C (AB, hard-soft) showed its particle size around 50 nm. The double-layer film D soft hard (BA) showed 50–70 nm growth on surface. The trilayer film ABA had larger growth on top it was found to be around 300 nm. The films were dense as is revealed by AFM. Figures 2(a) and 2(b) presents the AFM images of double-layer film C (AB) and trilayer film E (ABE).

4. Interface Study of the Trilayer (ABA) SiCN Film

The interface cross sectional studies of trilayer film C which was consisting of hard-soft-hard three layers on silicon substrate was studied by Transmission electron microscope. Figure 3(a) shows the interface of Si substrate and the first hard layer. It was observed that they had sharp interface and the individual first hard layer A in the trilayer film was amorphous as confirmed by the SAED of film (inset of Figure 3(a)). The EDX of the film showed mainly the presence of Si, N, and C. Though the interface between the hard and soft layers was sharp, a very thin 5 nm reacted zone was observed at the interface between SiCN layer A and the substrate as can be seen in Figure 3(b).

The interface of the layer A, hard film, and the layer B, soft film, is shown in Figure 4(a). Here the interface was sharp and no delamination was observed. A nanocolumnar type growth morphology was observed in the soft film with larger particle sizes compared to hard film A. This was complimentary with the surface microstructure revealed by AFM and SEM. EDS composition analysis of the soft film also showed the presence

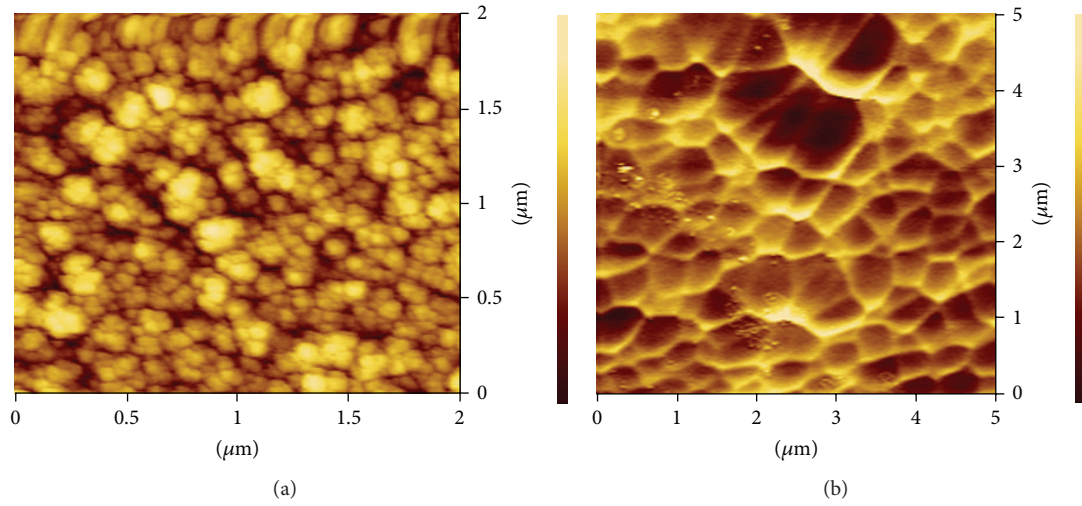


FIGURE 2: AFM topography image of multilayer layer SiCN film on Si: (a) film C (layer AB) and (b) triple layer SiCN film E (ABA).

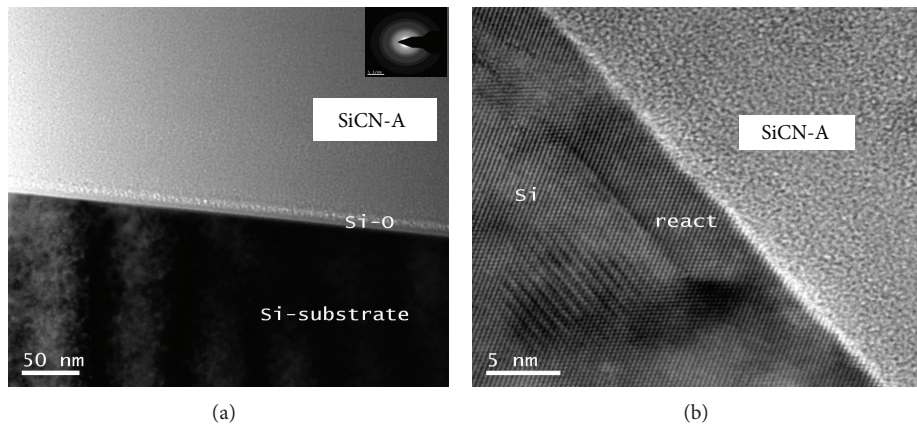


FIGURE 3: Cross-sectional TEM microstructure: (a) Si and hard SiCN-A interface, SAED of SiCN hard layer A, and (b) high-resolution image of the interface and the reacted zone.

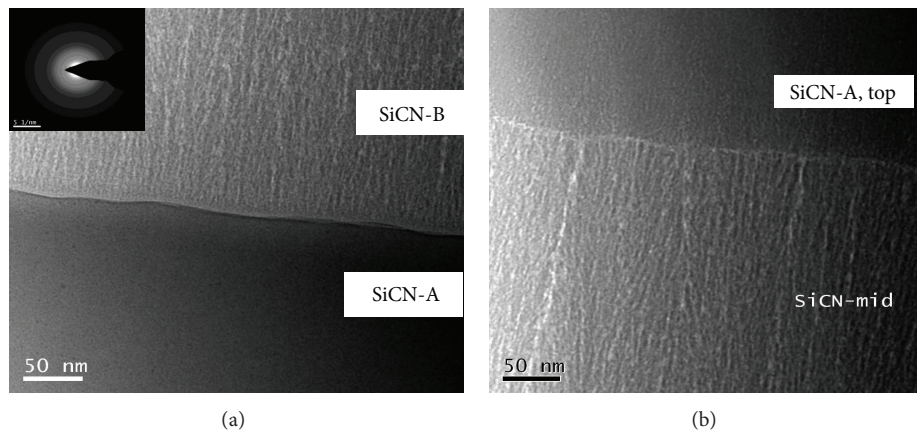


FIGURE 4: Cross-sectional TEM microstructure of SiCN layered film: (a) AB layer interface and SAED from Layer B and (b) B middle soft A top hard layer interface.

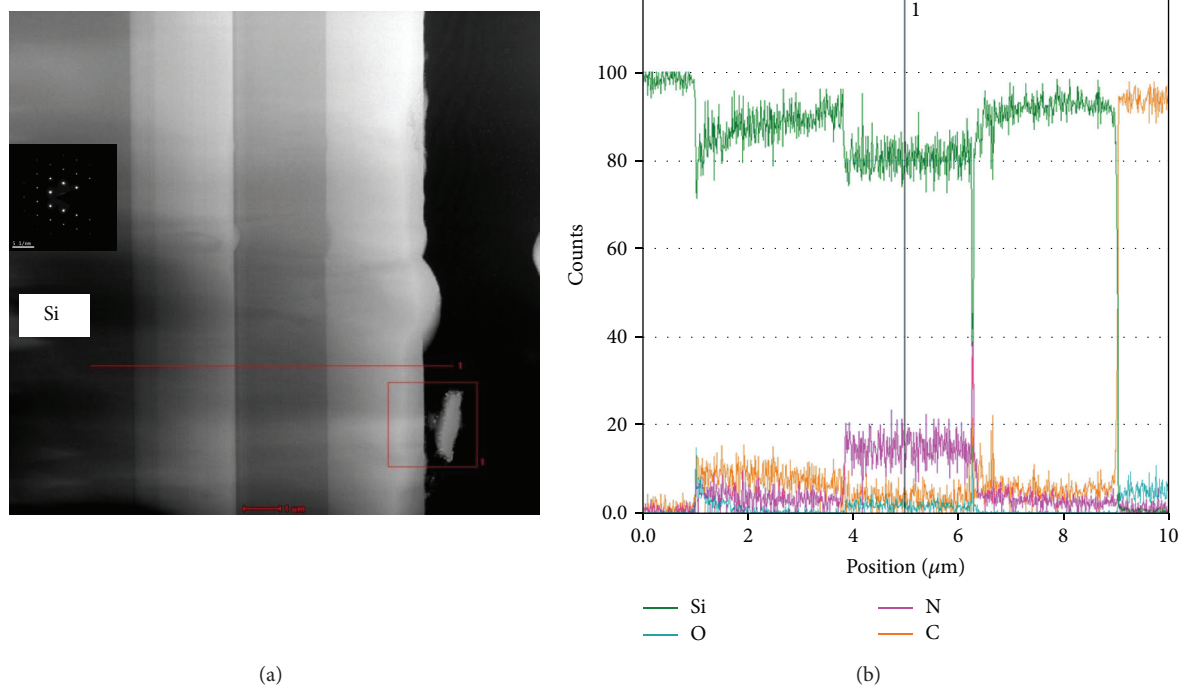


FIGURE 5: TEM microstructure SiCN film E (a) trilayer ABA, inset SAED of substrate Si, and (b) corresponding elemental EDS mapping across the line of interface shown in (a).

of SiCN mainly; however, the nitrogen was found to be more in case of soft film. It was so expected since the deposition was done at higher nitrogen fraction in the plasma compared to the hard film where nitrogen was much less. Nitrogen incorporation in the film reduces the hardness and has been reported in other systems of film such as TiBN, CN due to the formation of different soft phases consisting of different ratios of C and N and Si. The SAED of layer B also essentially showed broad halo ring typical of an amorphous phase SAED (inset of Figure 4(a)). The columnar growth is due to the presence of nitrogen species which leads to slower growth rate and enough mobility of ad atoms leading to more structured growth, whereas in hard layer A the deposition rate was much higher compared to layer B.

Figure 4(b) shows the interface of the middle B layer and the top hard layer. Here it is clear that the columnar growth is visible in B layer only and in A layer the particles are very fine. The interface was found to have sharp boundary, and no other phase was observed in cross section study.

Figure 5(b) shows the nanoprobe STEM-EDS composition line-scan profile across the interface along the line drawn in Figure 5(a), which confirms the sharp boundaries at interface and having higher amount of nitrogen and lesser amount of Si in soft layer B compared to the hard layers A on its both sides, as was discussed above.

Mechanical properties such as hardness and modulus of the film were studied through nanoindentation using Berkovich indenter. The sample A showed an appreciable hardness 31 GPa with 266.6 GPa modulus. Whereas B was soft having 9 GPa and 115 GPa hardness and modulus. The reason behind high hardness in film A was the formation of Si_3N_4

and C_3N_4 which were found to be absent in the soft film B, as has been reported earlier by one of the present authors [20]. These phases, due to their strong covalent bonds and very fine crystallites in amorphous matrix, impart high hardness to the material. Then, double-layer films were deposited (Film C (AB) and Film D (BA)). These coatings showed increase in hardness as well as increase in Young's modulus and were found to be (hardness: 25.9 and 36.4 GPa) (modulus: 266, 339 GPa), respectively. The hardness of film C was lesser than the individual hard film A due to the presence of soft layer and it gives a composite hardness. In the case of film D however the film hardness and modulus were more than the individual hard film. It is due to the reason that upper most layer is of hard film and underlayer soft layer gives a support and resilience, which in case of single layer was substrate. The thickness of the effective composite film increased; hence, the effect of substrate decreased. Hence higher value trilayer coating Film E (ABA) showed a similar range of hardness and modulus as that of D but with higher percentage elastic recovery. The underlayer as soft layer seems to increase the hardness and modulus. The values for hardness, modulus, and percentage elastic recovery for different layers are given in Table 2. It was observed that film E with trilayer (ABA) had higher hardness of 36.4 GPa with modulus 317 GPa along with 62% elastic recovery. This also reveals that trilayer film with ABA combination was tougher.

For fracture behaviour of the different layers microhardness studies were performed on these films. Table 3 shows the hardness obtained for different layers on SS and Si substrates. However, in some cases hardness could not be measured due to the presence of cracks at those loads; hence, values are not

TABLE 2: Hardness, modulus of elasticity, percentage elastic recovery of single-layer, and multilayer by nanoindentation.

Film	No. of layers (substrate-SS304)	Hardness (GPa)	Modulus of elasticity (GPa)	Percentage elastic recovery (%)
A	1	31.7	266.57	59.8
B	1	9.629	115.745	55.0
C (AB)	2	25.978	266.138	52.6
D (BA)	2	36.43	339.387	52.3
E (ABA)	3	36.394	317.236	61.9

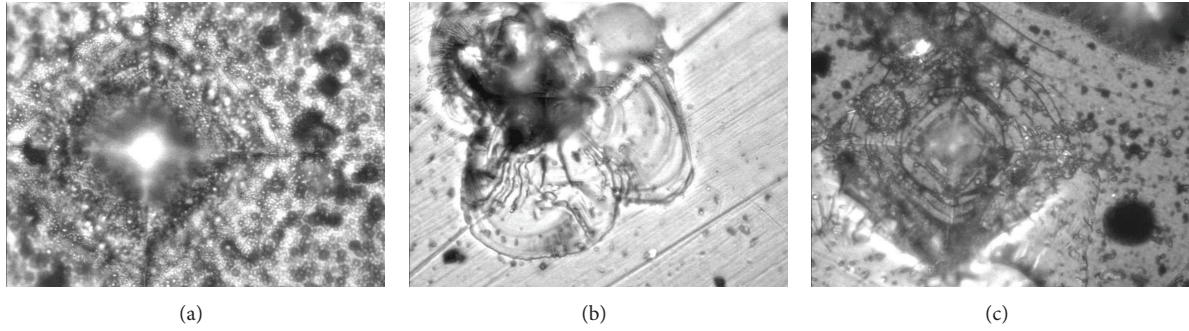


FIGURE 6: Indentation picture of SiCN film on SS 304 (a) film E; HSH layer at 2000 gf, (b) Film A at 1000 gf and (c) Film D; SH layer at 1000 gf.

TABLE 3: Hardness values by microhardness tester.

Load →	25 gf	100 gf	200 gf	300 gf	500 gf	1000 gf
A (SS 304)	6630	6061	4552	4102	—	—
B (SS 304)	3891	3181	2153	1647	—	—
C (AB) (SS 304)	3690	3120	2850	2999	3514	—
D (BA) (SS 304)	4077	4091	3066	3308	2875	—
E (ABA) (SS 304)	5868	3713	3314	2960	2768	2514
A (Si 100)	4077	4091	3066	3308	2875	—
E (ABA) (Si 100)	3690	3120	2850	2999	3514	—

presented. The values of hardness are different and higher than those from nanoindentation, as in nanoindentation the hardness measured is dynamic and at maximum depth without elastic recovery, whereas in microhardness the hardness values are measured after elastic recoveries have taken place after unloading. Hence, in both the cases hardness values depend on the elastic-plastic behaviour of the composite coatings. The decrease of hardness with load is obvious since with increase of load depth of indentation increases, substrate starts influencing, and composite hardness is measured. It is clear from Table 3 that hardness could be measured up to 1000 gf for only trilayer film E.

From fracture behaviour of the films, it was observed that trilayer film had better resistance to loading than individual hard coatings. A soft layer in between played a significant role in building resistant behaviour against indentation. In the fracture in case of film deposited on steel it was observed that the film did not fail even up to 2000 gf but the substrate got plastically deformed resulting in pileups as can be seen in figure lines along the side of the indents but still the film did not show the cracking or spalling (Figure 6(a)). However such failures took at 1000 gf for the film A (Figure 6(b)), spalling

is clearly seen. The double-layer film C having hard and soft layer also showed failure at 1000 gf, but film D having double layer as soft and hard was able to sustain 1000 gf (Figure 6(c)) though here pileups were more than sample E, so the effect of thickness of the film also plays a role; however, for film E the structure shown is for 2000 gf. It clearly demonstrates that three-layer films were tougher. Hence a soft layer film is helping in increasing the load bearing capacity of the film. In multilayer structure the microcracks tend to branch and deflect at the interface between two alternating layers of different materials. The resulting deflection and branching can lead to reduced stress intensities at the crack tips. This means that at every layer interface the cracking process must start all over again, which takes energy and leads to a tougher coating. At the same time the columnar growth of the soft layer SiCN film beneath or in between hard layers is also added to increase the toughness of the multilayered film due to the stress distribution and deflection. The thickness of the bilayer and trilayer films are also more that will also play role in load bearing capacity of the film. A thicker film will fail at higher loads; however, as it is clear from the microstructure that film has not failed but the substrate pileups were observed, the film remained intact at higher loads also for trilayer film.

The fracture toughness of the trilayer film E (ABA) was measured from film deposited on Si as crack length could be measured. Figure 7 shows the crack developed at 1000 gf load. The toughness of the brittle materials can be calculated by Antis equation [21]:

$$K_c = \beta \times \left(\frac{E}{H} \right)^{1/2} \times \frac{P_{\max}}{a^{3/2}}, \quad (2)$$

where β is an empirical constant which depends on the geometry of the indenter and the value is 0.032 for cube corner indenter and 0.016 for Berkovich and Vicker's indenter.

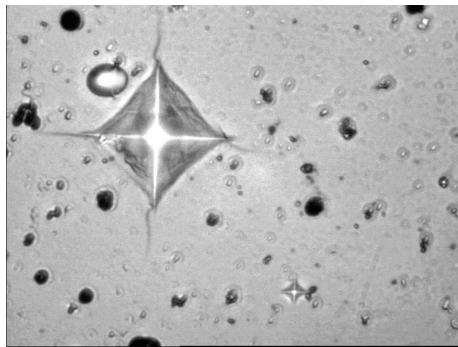


FIGURE 7: A typical cracked surface of SiCN coated multilayer E (ABA) silicon (Si 100) sample at 1000 gf load.

E is the elastic modulus and H is the hardness that was taken from the obtained measured value from nanoindentation as 317.3 and 36.4 GPa, respectively. The average crack length was measured from microindentation and was $13.625\ \mu\text{m}$. The fracture toughness was calculated at different indents and the average toughness was found to be of the order of $9.5\text{--}10\ \text{MPa m}^{1/2}$, which is significant higher for a ceramic nanocomposite and single-layer film compared to the reported values. The value of the single hard SiCN layer was also calculated and was found around $3.5\text{--}4\ \text{MPa m}^{1/2}$.

5. Conclusion

A detailed microstructure of surface as well the interface has been studied for alternate hard and soft nanocomposite SiCN film deposited by single SiC target using RF magnetron sputtering. The average particle size was found to be around $10\text{--}30\ \text{nm}$ by AFM and SEM studies for hard film, whereas for soft film it was found to be in the order of $100\text{--}150\ \text{nm}$. The layered film showed a mixture of fine grains $80\text{--}100\ \text{nm}$. Trilayer film showed particle size around $300\ \text{nm}$. Though the interface was sharp between substrate Si and first hard layer a very thin $5\ \text{nm}$ reacted zone was observed at the interface. Columnar type growth and larger particle sizes compared to hard film were observed in soft film. The elemental composition profile across interface and layers confirms the sharp boundaries at interface between the layers and presence of higher amount of nitrogen and lesser amount of Si in soft layer B compared to both side hard layers A.

The hardness and modulus for individual soft and hard films were (10 GPa and 115 GPa) and (32 GPa and 266 GPa), respectively. The double-layered films hard on soft and soft on hard showed a composite hardness of (26 GPa and 266 GPa) and (36 GPa and 317 GPa), respectively. The trilayer film E (ABA) had 37 GPa and 317 GPa hardness and modulus and appreciable elastic recovery of 62%. The fracture behaviour on steel showed that up to 2000 gf force trilayer film E film did not fail but substrate gets deformed resulting in pileups. The crack could be found at 1000 gf for film on Si and fracture toughness value K_{IC} was measured to be $9.5\text{--}10\ \text{MPa m}^{1/2}$. The trilayer film E (ABA) showed higher tolerance of the load under the microindentation compared to single-layer or

double-layer film. A soft underlayer film below hard layers normally gave a better film in terms of mechanical properties.

References

- [1] J. W. Hutchinson and Z. Suo, "Mixed mode cracking in layered materials," *Advances in Applied Mechanics*, vol. 29, pp. 63–191, 1991.
- [2] M. Gell, "Application opportunities for nanostructured materials and coatings," *Materials Science & Engineering A*, vol. 204, no. 1-2, pp. 246–251, 1995.
- [3] S. Zhang, H. L. Wang, S.-E. Ong, D. Sun, and X. L. Bui, "Hard yet tough nanocomposite coatings—present status and future trends," *Plasma Processes and Polymers*, vol. 4, no. 3, pp. 219–228, 2007.
- [4] A. A. Griffith, "The phenomena of rupture and flows in solids," *Philosophical Transactions of the Royal Society A*, vol. 221, pp. 163–197, 1921.
- [5] S. Vepřek, "Conventional and new approaches towards the design of novel superhard materials," *Surface and Coatings Technology*, vol. 97, no. 1-3, pp. 15–22, 1997.
- [6] M. Stueber, H. Holleck, H. Leiste, K. Seemann, S. Ulrich, and C. Ziebert, "Concepts for the design of advanced nanoscale PVD multilayer protective thin films," *Journal of Alloys and Compounds*, vol. 483, no. 1-2, pp. 321–333, 2009.
- [7] E. G. Wang, "Research on Carbon nitrides," *Progress in Materials Science*, vol. 41, no. 5, pp. 241–298, 1997.
- [8] A. Leyland and A. Matthews, "On the significance of the H/E ratio in wear control: a nanocomposite coating approach to optimised tribological behaviour," *Wear*, vol. 246, no. 1-2, pp. 1–11, 2000.
- [9] J. Ding, Y. Meng, and S. Wen, "Mechanical properties and fracture toughness of multilayer hard coatings using nanoindentation," *Thin Solid Films*, vol. 371, no. 1, pp. 178–182, 2000.
- [10] H. J. Seifert, J. Peng, H. L. Lukas, and F. Aldinger, "Phase equilibria and thermal analysis of Si-C-N ceramics," *Journal of Alloys and Compounds*, vol. 320, no. 2, pp. 251–261, 2001.
- [11] I. Blaszczyk-Lezak, A. M. Wrobel, M. P. M. Kivitorma, I. J. Vayrynen, and A. Tracz, "Silicon carbonitride by remote microwave plasma CVD from organosilicon precursor: growth mechanism and structure of resulting Si:C:N films," *Applied Surface Science*, vol. 253, no. 17, pp. 7211–7218, 2007.
- [12] H. Hoche, D. Allebrandt, M. Bruns, R. Riedel, and C. Fasel, "Relationship of chemical and structural properties with the tribological behavior of sputtered SiCN films," *Surface and Coatings Technology*, vol. 202, no. 22-23, pp. 5567–5571, 2008.
- [13] S. K. Mishra, H. Gaur, P. K. P. Rupa, and L. C. Pathak, "Deposition of nanostructured Si-C-N superhard coatings by rf magnetron sputtering," *Journal of Vacuum Science and Technology B*, vol. 24, no. 3, pp. 1311–1317, 2006.
- [14] A. S. Bhattacharyya, S. K. Mishra, S. Mukherjee, and G. C. Das, "A comparative study of Si-C-N films on different substrates grown by RF magnetron sputtering," *Journal of Alloys and Compounds*, vol. 478, no. 1-2, pp. 474–478, 2009.
- [15] S. K. Mishra, C. Shekhar, P. K. P. Rupa, and L. C. Pathak, "Effect of pressure and substrate temperature on the deposition of nano-structured silicon-carbon-nitride superhard coatings by magnetron sputtering," *Thin Solid Films*, vol. 515, no. 11, pp. 4738–4744, 2007.
- [16] A. Vijayakumar, R. M. Todi, A. P. Warren, and K. B. Sundaram, "Influence of N_2/Ar gas mixture ratio and annealing on optical

- properties of SiCBN thin films prepared by rf sputtering,” *Diamond and Related Materials*, vol. 17, no. 6, pp. 944–948, 2008.
- [17] Z.-W. Deng and R. Souda, “XPS studies on silicon carbonitride films prepared by sequential implantation of nitrogen and carbon into silicon,” *Diamond and Related Materials*, vol. 11, no. 9, pp. 1676–1682, 2002.
- [18] A. S. Bhattacharyya, S. K. Mishra, and S. Mukherjee, “Correlation of structure and hardness of rf magnetron sputtered silicon carbonitride films,” *Journal of Vacuum Science and Technology A*, vol. 28, no. 4, pp. 505–509, 2010.
- [19] S. K. Mishra and A. S. Bhattacharyya, “Effect of substrate temperature on the adhesion properties of magnetron sputtered nano-composite Si-C-N hard thin films,” *Materials Letters*, vol. 62, no. 3, pp. 398–402, 2008.
- [20] A. S. Bhattacharyya and S. K. Mishra, “Raman studies on nanocomposite silicon carbonitride thin film deposited by r.f. magnetron sputtering at different substrate temperatures,” *Journal of Raman Spectroscopy*, vol. 41, no. 10, pp. 1234–1239, 2010.
- [21] G. R. Anstis, P. Chantikul, B. R. Lawn, and D. B. Marshall, “A critical evaluation of indentation techniques for measuring fracture toughness: I, direct crack measurements,” *Journal of the American Ceramic Society*, vol. 64, no. 9, pp. 533–538, 1981.

Research Article

The Effect of Nitrogen Ion Implantation on the Surface Properties of Ti6Al4V Alloy Coated by a Carbon Nanolayer

Petr Vlcak,¹ Frantisek Cerny,¹ Zdenek Weiss,² Stanislav Danis,³ Josef Sepitka,¹
Zdenek Tolde,¹ and Vladimir Jech¹

¹ Faculty of Mechanical Engineering, Czech Technical University in Prague, 16607 Prague, Czech Republic

² Application Center Prague, LECO Instrument Plzen spol. s. r.o., 19000 Prague, Czech Republic

³ Faculty of Mathematics and Physics, Charles University in Prague, 12116 Prague, Czech Republic

Correspondence should be addressed to Petr Vlcak; petr.vlcak@fs.cvut.cz and Frantisek Cerny; frantisek.cerny@fs.cvut.cz

Received 20 September 2013; Revised 21 November 2013; Accepted 26 November 2013

Academic Editor: Tianchang Hu

Copyright © 2013 Petr Vlcak et al. This is an open access article distributed under the Creative Commons Attribution License, which permits unrestricted use, distribution, and reproduction in any medium, provided the original work is properly cited.

The ion beam assisted deposition (IBAD) method was chosen for preparing a carbon thin film with a mixing area on a substrate of Ti6Al4V titanium alloy. Nitrogen ions with energy 90 keV were used. These form a broad ion beam mixing area at the interface between the carbon film and the substrate. We investigated the chemical composition by the glow discharge optical emission spectroscopy (GD-OES) method and the phases by the X-ray diffraction (XRD) method. The measured concentration profiles indicate the mixing of the carbon film into the substrate, which may have an effect on increasing the adhesion of the deposited film. The nanohardness and the coefficient of friction were measured. We found that the modified samples had a markedly lower coefficient of friction even after damage to the carbon film, and they also had higher nanohardness than the unmodified samples. The increased nanohardness is attributed to the newly created phases that arose with ion implantation of nitrogen ions.

1. Introduction

Titanium and titanium alloys have many applications. They are used in the aerospace industry and in biomedical engineering. However, the components of titanium alloys show unsatisfactory tribological properties [1]. The tribological properties of Ti6Al4V titanium alloy have received huge attention worldwide. Many methods and concepts for modifying the coating to reduce the coefficient of friction and the wear rate have been applied. It is known that carbon-based coatings can exhibit a very low coefficient of friction and that their application on a substrate may result in a multiple increase in its working life [2–4]. Due to the high internal stress, these coatings have low adhesion to many substrates [5, 6]. We therefore investigated various deposition techniques and the parameters of these techniques that influence not only the adhesion but also other properties of carbon-based layers [7–9]. In our work, the ion beam assisted deposition (IBAD) method was chosen for modifying the surface properties of the titanium alloy. A carbon coating a few tens nanometers in thickness was applied to a Ti6Al4V

alloy substrate. Subsequent ion bombardment by nitrogen ions with energy 90 keV was aimed at mixing the coating and substrate atoms and hardening the surface area. The parameters of the preparation process were proposed in such a way that the resulting model of the mixed area would have a decreasing concentration towards the substrate. The aim was to investigate the effect of the deposition parameters on the penetration depth of the mixed and implanted atoms and on the surface properties.

2. Materials and Methods

2.1. Substrates. The substrate material was a Ti6Al4V titanium alloy with an $\alpha + \beta$ phase microstructure. The chemical composition is shown in Table 1. The disc samples (20 mm in diameter and 6 mm in thickness) were cut from a titanium alloy bar and were then ground with a series of waterproof abrasive papers up to 2000 grit. Final polishing was performed with 5 μm and 1 μm diamond paste. The samples were ultrasonically cleaned in isopropyl alcohol before the preparation process.

TABLE 1: Chemical composition of the Ti6Al4V titanium alloy (wt%).

Element	C	V	Al	O	N	H	Fe	Ti
Content	0.10	3.50–4.50	5.50–6.75	0.20	0.05	0.0125	0.3	Balance

TABLE 2: Operating parameters of the surface modifications by IBAD.

Parameter	Values
Electron beam deposition of carbon nanolayers	
Base pressure (Pa)	$8 \cdot 10^{-5}$
Work pressure (Pa)	$8 \cdot 10^{-4}$
Acceleration voltage (kV)	6
Emission current (mA)	100
Target	Graphite (99.999%)
Deposition rate ($\text{nm}\cdot\text{s}^{-1}$)	0.15
Nitrogen ion implantation	
Base pressure (Pa)	$9 \cdot 10^{-5}$
Work pressure (Pa)	$5 \cdot 10^{-3}$
Acceleration voltage (kV)	90
Ion beam current density ($\mu\text{A}\cdot\text{cm}^{-2}$)	1.5

2.2. Preparation Process. The modifications of the surface properties were performed by the IBAD method. We used the method in which the modifications were created by sequential deposition and ion implantation. A scheme of the IBAD equipment used in the experiment is presented in our previous work [10]. The samples were attached in a vacuum chamber to a water-cooled rotary manipulator. The thickness of the nanolayers was monitored with a quartz monitor, and the ion beam current was measured using a Faraday cup. The temperature of the samples was measured by a thermocouple located in the sample holder. The modifications were created in two steps. First, a carbon nanolayer was deposited by electron beam evaporation of a graphite tablet. The deposition rate of the carbon nanolayers was about $0.15 \text{ nm}\cdot\text{s}^{-1}$, and the work pressure was about $8 \cdot 10^{-4} \text{ Pa}$. In the second step, the coated substrates were irradiated with nitrogen ions. The acceleration voltage was 90 kV, and the ion beam current density was about $1.5 \mu\text{A}\cdot\text{cm}^{-2}$. During the deposition and ion implantation process, the temperature of the sample was below 50°C . The parameters of the deposition and ion implantation process are shown in Table 2. Prior to deposition, the samples in the vacuum chamber were cleaned by low-energy argon bombardment for 30 min. The energy of the accelerated argon ions was 700 eV, and the ion beam current density was $90 \mu\text{A}\cdot\text{cm}^{-2}$.

The parameters of the IBAD modified samples (nanolayer thickness and fluence of implanted ions) were proposed according to mathematical models of the carbon and nitrogen concentration profiles simulated by TRIDYN code and SRIM code. The chosen parameters are shown in Table 3.

2.3. Chemical and Structure Analysis of the Surface Area. We investigated the chemical composition by means of the glow discharge optical emission spectroscopy (GD-OES) method [11]. A LECO GDS850A optical emission spectrometer was used. GDS850A is an optical emission spectrometer with a

TABLE 3: Parameters of the IBAD modified samples (thickness of the carbon nanolayer, fluence of the nitrogen ions).

Sample	A	B	C	D
Nanolayer thickness (nm)	20	40	20	40
Fluence (cm^{-2})	$1 \cdot 10^{17}$	$1 \cdot 10^{17}$	$5 \cdot 10^{16}$	$5 \cdot 10^{16}$

Paschen-Runge polychromator with focal length of 750 mm, and it has a glow discharge spectral source with a flat cathode (Grimm type). The sample itself serves as a cathode in this arrangement. Atomization of the sample surface is performed by the mechanism of cathode sputtering under an anomalous discharge. The process gas was argon. The spectrometer was calibrated using reference materials with a known composition and known sputter rates, and the “standard” calibration model was used [12]. The intensities of selected emission lines of the elements of interest are expressed as functions of the product $c_{E,M} \cdot q_M$, where $c_{E,M}$ is the concentration of element E in sample M and q_M is its sputter rate. In a depth profile analysis of an unknown sample, the intensities of selected lines are recorded as functions of time. The sample composition is subsequently calculated as a function of time. The sum of the concentrations of all the elements is 100% at each point of the profile, and the unknown sputter rate of the sample was calculated with known emission yields as a function of time. Finally, the time scale was converted into depth by integrating the sputter rate as a function of time.

We investigated the phase composition using the X-ray diffraction (XRD) method. The measurements were performed on a PANalytical X’Pert PRO powder diffractometer. Geometry with the parallel beam with an incident angle of 0.5° was chosen with respect to the intensity of the diffraction pattern. The diffraction was recorded for the 2θ range 20° – 80° . Cobalt radiation with wavelength 0.1789 nm was used.

2.4. Nanoindentation and Sliding Tests. The nanohardness of the ion beam modified samples was investigated by nanoindentation testing. The dependence of the nanohardness on the depth was registered. The quasistatic load controlled experiments were performed on a Hysitron TriboIndenter system with a Berkovich diamond tip, using a partial unloading function consisting of 39 cycles, each composed of a loading segment, a dwell, and an unloading segment ($1 \times 1 \times 1$ second) up to a force value of $5000 \mu\text{N}$. Nanoindentation testing proceeded at a temperature of 23.6°C . Grids of 3×4 indents with $10 \mu\text{m}$ separation were applied for each sample. The nanohardness values were determined for each unloading segment of the indentation cycle. The tip area function was calibrated on the fused quartz sample according to a standard calibration procedure [13].

A sliding test was performed in order to find out the coefficient of friction. A pin-on-disc tribometer was used. A constant normal load of 2 N was set during the test. The radius of rotation was 4 mm , and the velocity was $6 \text{ cm}\cdot\text{s}^{-1}$. The second part of the sliding couple was a 100Cr6 steel ball 6 mm in diameter. The sliding tests proceeded at laboratory ambient temperature 23°C without lubrication and with relative humidity of 57% . The measurements were performed without sucking off the products of abrasive wear.

The sliding test of the modified samples was supplemented by measurements of the surface condition. An atomic force microscope (AFM) in tapping mode was used to characterize the surface topography.

3. Results and Discussion

3.1. Chemical Composition of Surface Area. The chemical composition was investigated by the GD-OES method. Figure 1 shows the resulting concentration profiles of nitrogen and carbon correlated with their mathematical models from the simulation programs. The simulated concentration profiles of carbon were determined by the TRIDYN code [14], and the simulated concentration profiles of nitrogen were determined by the SRIM code [15]. The correspondence between the measured and calculated depth profiles of the carbon distribution is very good. The carbon concentration on the surface is slightly lower than that in the mathematical model of the carbon concentration profile. This may be due to contamination of the surface by the residual atmosphere consisting mainly of nitrogen. Minor differences between the measured and simulated nitrogen concentration profiles are shown in Figure 1.

The experimental concentration profiles are deformed towards the surface in comparison with the mathematical models. A large amount of energy is delivered by nuclear collisions of ions in the surface area. This leads to the formation of point defects. We presume that especially the increased concentration of these defects and their migration lead to deformation of the concentration profiles in this area through radiation enhanced diffusion (RED). Budzynski et al. [16] reported similar deformations of concentration profiles caused by RED. The SRIM simulations do not include the calculation of the dynamic change of the target composition. This has a significant effect on the calculation

result, especially at higher fluences. The depth profile of the nitrogen concentration towards the substrate is undoubtedly influenced by the crater effect. A crater is formed during the GD-OES measurement, and sputtering from the crater wall influences the depth profile of the nitrogen concentration. Diffusion may play some role, but the sputtering from the crater wall has the dominant influence. For the samples with lower fluence ($5 \cdot 10^{16} \text{ cm}^{-2}$), the maximum nitrogen concentration was found to be approximately $10 \text{ at}\%$ at a depth of approximately 75 nm . For the samples with higher fluence ($1 \cdot 10^{17} \text{ cm}^{-2}$), the maximum nitrogen concentration was found to be approximately $20 \text{ at}\%$ at a depth of approximately 80 nm . The mixing area is well perceptible from the course of the concentration profiles of carbon and titanium in Figure 1. For clarity, the concentration profiles of the alloying elements of the substrate (aluminium and vanadium), which are an addition to 100% concentration of the Ti6Al4V alloy, are not plotted in Figure 1.

3.2. XRD Analysis. The crystal structure and the phase composition of the modified samples were examined by the XRD method. This method can provide direct evidence of intermetallic compounds formed in the implanted surface area. Alpha structural phase of the titanium alloy ($\alpha\text{-Ti}$) was observed in all samples, while no minority beta structural phase ($\beta\text{-Ti}$) was identified in the diffraction spectra. In the XRD diffractograms, additional $\alpha\text{-Ti}$ phase with a larger lattice parameter appeared. The implanted nitrogen ions were placed in the interstitial sites, and a solid solution of nitrogen was formed in the titanium matrix. A part of the interstitial nitrogen ions was arranged into the structure, and TiN_x nonstoichiometric phase arose. $\text{TiN}_{0.61}$ phase and graphite were observed for all types of samples. Liu et al. [17] and Schmidt et al. [18] have confirmed that nitrogen ion implantation on Ti-6Al-4V stabilizes the $\alpha\text{-Ti}$ phase and forms compounds of varying composition and stoichiometry. The diffraction spectra of all types of samples have similar characteristics; see Figure 2.

3.3. Nanoindentation Tests. The indentation hardness was investigated by nanoindentation. The resulting depth profiles of the indentation hardness are shown in Figure 3.

The maximum indentation hardness values of the modified samples are shown in Table 4.

Hardness values at depths below 14 nm should be excluded from the depth profiles in Figure 3. The results in this region are influenced by the error originating from standard calibration of the tip area function on fused quartz [13]. The indentation hardness values decrease with increasing contact depth and converge to the hardness of the reference sample within the indentation depth. All samples modified by the ion beam assisted deposition method with the proposed technological parameters had a more than twofold increase in indentation hardness compared to the unmodified substrate. The increase in indentation hardness can be attributed mainly to nitrogen ion implantation. Hard titanium nitrides detected by XRD in the titanium matrix hardened the surface area. Although XRD analysis showed no carbidic phase, it can be assumed that the mixing area may also have an impact on the

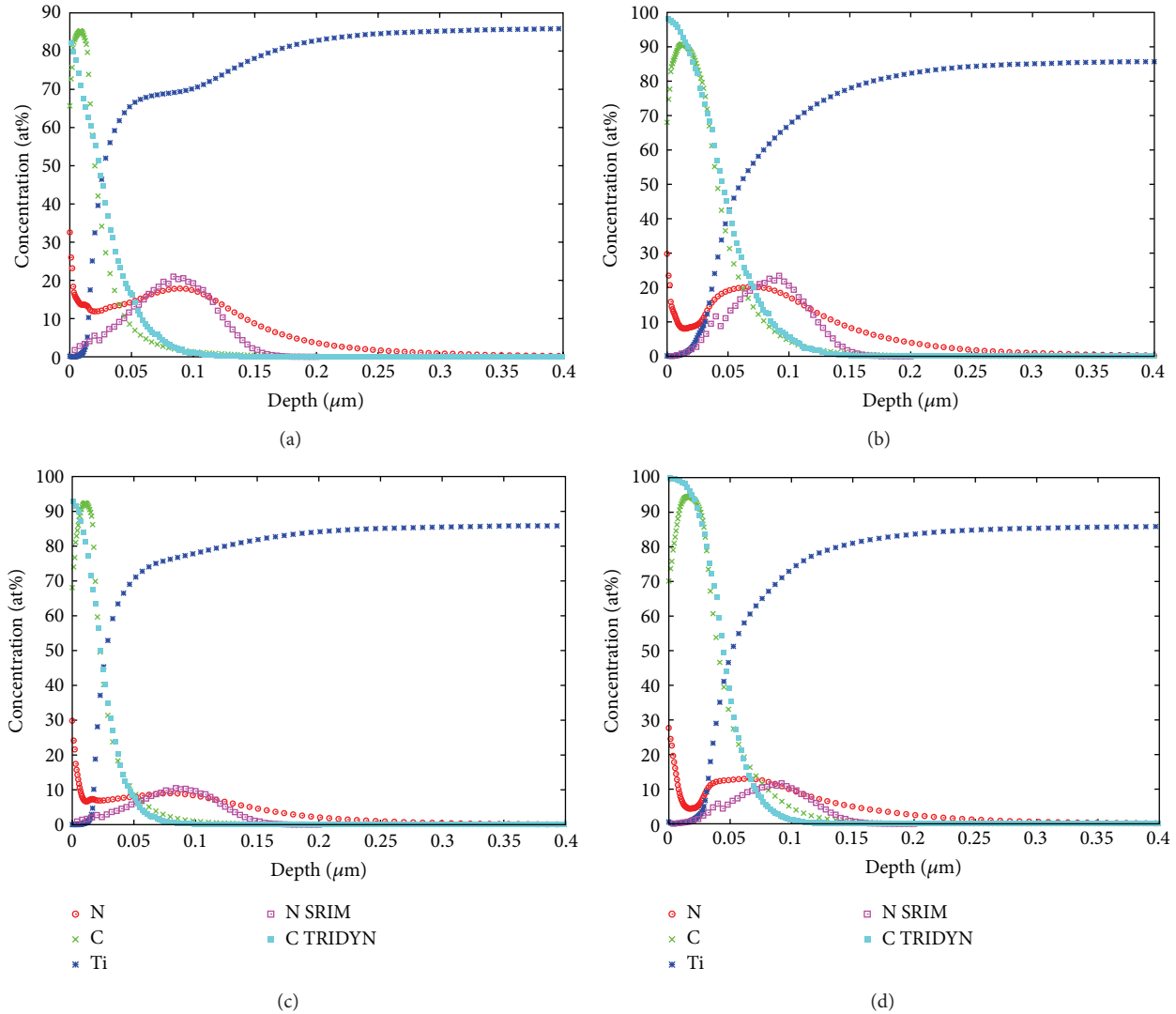


FIGURE 1: Chemical composition of the surface area of the samples with a carbon nanolayer implanted by nitrogen ions—(a) C 20 nm, $1 \cdot 10^{17} \text{ cm}^{-2}$, (b) C 40 nm, $1 \cdot 10^{17} \text{ cm}^{-2}$, (c) C 20 nm, $5 \cdot 10^{16} \text{ cm}^{-2}$, and (d) C 40 nm, $5 \cdot 10^{16} \text{ cm}^{-2}$. Experimental concentration profiles of carbon (C) and nitrogen (N) compared with the simulated concentration profiles of carbon (C TRIDYN) and nitrogen (N SRIM).

increase in indentation hardness. The indentation hardness results in Figure 3 contain the depth profile of the indentation hardness of the coated sample without ion implantation. The maximum hardness value of the sample coated with a carbon nanolayer of 40 nm without ion implantation is 6.3 GPa at a depth of 14 nm. The nonconstant course of the indentation hardness of the unmodified substrate is caused by mechanical strengthening of the surface due to cutting and polishing of the samples.

3.4. Sliding Tests. Sliding tests were carried out on a pin-on-disc tribometer, and the results are shown in Figure 4.

Figure 4 shows the evolution of the coefficient of friction for all ion beam modified samples as a function of the number of cycles. The friction curves of the modified samples can be divided into two parts. The first part represents the low-friction regime, while the second part represents the

increased friction regime. The friction coefficient in the low-friction part is very low, having a value of about 0.1 (Figures 4(a), 4(b), and 4(c)) which is typical for DLC (diamond-like carbon) coatings [19]. The low level of the coefficient of friction is explained by the thin carbon film, which remained on the surface after ion implantation, as shown by the results of the previous analysis of the chemical composition (see Figure 1). The friction coefficient for modifications with a 20 nm carbon nanolayer and both applied fluences remains low in the next 1000 cycles; and for modification with a 40 nm carbon nanolayer and fluence $1 \cdot 10^{17} \text{ cm}^{-2}$, it remains low in the next 3500 cycles; that is, a two times thicker nanolayer increased the duration of the lubrication effect by a factor of 3.5. The low-friction coefficient value remained constant until the carbon nanolayer was destroyed. The hard titanium nitrides detected by XRD in the titanium matrix hardened the surface area after nitrogen ion implantation,

TABLE 4: Maximum indentation hardness values of the modified samples and the reference sample.

Sample	REF (unmodified)	A (C 20 nm/ $1 \cdot 10^{17}$ cm $^{-2}$)	B (C 40 nm/ $1 \cdot 10^{17}$ cm $^{-2}$)	C (C 20 nm/ $5 \cdot 10^{16}$ cm $^{-2}$)	D (C 40 nm/ $5 \cdot 10^{16}$ cm $^{-2}$)
Maximum indentation hardness (GPa)	5.3	13	12.4	11.2	11.5
Indentation depth (nm)	14	15	15	14.6	19.6

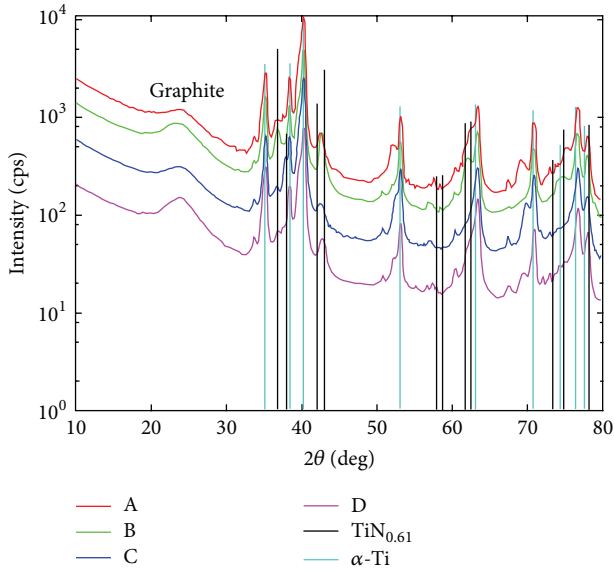
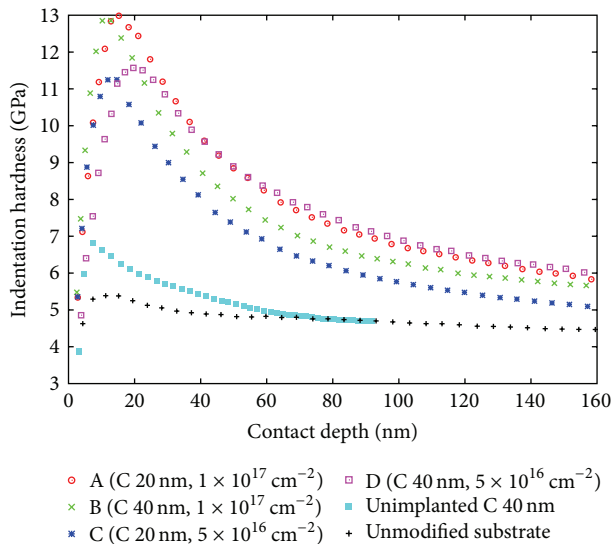
FIGURE 2: Diffraction spectra of the modified samples—(A) C 20 nm, $1 \cdot 10^{17}$ cm $^{-2}$, (B) C 40 nm, $1 \cdot 10^{17}$ cm $^{-2}$, (C) C 20 nm, $5 \cdot 10^{16}$ cm $^{-2}$, and (D) C 40 nm, $5 \cdot 10^{16}$ cm $^{-2}$.

FIGURE 3: Depth profiles of the indentation hardness of the modified samples.

as shown by the depth profiles of the indentation hardness. The carbon film on the hardened surface acted as a solid lubricant. Almost identical friction curves were obtained for the modifications with the 20 nm carbon nanolayer and for both applied fluences. The measurements of samples with a 20 nm carbon nanolayer showed no effect of the fluence on the course of the friction coefficient. The low-friction part was absent for the sample with a 40 nm carbon nanolayer and applied fluence $5 \cdot 10^{16}$ cm $^{-2}$. For the sample with a thicker nanolayer, nitrogen impurity accumulated in the mixing area and the lower nitrogen concentration in the titanium matrix generated lower hardness. The lower hardness of the substrate caused the thicker carbon nanolayer to break, and an increase in the coefficient of friction occurred just at the beginning of the measurement. The thinner nanolayer did not break, because the maximum nitrogen concentration is in the titanium matrix, and the nanolayer is more flexible. The part with increased friction is characterized by a sharp increase in the coefficient of friction. In all samples, the coefficient of friction is approximately 0.28 in this part and is constant until the end of the test. This means a two times greater decrease in the friction coefficient in comparison with the unmodified substrate, which has a coefficient of friction of 0.6. The resulting reduction in the friction coefficient is attributed to the sliding properties of the mixing area. According to Budzynski et al. [16], implanting nitrogen ions into Ti6Al4V does not cause such a significant reduction in the coefficient of friction without the lubrication effect of a sliding layer.

Three-dimensional AFM images of the selected samples (unmodified substrate and modified sample with a 20 nm carbon nanolayer and applied fluence $1 \cdot 10^{17}$ cm $^{-2}$) are shown in Figures 5(a) and 5(b). The scanning area was $20 \times 20 \mu\text{m}^2$. It can be seen that the surface topography of the modified sample and the unmodified substrate are almost the same. Nevertheless, ion beam modifications slightly smoothed down the surface roughness. The surface of the substrate was very smooth, with visible deep depressions. The deep depressions may also be a source of premature failure of the carbon nanolayer. In the case of high concentrations of these depressions, the depressions could be a source of graphite lubricant and could thus reduce the friction.

4. Conclusion

The results of chemical composition analysis indicate that the proposed parameters of the modification process lead to the mixing area. The carbon nanolayer remained on the

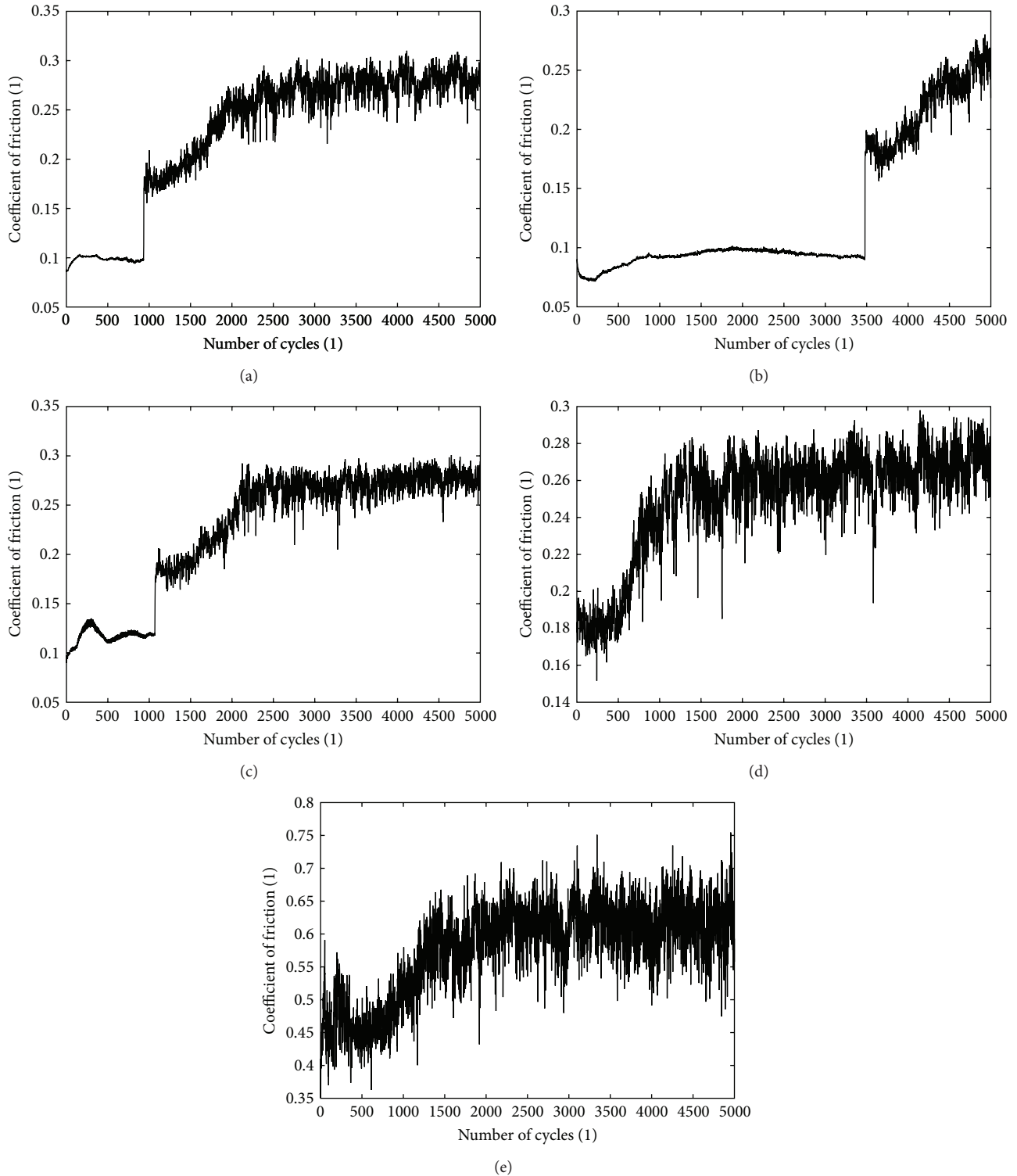


FIGURE 4: Results of sliding tests of the samples with a carbon nanolayer implanted by nitrogen ions—(a) C 20 nm, $1 \cdot 10^{17} \text{ cm}^{-2}$, (b) C 40 nm, $1 \cdot 10^{17} \text{ cm}^{-2}$, (c) C 20 nm, $5 \cdot 10^{16} \text{ cm}^{-2}$, (d) C 40 nm, $5 \cdot 10^{16} \text{ cm}^{-2}$, and (e) unmodified substrate.

surface after ion implantation, and this had an influence on the sliding properties. The differences between the measured concentration profiles and the simulated profiles are attributed in particular to the influence of radiation enhanced diffusion, that is, diffusion accelerated by radiation defects.

The results show that the increase in the indentation hardness is primarily the result of nitrogen ion implantation. The hard titanium nitrides detected in the surface area are probably the dominant source of higher hardness. The measurements showed a slight increase in the indentation

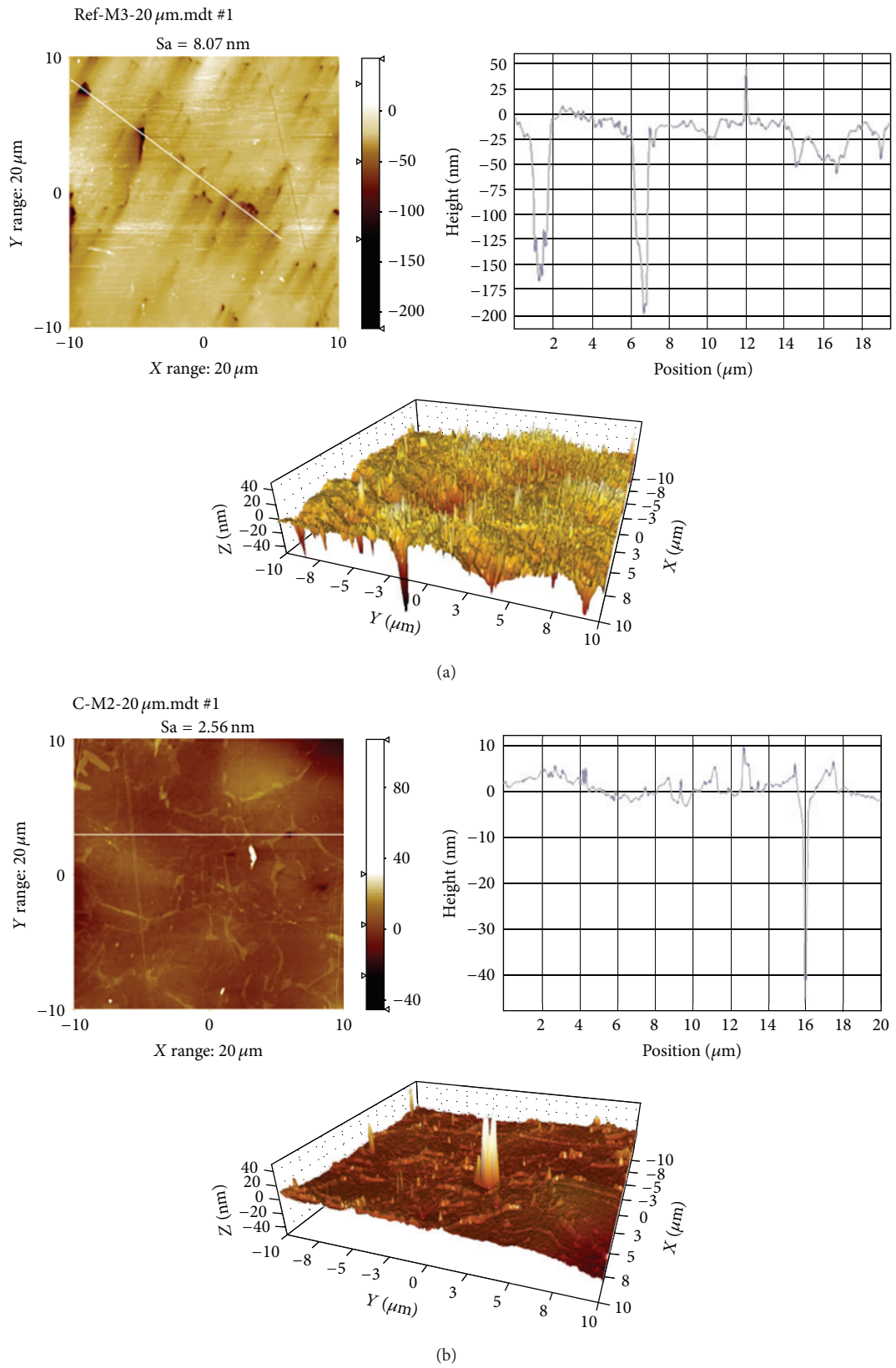


FIGURE 5: AFM images of selected samples (a) unmodified substrate and (b) a modified sample with a 20 nm carbon nanolayer and applied fluence $1 \cdot 10^{17} \text{ cm}^{-2}$.

hardness of the coated sample without ion implantation. The carbon nanolayer may make some contribution to the increase in hardness.

The results of the sliding test indicate that the carbon nanolayer greatly decreased the friction coefficient. The nanolayer on the hardened surface acted as a solid lubricant. Although damage to this nanolayer increased the friction coefficient, its value was lower than the friction coefficient of the unmodified substrate. Double reduction of the friction coefficient was observed. This fact leads to the conclusion that the friction coefficient can be considerably reduced by forming a mixing area. In order to form the mixing area without a residual carbon layer, it is necessary to modify the proposed IBAD deposition parameters.

Acknowledgment

This research has been supported by the Ministry of Education, Youth and Sports of the Czech Republic, Project SGS OHK2-033-13 of the Czech Technical University in Prague.

References

- [1] M. Geetha, A. K. Singh, R. Asokamani, and A. K. Gogia, "Ti based biomaterials, the ultimate choice for orthopaedic implants—a review," *Progress in Materials Science*, vol. 54, no. 3, pp. 397–425, 2009.
- [2] S. Wei, T. Shao, and P. Ding, "Improvement of orthodontic friction by coating archwire with carbon nitride film," *Applied Surface Science*, vol. 257, no. 24, pp. 10333–10337, 2011.
- [3] S.-W. Jiang, B. Jiang, Y. Li, Y.-R. Li, G.-F. Yin, and C.-Q. Zheng, "Friction and wear study of diamond-like carbon gradient coatings on Ti6Al4V substrate prepared by plasma source ion implant-ion beam enhanced deposition," *Applied Surface Science*, vol. 236, no. 1–4, pp. 285–291, 2004.
- [4] D. Sheeja, B. K. Tay, S. M. Krishnan, and L. N. Nung, "Tribological characterization of diamond-like carbon (DLC) coatings sliding against DLC coatings," *Diamond and Related Materials*, vol. 12, no. 8, pp. 1389–1395, 2003.
- [5] S. Neuville and A. Matthews, "A perspective on the optimisation of hard carbon and related coatings for engineering applications," *Thin Solid Films*, vol. 515, no. 17, pp. 6619–6653, 2007.
- [6] L. F. Bonetti, G. Capote, L. V. Santos, E. J. Corat, and V. J. Trava-Airoldi, "Adhesion studies of diamond-like carbon films deposited on Ti6Al4V substrate with a silicon interlayer," *Thin Solid Films*, vol. 515, no. 1, pp. 375–379, 2006.
- [7] Y. Ren, I. Erdmann, B. Kützün, F. Deuerler, and V. Buck, "Effect of deposition parameters on wear particle size distribution of DLC coatings," *Diamond and Related Materials*, vol. 23, pp. 184–188, 2012.
- [8] M. C. Salvadori, F. S. Teixeira, W. W. R. Araújo, L. G. Sgubin, and I. G. Brown, "Interface tailoring for adhesion enhancement of diamond-like carbon thin films," *Diamond and Related Materials*, vol. 25, no. 6, pp. 8–12, 2012.
- [9] V. J. Trava-Airoldi, L. F. Bonetti, G. Capote, L. V. Santos, and E. J. Corat, "A comparison of DLC film properties obtained by r.f. PACVD, IBAD, and enhanced pulsed-DC PACVD," *Surface and Coatings Technology*, vol. 202, no. 3, pp. 549–554, 2007.
- [10] P. Vlčák, F. Černý, Z. Tolde, J. Šepitka, I. Gregora, and S. Danis, "Mechanical and tribological properties of carbon thin film with tungsten interlayer prepared by ion beam assisted deposition," *Journal of Materials*, vol. 2013, Article ID 630156, 4 pages, 2013.
- [11] R. K. Marcus and J. A. C. Broekaert, *Glow Discharge Plasmas in Analytical Spectroscopy*, John Wiley & Sons, Chichester, UK, 2003.
- [12] Z. Weiss, "Emission yields and the standard model in glow discharge optical emission spectroscopy: links to the underlying physics and analytical interpretation of the experimental data," *Spectrochimica Acta B*, vol. 61, no. 2, pp. 121–133, 2006.
- [13] W. C. Oliver and G. M. Pharr, "An improved technique for determining hardness and elastic modulus using load and displacement sensing indentation experiments," *Journal of Materials Research*, vol. 7, no. 6, pp. 1564–1580, 1992.
- [14] A. Arranz and C. Palacio, "Ion beam mixing of Ti/Al interfaces by nitrogen irradiation," *Surface Science*, vol. 601, no. 18, pp. 4510–4514, 2007.
- [15] N. Berrouachedi, M. Bouslama, A. Abdellaoui et al., "Investigation by EELS and TRIM simulation method of the interaction of Ar⁺ and N⁺ ions with the InP compound," *Applied Surface Science*, vol. 256, no. 1, pp. 21–26, 2009.
- [16] P. Budzynski, A. A. Youssef, and J. Sielanko, "Surface modification of Ti-6Al-4V alloy by nitrogen ion implantation," *Wear*, vol. 261, no. 11-12, pp. 1271–1276, 2006.
- [17] Y. Z. Liu, X. T. Zu, S. Y. Qiu et al., "Phase formation and modification of corrosion property of nitrogen implanted Ti-Al-V alloy," *Vacuum*, vol. 81, no. 1, pp. 71–76, 2006.
- [18] H. Schmidt, A. Schminke, M. Schmiedgen, and B. Baretzky, "Compound formation and abrasion resistance of ion-implanted Ti6Al4V," *Acta Materialia*, vol. 49, no. 3, pp. 487–495, 2001.
- [19] A. J. Gant, M. G. Gee, and L. P. Orkney, "The wear and friction behaviour of engineering coatings in ambient air and dry nitrogen," *Wear*, vol. 271, no. 9-10, pp. 2164–2175, 2011.